Electromagnetic Behaviour Of Various DNG Metamaterial Structures With Elliptical Surfaces

BY

OGUZHAN AKGOL
B.A., Inonu University, 2001
M.S., Polytechnic University, 2004

THESIS

Submitted as partial fulfillment of the requirements
for the degree of Doctor of Philosophy in Electrical and Computer Engineering
in the Graduate College of the
University of Illinois at Chicago, 2011

Chicago, Illinois

Defense Committee:

Danilo Erricolo
Piergiorgio Uslenghi
Sharad Laxpati
H.Y. David Yang
Vito Daniele, Politecnico Di Torino

To my Professors and my family,

ACKNOWLEDGMENTS

This dissertation would not have been possible without the guidance and the help of several individuals who in one way or another contributed and extended their valuable assistance in the preparation and completion of this study.

First and foremost, my utmost gratitude to Prof. Danilo Erricolo and Prof. Piergiorgio Uslenghi whose guidance and encouragement I will never forget. Prof. Erricolo and Prof. Uslenghi have been my inspiration as I hurdle all the obstacles in the completion this research work.

Secondly, I want to thank my committee for their priceless advices and suggestions.

Last but not the least, my family and my friends for giving their continuous support.

OA

PREFACE

In this work, exact analyses of some structures are considered. These structures contain lenses and trenches that are made or filled by DNG Metamaterial. In double negative metamaterials (DNG), both permittivity and permeability are negative resulting in a negative index of refraction. DNGs are also referred to as negative index metamaterials (NIM). What is a metamaterial? In recent years, there has been a growing interest in the fabricated structures and composite materials that either mimic known material responses or qualitatively have new, physically realizable response functions that do not occur or may not be readily available in nature. The unconventional response functions of these metamaterials are often generated by artificially fabricated inclusions or inhomogeneities embedded in a host medium or connected to or embedded on a host surface. Exotic properties for such metamaterials have been predicted; many experiments have confirmed our basic understanding of many of them. The underlying interest in metamaterials is the potential to have the ability to engineer the electromagnetic and optical properties of materials for a variety of applications. The impact of metamaterials may be enormous: If one can tailor and manipulate the wave properties, significant decreases in the size and weight of components, devices, and systems along with enhancements in their performance appear to be realizable.

TABLE OF CONTENTS

TABLE OF CONTENTS (Continued)

CHAPTER **PAGE**

LIST OF FIGURES

LIST OF FIGURES (Continued)

LIST OF FIGURES (Continued)

LIST OF ABBREVIATIONS

DNG	Double Negative
DPS	Double Positive
RCS	Radar Cross Section
FEM	Finite Element Method
HFSS	High Frequency Structure Simulator
UIC	University of Illinois at Chicago

SUMMARY

This research focuses on the exact electromagnetic analysis of various double negative (DNG) metamaterial structures. The boundaries of these structures are coordinate surfaces of the elliptic cylinder coordinate system. Four structures are considered: (1) the elliptic cylinder, (2) a semielliptical cavity flush mounted under an aperture, (3) a quarter elliptic channel at the corner between two metallic walls and (4) a multilayered elliptical cylinder. All these structures are made of or filled with DNG metamaterial. Inside a DNG metamaterial both permittivity and permeability are negative resulting in a negative index of refraction. These two-dimensional boundary-value problems are solved exactly, in the frequency domain, when the primary field is either a plane wave of arbitrary polarization and direction of incidence or an electric or magnetic line source. The electromagnetic fields in the various regions and the incident fields are expressed in terms of infinite series of elliptic-cylinder wave functions, involving products of radial and angular Mathieu functions. Numerical results shown to clarify the effect of DNG metamaterials in these geometries.

CHAPTER 1

BACKGROUND

In this work, the following structures: (1) the elliptic cylinder, (2) a semielliptical cavity flush mounted under an aperture, (3) a quarter elliptic channel at the corner between two metallic walls and (4) a multilayered elliptical cylinder are studied. Similar structures have been investigated in (1), (2), (3), (4), (5), (6), (7), (8). The novelty of this work is that these structures contain DNG metamaterials. In order to introduce these structures, we begin by recalling some mathematical details for the elliptic cylinder coordinate system, Mathieu functions and DNG metamaterials.

1.1 Elliptic Cylinder Coordinate System

This work focus on electromagnetic behavior of various DNG Metamaterial structures with elliptical surfaces. Therefore, it is worth to mention about elliptic cylinder coordinate system, which we will be using heavily.

Referring to Figure 1, the two foci F_1 and F_2 are located at $-d/2$ and $+d/2$, respectively, on the x-axis of the Cartesian coordinate system. The rectangular coordinates (x, y, z) are related to the elliptic cylinder coordinates (u, v, z) by:

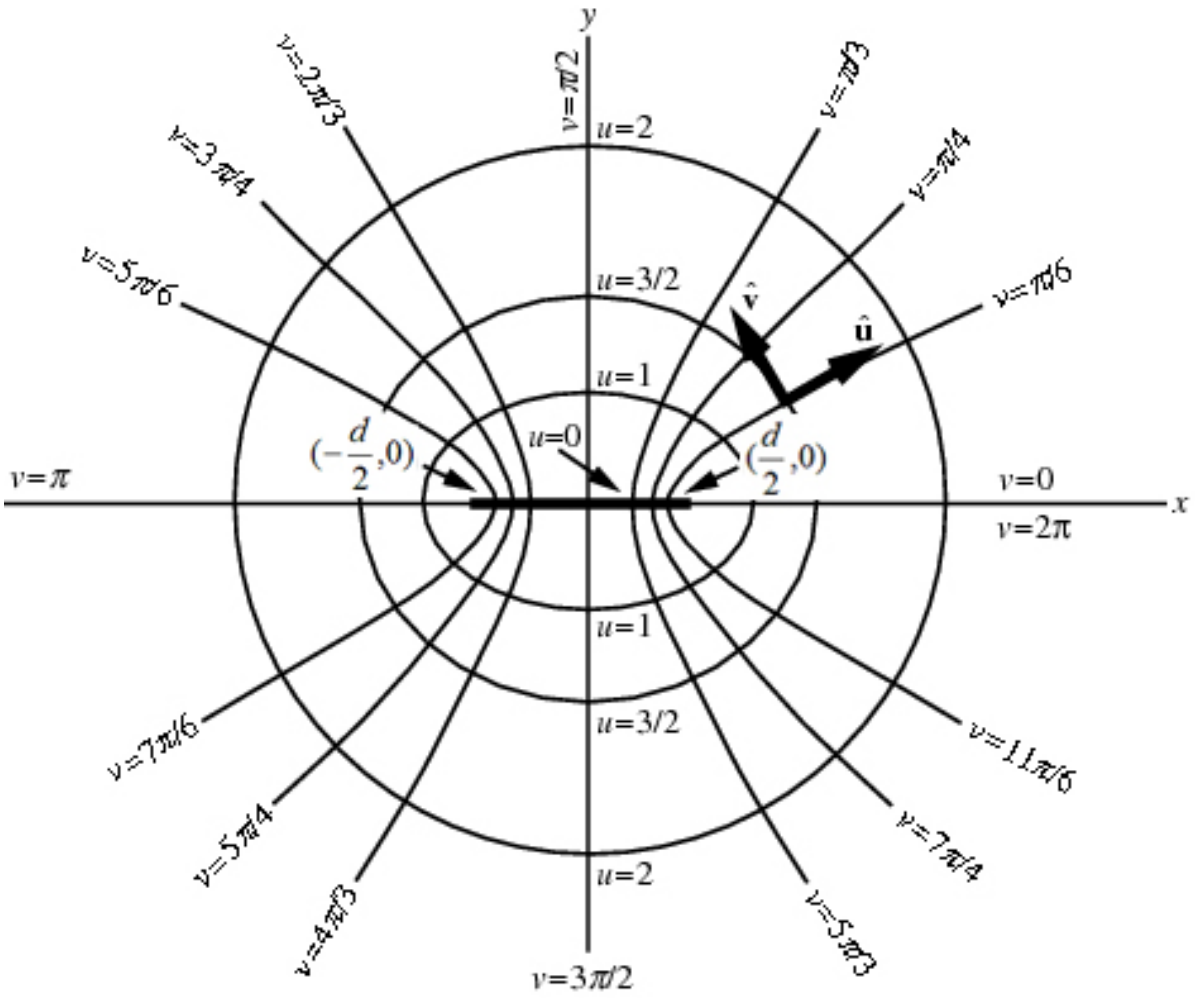

Figure 1. Elliptic Cylinder Coordinate System

$$x = \frac{d}{2}\cosh u \cos v, \tag{1.1}$$

$$y = \frac{d}{2}\sinh u \sin v,$$

$$z = z$$

where $0 \leq u < \infty$, $0 \leq v \leq 2\pi$, $-\infty < z < \infty$.

The v coordinates represent the angle of the asymptotes to the hyperbolic cylinders symmetrical about the x-axis. The u coordinates are confocal elliptic cylinders centered on the origin. When $u = 0$ the ellipse reduces to a line and it gets closer to a circle when u has larger values.

1.2 Geometries of the Problems

Various DNG Metamaterial structures with elliptical surfaces are considered.

The first geometry analyzed consists of an infinite cylinder of elliptical cross section made of a DNG metamaterial whose permittivity and permeability are real and opposite to the corresponding parameters in the surrounding space, see Figure 2.

The second geometry is a semielliptical trench flush-mounted under an infinite perfect electric conductor plane, see Figure 10. The trench is slotted along the interfocal distance of its cross-section, and is filled with a DNG metamaterial that is isoimpedance to the material filling the half-space above the trench.

The third geometry is a partially covered cavity, or trench, located along the edge of two intersecting metallic walls perpendicular to each other. The cross-section of the cavity is a quarter ellipse and is slotted along the interfocal distance, see Figure 20. The cavity is filled with a DNG metamaterial that is isoimpedance to the material filling the half-space above the trench.

The fourth geometry is a confocal elliptic cylindrical layer made of double-negative metamaterial. The space inside and outside the layer is filled with a lossless homogeneous double-positive medium, see Figure 27.

These two-dimensional boundary-value problems are solved exactly, in the frequency domain, when the primary field is either a plane wave of arbitrary polarization and direction of incidence or an electric or magnetic line source.

The electromagnetic fields in the various regions and the incident fields are expressed in terms of infinite series of elliptic-cylinder wave functions, involving products of radial and angular Mathieu functions. In the free space or in the DPS region, the electric permittivity is ε and the magnetic permeability is μ, whereas in the DNG region the same quantities become $-\varepsilon$ and $-\mu$, respectively. The wavevector is $k = \sqrt{\varepsilon\mu}$ in DPS region and $k = -\sqrt{\varepsilon\mu}$ inside DNG media. We define a dimensionless parameter $c = kd/2$ in the DPS material and $-c$ in DNG metamaterial. The intrinsic impedance $Z = \sqrt{\mu/\varepsilon}$ is the same for both media. The wavenumbers in the DPS and DNG region have opposite signs, however, it is still possible to enforce the boundary conditions at the surface of the boundaries on a mode to mode basis that leads to an exact analytical solution for the modal expansion coefficients.

1.3 Mathieu Functions

The Mathieu functions are the solutions to the Mathieu differential equation and they are discussed in, e.g. (9), (10). Mathieu functions appear naturally in the solution of the Helmholtz equation in cylindrical coordinates. There is an analogy between the solution of the scattering of an electromagnetic wave by a circular cylinder and an elliptic cylinder. The Mathieu radial

functions correspond to the Bessel functions and the Mathieu angular functions correspond to the trigonometric functions. We will make frequent use of the following expansions.

1.4 Expansion of a plane wave in terms of Mathieu functions

A plane wave may be expanded in a series of elliptic-cylinder functions (11) as

$$\exp[jk(x\cos\varphi_0 + y\sin\varphi_0)] = \sqrt{8\pi}\sum_{m=0}^{\infty} j^m \left[\frac{1}{N_m^{(e)}}\mathrm{Re}_m^{(1)}(c,u)\mathrm{Se}_m(c,v)\mathrm{Se}_m(c,\varphi_0) + \frac{1}{N_m^{(o)}}\mathrm{Ro}_m^{(1)}(c,u)\mathrm{So}_m(c,v)\mathrm{So}_m(c,\varphi_0)\right], (u \geq u_1) \tag{1.2}$$

1.5 Expansion of a cylindrical wave in terms of Mathieu Functions

Similarly, a Hankel functions of the second kind may be expanded in a series of elliptic-cylinder functions (11):

$$H_0^{(2)}(kR) = 4\sum_{m=0}^{\infty}\left[\frac{1}{N_m^{(e)}}\mathrm{Re}_m^{(1)}(c,u_<)\mathrm{Re}_m^{(4)}(c,u_>)\mathrm{Se}_m(c,v)\mathrm{Se}_m(c,v_0) + \frac{1}{N_m^{(o)}}\mathrm{Ro}_m^{(1)}(c,u_<)\mathrm{Ro}_m^{(4)}(c,u_>)\mathrm{So}_m(c,v)\mathrm{So}_m(c,v_0)\right], \tag{1.3}$$

1.6 Relationship Between Electric and Magnetic Field

Using Maxwell's equations and expanding them in elliptic cylindrical coordinate system, we can obtain the magnetic field from the electric field by

$$\boldsymbol{H_{1,2}} = \frac{j}{cZ\sqrt{\xi^2-\eta^2}}\left(\frac{\partial E_{(1,2)z}}{\partial v}\hat{u} - \frac{\partial E_{(1,2)z}}{\partial u}\hat{v}\right). \tag{1.4}$$

In a similar way, electric field can be obtained from

$$\boldsymbol{E_{1,2}} = \frac{jZ}{c\sqrt{\xi^2 - \eta^2}} \left(-\frac{\partial H_{(1,2)z}}{\partial v}\hat{u} + \frac{\partial H_{(1,2)z}}{\partial u}\hat{v} \right). \tag{1.5}$$

CHAPTER 2

ELECTROMAGNETIC SCATTERING BY AN ELLIPTIC DNG METAMATERIAL CYLINDER

2.1 INTRODUCTION

The first geometry we consider consists of an infinite cylinder of elliptical cross section made of a DNG metamaterial, shown in Figure 2. The primary field is a plane wave of arbitrary polarization propagating in a direction perpendicular to the axis of the cylinder. The elliptical cylinder has real and negative refractive index. The medium surrounding the cylinder is double-positive (DPS) having real but positive refractive index. Both media have the same intrinsic impedance value, $Z_1 = Z_2$.

2.2 PLANE WAVE INCIDENCE

2.2.1 E-polarization

Consider a plane wave incident perpendicularly to the cylinder axis and polarized parallel to z-axis , with primary electric field

$$\boldsymbol{E}^i = \hat{z}E_z^i = \hat{z}\exp[jk(x\cos\varphi_0 + y\sin\varphi_0)]. \tag{2.1}$$

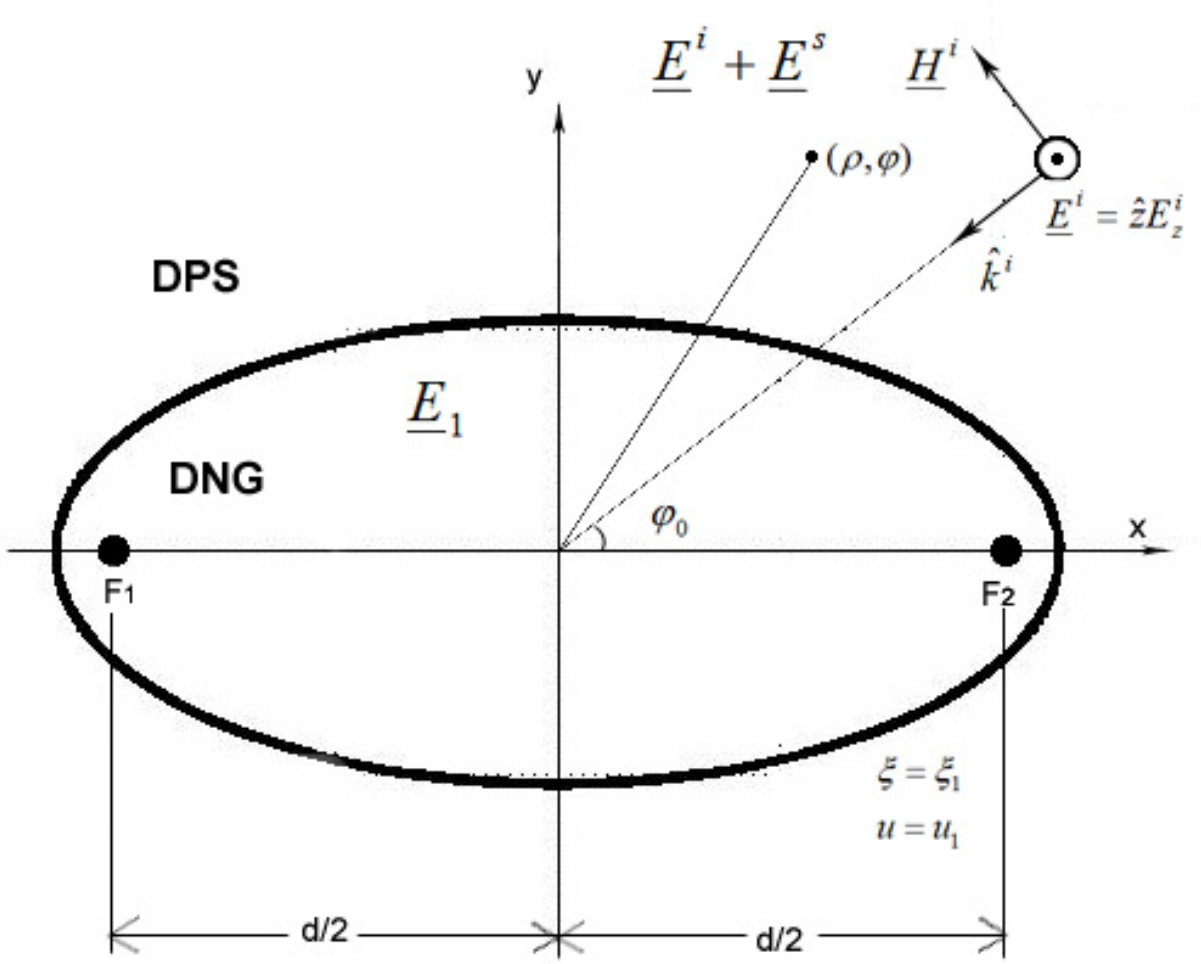

Figure 2. Geometry of the problem.

The incident field may be expanded in a series of elliptic-cylinder functions (11)

$$E_z^i = \sqrt{8\pi} \sum_{m=0}^{\infty} j^m \left[\frac{1}{N_m^{(e)}} \mathrm{Re}_m^{(1)}(c,u)\mathrm{Se}_m(c,v)\mathrm{Se}_m(c,\varphi_0) + \frac{1}{N_m^{(o)}} \mathrm{Ro}_m^{(1)}(c,u)\mathrm{So}_m(c,v)\mathrm{So}_m(c,\varphi_0) \right],$$

$$(u \geq u_1). \tag{2.2}$$

The scattered electric field outside the cylinder can be written as

$$E_z^s = \sqrt{8\pi}\sum_{m=0}^{\infty} j^m \left[\frac{c_m}{N_m^{(e)}}\mathrm{Re}_m^{(4)}(c,u)\mathrm{Se}_m(c,v)\mathrm{Se}_m(c,\varphi_0) + \frac{d_m}{N_m^{(o)}}\mathrm{Ro}_m^{(4)}(c,u)\mathrm{So}_m(c,v)\mathrm{So}_m(c,\varphi_0)\right], \quad (u \geq u_1) \tag{2.3}$$

and the electric field inside the cylinder is

$$E_{1z} = \sqrt{8\pi}\sum_{m=0}^{\infty} j^m \left[\frac{a_m}{N_m^{(e)}}\mathrm{Re}_m^{(1)}(-c,u)\mathrm{Se}_m(-c,v)\mathrm{Se}_m(-c,\varphi_0) + \frac{b_m}{N_m^{(o)}}\mathrm{Ro}_m^{(1)}(-c,u)\mathrm{So}_m(-c,v)\mathrm{So}_m(-c,\varphi_0)\right], (0 \leq u \leq u_1). \tag{2.4}$$

Using the properties of Mathieu functions, we can obtain

$$E_{1z} = \sqrt{8\pi}\sum_{m=0}^{\infty} j^m \left[\frac{a_m}{N_m^{(e)}}\mathrm{Re}_m^{(1)}(-c,u)\mathrm{Se}_m(c,v)\mathrm{Se}_m(c,\varphi_0) + \frac{b_m}{N_m^{(o)}}\mathrm{Ro}_m^{(1)}(-c,u)\mathrm{So}_m(c,v)\mathrm{Se}_m(c,\varphi_0)\right], (0 \leq u \leq u_1). \tag{2.5}$$

The magnetic fields are

$$H_v^i + H_v^s = \frac{-j}{cZ\sqrt{\xi^2-\eta^2}}\frac{\partial}{\partial u}(E_z^i + E_z^s), \quad (u \geq u_1) \tag{2.6}$$

and

$$H_{1v} = \frac{j}{cZ\sqrt{\xi^2 - \eta^2}} \frac{\partial}{\partial u} E_{1z}, \quad (0 \leq u \leq u_1). \tag{2.7}$$

and the unknown expansion coefficients a_m, b_m, c_m, d_m may be determined by the application of the boundary conditions, i.e. the continuity of the tangential components of the total electric and magnetic fields, across the interface $u = u_1$

$$\left(E_z^i + E_z^s\right)_{u=u_1} = \left(E_{1z}\right)_{u=u_1}, \tag{2.8}$$

$$\left(H_v^i + H_v^s\right)_{u=u_1} = \left(H_{1v}\right)_{u=u_1}. \tag{2.9}$$

The result is

$$a_m = \frac{-j}{\sqrt{\xi_1^2 - 1}\Delta^{(e)}}, \tag{2.10}$$

$$b_m = \frac{-j}{\sqrt{\xi_1^2 - 1}\Delta^{(o)}}, \tag{2.11}$$

$$c_m = \frac{\Delta_{(c)}}{\Delta^{(e)}}, \tag{2.12}$$

$$d_m = \frac{\Delta_{(d)}}{\Delta^{(o)}}, \tag{2.13}$$

where

$$\Delta^{(e)} = \mathrm{Re}_m^{(1)}(-c,u_1)\mathrm{Re}_m^{(4)'}(c,u_1) + \mathrm{Re}_m^{(4)}(c,u_1)\mathrm{Re}_m^{(1)'}(-c,u_1), \tag{2.14}$$

$$\Delta^{(o)} = \mathrm{Ro}_m^{(1)}(-c,u_1)\mathrm{Ro}_m^{(4)'}(c,u_1) + \mathrm{Ro}_m^{(4)}(c,u_1)\mathrm{Ro}_m^{(1)'}(-c,u_1), \tag{2.15}$$

$$\Delta_{(c)} = -\left[\mathrm{Re}_m^{(1)}(-c,u_1)\mathrm{Re}_m^{(1)'}(c,u_1) + \mathrm{Re}_m^{(1)'}(-c,u_1)\mathrm{Re}_m^{(1)}(c,u_1)\right], \tag{2.16}$$

$$\Delta_{(d)} = -\left[\mathrm{Ro}_m^{(1)}(-c,u_1)\mathrm{Ro}_m^{(1)'}(c,u_1) + \mathrm{Ro}_m^{(1)'}(-c,u_1)\mathrm{Ro}_m^{(1)}(c,u_1)\right]. \tag{2.17}$$

Details of the computations leading to the previous results are given in Appendix-A. We may write the far field as

$$E_z^s|_{\xi\to\infty} \approx P^{(e)}(\phi)\sqrt{\frac{2}{\pi k\rho}}\exp(-jk\rho + j\frac{\pi}{4}) \tag{2.18}$$

where we introduce a far field coefficient $P^{(e)}(\phi)$

$$P^{(e)}(\phi) = 2\pi\sum_{m=0}^{\infty}(-1^m)\left[\frac{c_m}{N_m^{(e)}}\mathrm{Se}_m(c,v)\mathrm{Se}_m(c,\varphi_0) + \frac{d_m}{N_m^{(o)}}\mathrm{So}_m(c,v)\mathrm{So}_m(c,\varphi_0)\right]. \tag{2.19}$$

The bistatic radar cross section (RCS) per unit length is

$$\sigma^{(e)}(\phi) = \frac{4}{k}\left|P^{(e)}(\phi)\right|^2. \tag{2.20}$$

2.2.2 H-polarization

The analysis is similar to that for E-Polarization. The incident magnetic field is

$$\boldsymbol{H}^i = \hat{z} H_z^i = \hat{z} \exp[jk(x\cos\varphi_0 + y\sin\varphi_0)] \tag{2.21}$$

and may be expanded as

$$H_z^i = \sqrt{8\pi} \sum_{m=0}^{\infty} j^m \left[\frac{1}{N_m^{(e)}} \mathrm{Re}_m^{(1)}(c,u)\mathrm{Se}_m(c,v)\mathrm{Se}_m(c,\varphi_0) + \frac{1}{N_m^{(o)}} \mathrm{Ro}_m^{(1)}(c,u)\mathrm{So}_m(c,v)\mathrm{So}_m(c,\varphi_0) \right],$$
$$(u \geq u_1). \tag{2.22}$$

The scattered magnetic field outside the cylinder can be written as

$$H_z^s = \sqrt{8\pi} \sum_{m=0}^{\infty} j^m \left[\frac{e_m}{N_m^{(e)}} \mathrm{Re}_m^{(4)}(c,u)\mathrm{Se}_m(c,v)\mathrm{Se}_m(c,\varphi_0) + \frac{f_m}{N_m^{(o)}} \mathrm{Ro}_m^{(4)}(c,u)\mathrm{So}_m(c,v)\mathrm{So}_m(c,\varphi_0) \right],$$
$$(u \geq u_1). \tag{2.23}$$

The magnetic field inside the cylinder is:

$$H_{1z} = \sqrt{8\pi} \sum_{m=0}^{\infty} j^m \left[\frac{g_m}{N_m^{(e)}} \mathrm{Re}_m^{(1)}(-c,u)\mathrm{Se}_m(c,v)\mathrm{Se}_m(c,\varphi_0) + \right.$$
$$\left. \frac{h_m}{N_m^{(o)}} \mathrm{Ro}_m^{(1)}(-c,u)\mathrm{So}_m(c,v)\mathrm{So}_m(c,\varphi_0) \right], \quad (0 \leq u \leq u_1). \tag{2.24}$$

The total electric field inside and outside the cylinder is

$$E_v^i + E_v^s = \frac{jZ}{c\sqrt{\xi^2 - \eta^2}} \frac{\partial}{\partial u}(H_z^i + H_z^s), \quad (u \geq u_1) \tag{2.25}$$

and

$$E_{1v} = \frac{-jZ}{c\sqrt{\xi^2 - \eta^2}} \frac{\partial}{\partial u} H_{1z}, (0 \leq u \leq u_1). \tag{2.26}$$

The boundary conditions can be written as

$$\left(H_z^i + H_z^s\right)_{u=u_1} = \left(H_{1z}\right)_{u=u_1}, \tag{2.27}$$

$$\left(E_v^i + E_v^s\right)_{u=u_1} = \left(E_{1v}\right)_{u=u_1}. \tag{2.28}$$

When we apply the boundary conditions, we find that the modal coefficients are equal to those for E-polarization

$$g_m = a_m, \quad e_m = c_m \tag{2.29}$$

$$h_m = b_m, \quad f_m = d_m. \tag{2.30}$$

The far field is

$$H_z^s|_{\xi\to\infty} \approx P^{(h)}(\phi)\sqrt{\frac{2}{\pi k\rho}}\exp(-jk\rho + j\frac{\pi}{4}) \tag{2.31}$$

where the far field coefficient is $P^{(h)}(\phi) = P^{(e)}(\phi)$, and the bistatic radar cross section is the same for both polarizations: $\sigma^{(h)}(\phi) = \sigma^{(e)}(\phi)$.

2.3 SIMULATION AND NUMERICAL RESULTS

To examine the scattering effect of the cylinder, we look at the bistatic radar cross section (RCS) per unit length. The expression of the RCS for both polarizations is

$$\sigma(\phi) = \frac{4}{k}\left|P(\phi)\right|^2. \tag{2.32}$$

Let us consider the RCS normalized to the wavelength

$$\frac{\sigma^(\phi)}{\lambda} = \frac{2}{\pi}\left|P(\phi)\right|^2 \tag{2.33}$$

where $\lambda = 2\pi/k$ is the wavelength, and $P(\phi)$ is given by (Equation A.25).

Figure 3 shows the eigenfunction solution for our problem, for different values of c. The value of c is controlled by the frequency and the focal distance d:

$$c = \frac{kd}{2} = \frac{\pi d}{\lambda} \tag{2.34}$$

In Figure 3, we used $\varphi_0 = \pi/4$ and $u = 0.25$. To analyze the effect of c, we have used 4 different c values ($c = 0.5, c = 1.55, c = 2.5, c = 3.5$). For small values of c, the reflection from the cylinder is pronounced. However, when c is approximately equal or larger than 2, energy transmission in the forward direction prevails.

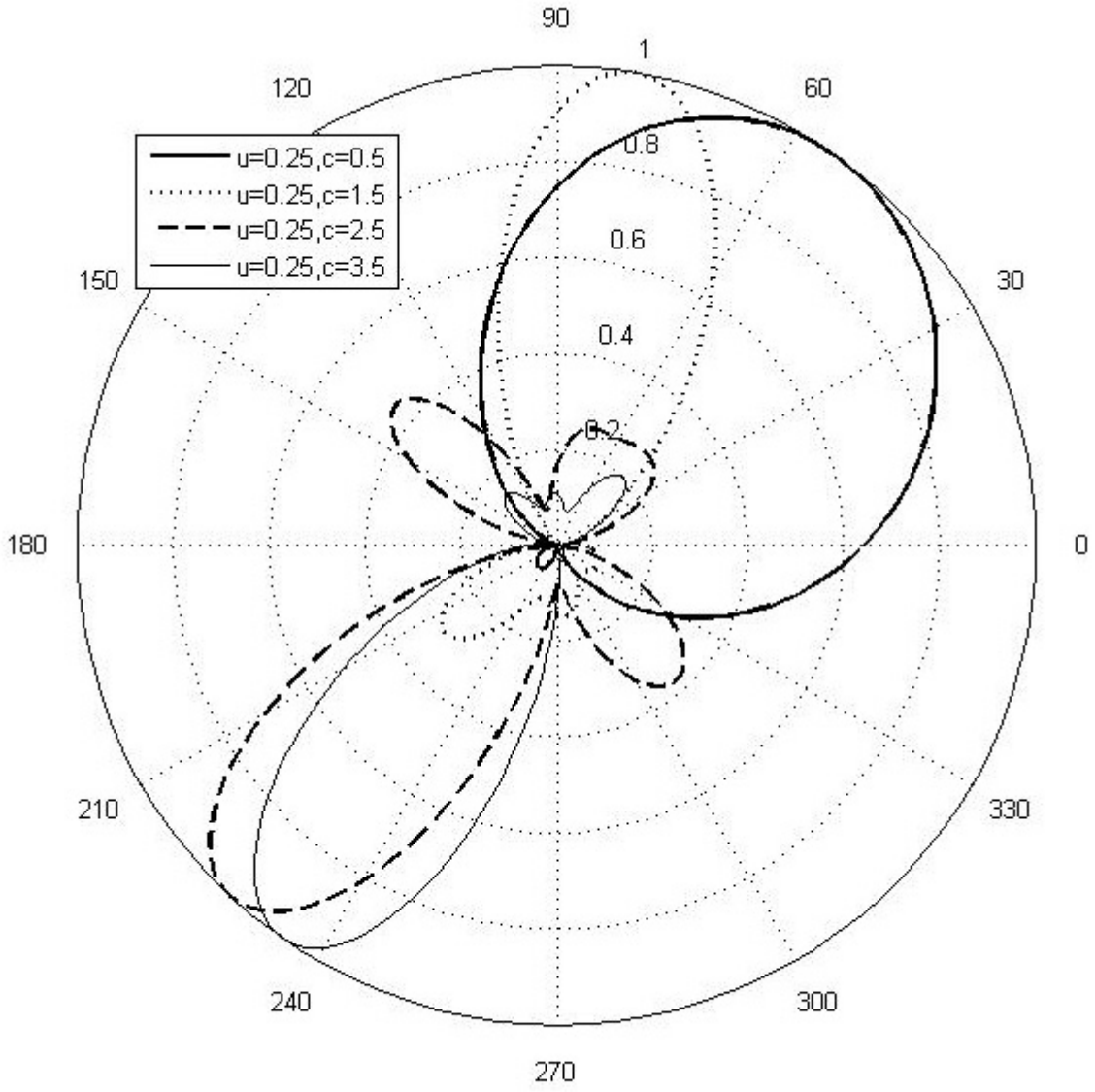

Figure 3. Normalized RCS with $u_1 = 0.25$ and $c = 0.5, 1.5, 2.5, 3.5$

CHAPTER 3

EXACT IMAGING BY AN ELLIPTIC LENS

3.1 INTRODUCTION

The imaging of an isotropic line source located at one of the focal lines of an elliptic cylindrical lens made of DNG metamaterial has been studied in the optical limit (12). It has been shown that the line source is imaged onto a non-isotropic virtual line source located at the other focal line of the lens. Here, an exact electromagnetic solution of the same problem is obtained as an infinite series of elliptic-cylinder wave functions, each term of the series consisting of products of radial and angular Mathieu functions. The numerical results are compared with the optical limit obtained in (12). Some preliminary results were previously presented at a conference (13) and (14).

The double-positive (DPS) material filling the infinite space outside the lens is characterized by a real positive electric permittivity ϵ and a real positive magnetic permeability μ, while the corresponding parameters inside the DNG lens are a real negative permittivity $-\epsilon$ and a real negative permeability $-\mu$. As a consequence of causality, the refractive index outside the lens is real positive, and is the opposite of the real negative refractive index inside the lens, while the intrinsic impedance has the same real positive value $Z = \sqrt{(\mu/\epsilon)}$ everywhere (15).

The time-dependence factor $\exp(+j\omega t)$ is omitted throughout. The wave number is $k = \omega\sqrt{(\epsilon\mu)}$ in the DPS medium and $-k$ in the DNG material.

3.2 Geometry of the problem

A cross-sectional view of the structure in a plane $z =$ constant is shown in Figure 4.

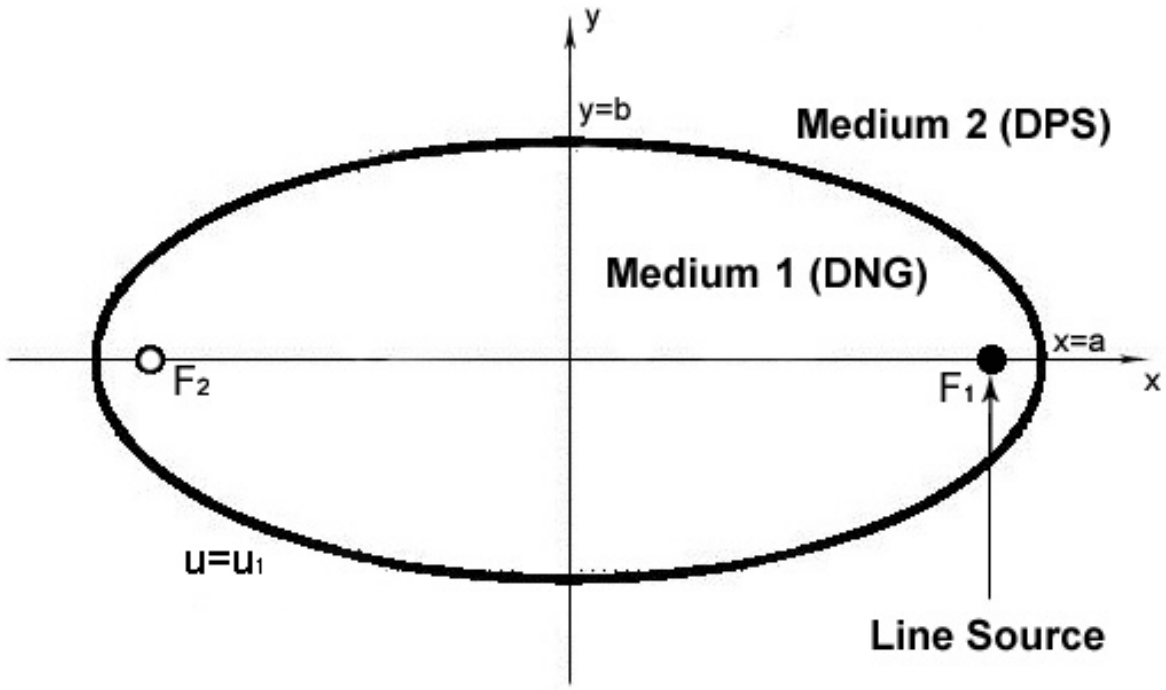

Figure 4. Cross section of the geometry of the problem.

The rectangular coordinates (x, y, z) are related to the elliptic cylinder coordinates (u, v, z) by $x = (d/2)\cosh u \cos v, y = (d/2)\sinh u \sin v, z = z$, where d is the inter focal distance, $0 \leq u <$

∞, $0 \leq v \leq 2\pi$, and $-\infty < z < \infty$. Curves $u = constant$ are ellipses and curves $v = constant$ are hyperbolas. We define the dimensionless real positive parameter $c = kd/2 = \pi d/\lambda$, where λ is the wavelength.

3.3 Line source incidence

3.3.1 E-polarization

Consider an electric line source parallel to the z-axis and located at $(x_0, y_0) \equiv (u_0, v_0)$ inside the DNG lens, whose primary electric field is

$$\boldsymbol{E}^i = \hat{z} E_z^i = \hat{z} H_0^{(2)}(-kR) \tag{3.1}$$

where

$$R = \sqrt{(x - x_0)^2 + (y - y_0)^2} \tag{3.2}$$

is the distance between the line source and the observation point $(x, y) \equiv (u, v)$ and $H_0^{(2)}$ is the Hankel function of the second kind. The incident field may be expanded in a series of elliptic-cylinder wave functions (1)-(11):

$$\begin{aligned} E_{1z}^i = H_0^{(2)}(-kR) = 4 \sum_{m=0}^{\infty} \\ \left[\frac{1}{N_m^{(e)}} \mathrm{Re}_m^{(1)}(-c, u_<) \mathrm{Re}_m^{(4)}(-c, u_>) \mathrm{Se}_m(-c, v_0) \mathrm{Se}_m(-c, v) + \right. \\ \left. \frac{1}{N_m^{(o)}} \mathrm{Ro}_m^{(1)}(-c, u_<) \mathrm{Ro}_m^{(4)}(-c, u_>) \mathrm{So}_m(-c, v_0) \mathrm{So}_m(-c, v) \right] \end{aligned} \tag{3.3}$$

where $u_<$ ($u_>$) is the smaller (larger) between u and u_0. When the electric line source is located inside the lens at the focal line ($x_0 = d/2, y_0 = 0$) the incident electric field only contains even functions and it becomes

$$E^i_{1z} = 4\sum_{m=0}^{\infty} \frac{1}{N_m^{(e)}} \mathrm{Re}_m^{(1)}(-c,0)\mathrm{Re}_m^{(4)}(-c,u)\mathrm{Se}_m(c,v) \tag{3.4}$$

because of properties of Mathieu functions (1) and the fact that the angular Mathieu functions Se_m and So_m are even functions of the parameter c has been taken into account. It should be noted that the Mathieu radial functions are not even functions of c (16). The scattered field inside the lens is

$$E^s_{1z} = 4\sum_{m=0}^{\infty} \frac{a_m}{N_m^{(e)}} \mathrm{Re}_m^{(1)}(-c,u)\mathrm{Se}_m(c,v). \tag{3.5}$$

Outside the lens, the scattered field is

$$E^s_{2z} = 4\sum_{m=0}^{\infty} \frac{b_m}{N_m^{(e)}} \mathrm{Re}_m^{(4)}(c,u)\mathrm{Se}_m(c,v), (u \geq u_1) \tag{3.6}$$

and it satisfies the radiation condition because it contains the radial functions of the fourth kind, $\mathrm{Re}_m^{(4)}$. The modal expansion coefficients $a_m^{(e)}$ and $b_m^{(e)}$, are obtained by imposing the boundary

conditions on the continuity of the total tangential components of **E** and **H** across the interface at $u = u_1$, yielding

$$a_m = \frac{-\mathrm{Re}_m^{(1)}(-c,0)}{\Delta}\left[\mathrm{Re}_m^{(4)'}(c,u_1)\mathrm{Re}_m^{(4)}(-c,u_1) + \mathrm{Re}_m^{(4)}(c,u_1)\mathrm{Re}_m^{(4)'}(-c,u_1)\right], \tag{3.7}$$

$$b_m = \frac{-\mathrm{Re}_m^{(1)}(-c,0)}{\Delta}\left[\mathrm{Re}_m^{(4)'}(-c,u_1)\mathrm{Re}_m^{(1)}(-c,u_1) - \mathrm{Re}_m^{(4)}(-c,u_1)\mathrm{Re}_m^{(1)'}(-c,u_1)\right] \tag{3.8}$$

where

$$\Delta = \mathrm{Re}_m^{(1)}(-c,u_1)\mathrm{Re}_m^{(4)'}(c,u_1) + \mathrm{Re}_m^{(1)'}(-c,u_1)\mathrm{Re}_m^{(4)}(c,u_1) \tag{3.9}$$

and the prime means the derivative with respect to the argument u. Detailed derivations of the modal coefficients are given in Appendix-B.

3.3.2 H-polarization

The analysis is similar to that for E-polarization. For a magnetic line source located at F_1 in Figure 20, the incident magnetic field is

$$\mathbf{H^i} = \hat{\mathbf{z}} H_z^i, \tag{3.10}$$

with

$$H_{1z}^i = 4\sum_{m=0}^{\infty} \frac{1}{N_m^{(e)}} \mathrm{Re}_m^{(1)}(-c,0)\mathrm{Re}_m^{(4)}(-c,u)\mathrm{Se}_m(-c,0)\mathrm{Se}_m(-c,v). \tag{3.11}$$

The scattered magnetic field inside the lens is

$$H_{1z}^{s} = 4\sum_{m=0}^{\infty} \frac{c_m}{N_m^{(e)}} \mathrm{Re}_m^{(1)}(-c,u)\mathrm{Se}_m(-c,v) \tag{3.12}$$

and the total magnetic fields outside the lens is

$$H_{2z}^{s} = 4\sum_{m=0}^{\infty} \frac{d_m}{N_m^{(e)}} \mathrm{Re}_m^{(4)}(c,u)\mathrm{Se}_m(c,v). \tag{3.13}$$

The modal coefficients are obtained from the application of the boundary conditions and, because of duality, one finds $c_m = a_m$ and $d_m = b_m$.

3.3.3 Far Field Expressions

For E polarization, the scattered field is given by equation (Equation B.5). When the Mathieu radial function $\mathrm{Re}_m^{(4)}(c,u)$ is replaced by its asymptotic expression $j^m \exp(-jk\rho + j\pi/4)\sqrt{k\rho}$, one finds

$$E_{2z}^{s} \approx 4\frac{\exp(-jk\rho + j\pi/4)}{\sqrt{k\rho}} \sum_{m=0}^{\infty} b_m \frac{j^m}{N_m^{(e)}} Se_m(c,v). \tag{3.14}$$

In order to obtain results that are not dependent upon the distance ρ from the origin, we divide the previous expression by $\exp(-j(k\rho - \pi/4)/\sqrt{k\rho}$ so that we obtain the far field radiation pattern

$$P^{(e)}(v) = 4\sum_{m=0}^{\infty} b_m \frac{j^m}{N_m^{(e)}} Se_m(c, v). \tag{3.15}$$

Similarly, for H polarization, using (Equation 3.13) and the asymptotic expression of $\mathrm{Re}_m^{(4)}(c, u)$, we obtain the expression for far field radiation

$$H_{2z}^s \approx 4\frac{\exp(-jk\rho + j\pi/4)}{\sqrt{k\rho}} \sum_{m=0}^{\infty} d_m \frac{j^m}{N_m^{(e)}} \mathrm{Se}_m(c, v) \tag{3.16}$$

from which we extract the far field radiation pattern

$$P^{(h)}(v) = 4\sum_{m=0}^{\infty} d_m \frac{j^m}{N_m^{(e)}} \mathrm{Se}_m(c, v). \tag{3.17}$$

3.4 Numerical results

We compare the far-field radiation pattern of (Equation 3.15) with the exact geometrical optics solution presented in (12). For this purpose, we consider two ellipses with $u_1 = 0.5$

and $u_1 = 0.8$. Each ellipse is represented normalized to its major axis $2a$ in Figure 5, which emphasizes also the variation in eccentricity

$$\chi = \frac{d}{2a} = \frac{1}{\cosh u_1} \tag{3.18}$$

by showing a comparison with a circle. The two ellipses have major axes with different lengths so that we compare numerical results in terms of the ratio between the wavelength and the major axis, *i.e.*

$$r = \frac{2a}{\lambda} = \frac{d \cosh u_1}{\lambda}. \tag{3.19}$$

Hence, the eccentricity controls the different behavior of the solutions corresponding to the same value of the ratio r. The solution presented in (12) is formulated in terms of the power emitted per unit angle, computed as

$$p(v) = \frac{1 - \chi^2}{1 + \chi^2 - 2\chi \cos v} \tag{3.20}$$

which corresponds to $r = \infty$. Therefore the previous formula is compared with the magnitude square of the far-field radiation pattern (Equation 3.15), *i.e.*

$$\left| P^{(e)}(v) \right|^2 = 16 \left| \sum_{m=0}^{\infty} b_m \frac{j^m}{N_m^{(e)}} Se_m(c, v) \right|^2 . \tag{3.21}$$

For a magnetic line source, $|P^{(h)}(v)|^2$ is given by (Equation 3.21) with b_m replaced by d_m.

Figure 6 shows the normalized polar plot of $\left|P^{(e)}(v)\right|^2$ for E polarization and the geometrical optics solution $p(v)$ for an ellipse with $u_1 = 0.5$ and eccentricity $\chi = 0.8868$. When the ellipse is electrically small, $r = 0.1$ the far-field result is significantly different from the geometrical optics solution because it is closer to an omni directional pattern. However, when the ellipse is electrically larger, $r = 1$ and $r = 3$, a better agreement with the geometrical optics solution is observed. Similar conclusions may be made for the results computed for H polarization and reported in Figure 8 and Figure 9.

A second set of results is shown in Figure 7 for an ellipse with $u_1 = 0.8$ and eccentricity $\chi = 0.748$. Similar to the previous case, the agreement with the geometrical optics solution improves when the ellipse becomes electrically large. However, in this second case, when $r = 3$ the pattern $\left|P^{(e)}(v)\right|^2$ is much closer to the geometrical optics solution. We attribute this closer agreement to the smaller value of eccentricity for the ellipse with $u_1 = 0.8$. In fact, with a smaller eccentricity, the shape of the second ellipse is closer to a circle (as evident in Figure 5) and at each point of the ellipse the curvature is also smaller. Therefore, each point of the border of the ellipse is locally flatter thus better approaching the geometrical optics limit.

Finally, all the numerical results correspond to the summation of the first 16 terms of the series (Equation 3.21) and the evaluation of Mathieu function was accomplished using an extension of the Fortran code described in (17) combined with the acceleration technique (18). The series (Equation 3.21) converges slowly and one needs to stop the summation before numerical instabilities occur.

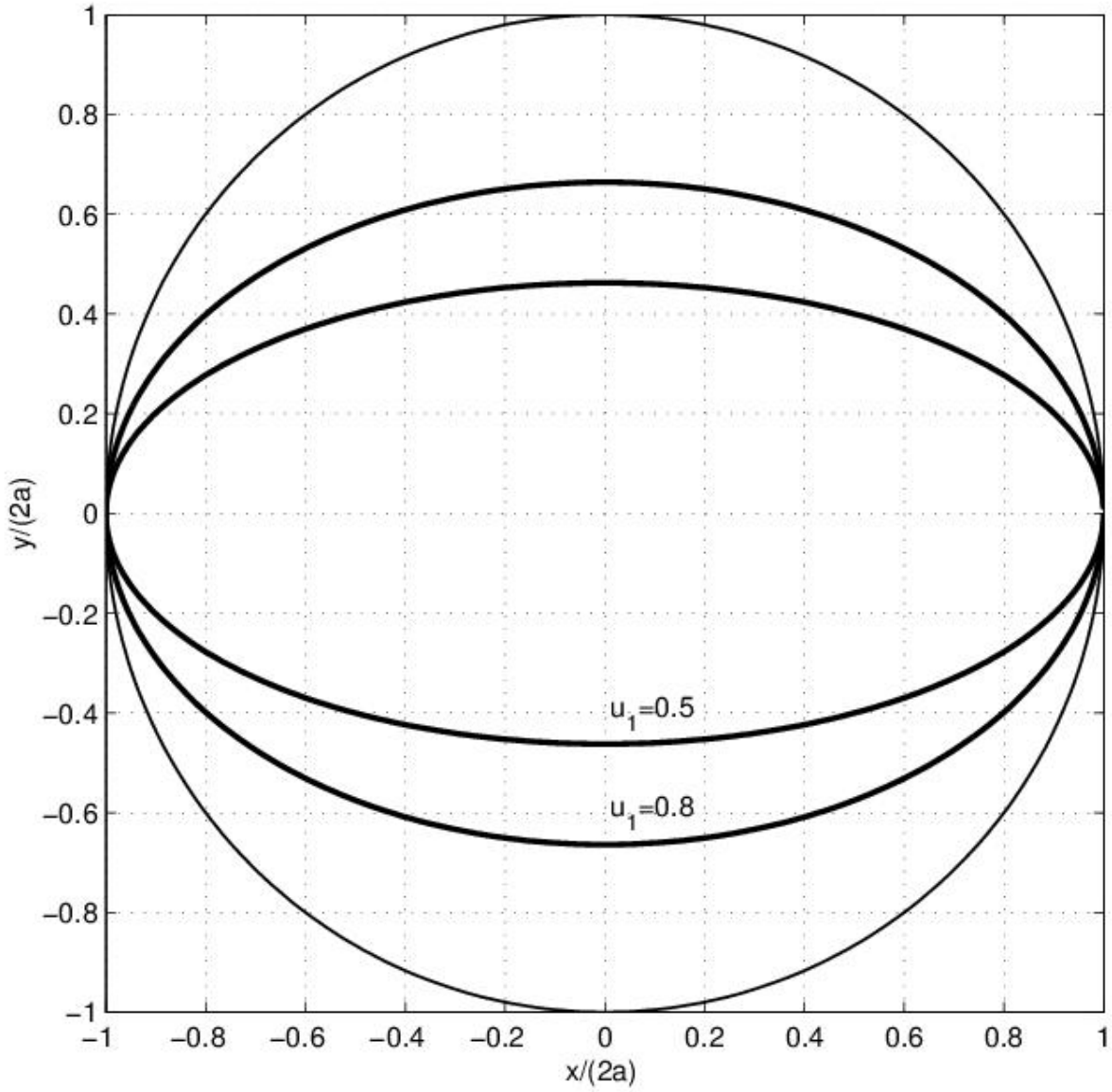

Figure 5. Normalized cross sections of the two ellipses considered in the numerical examples and comparison with a circle.

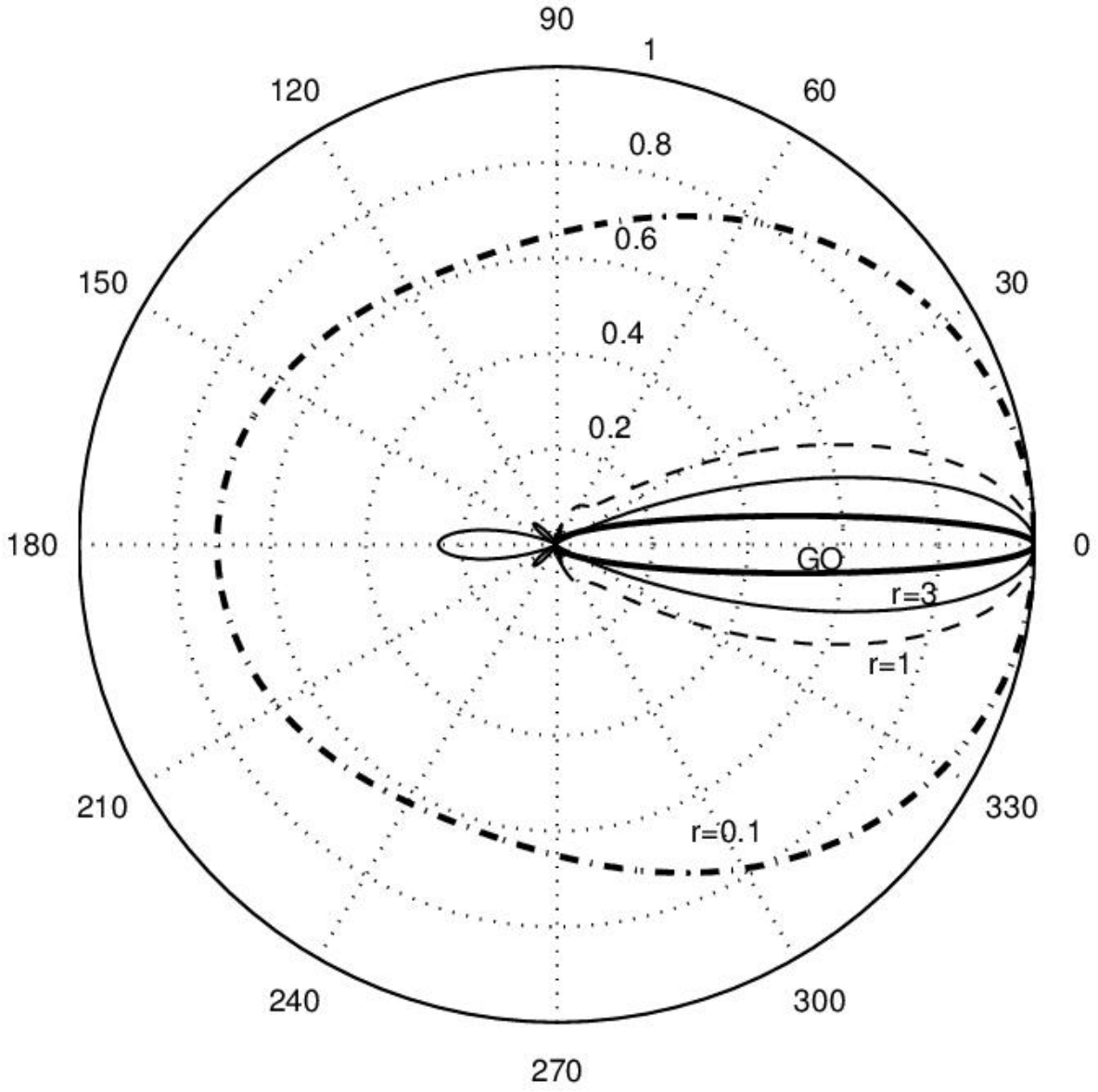

Figure 6. Comparison between the far-field pattern $\left|P^{(e)}(v)\right|^2$ given by (Equation 3.21) and the geometrical optics solution $p(v)$ of (Equation 3.20) computed for an ellipse with $u_1 = 0.5$. The values are normalized to their maxima and plotted on a linear scale. The results represent: far-field pattern for $r = 0.1$ or $c = 0.279$ (dash-dot line); far-field pattern for $r = 1$ or $c = 2.786$ (dashed line); far-field pattern for $r = 3$ or $c = 8.358$ (thin solid line); and, geometrical optics solution (thick solid line, $r = \infty$).

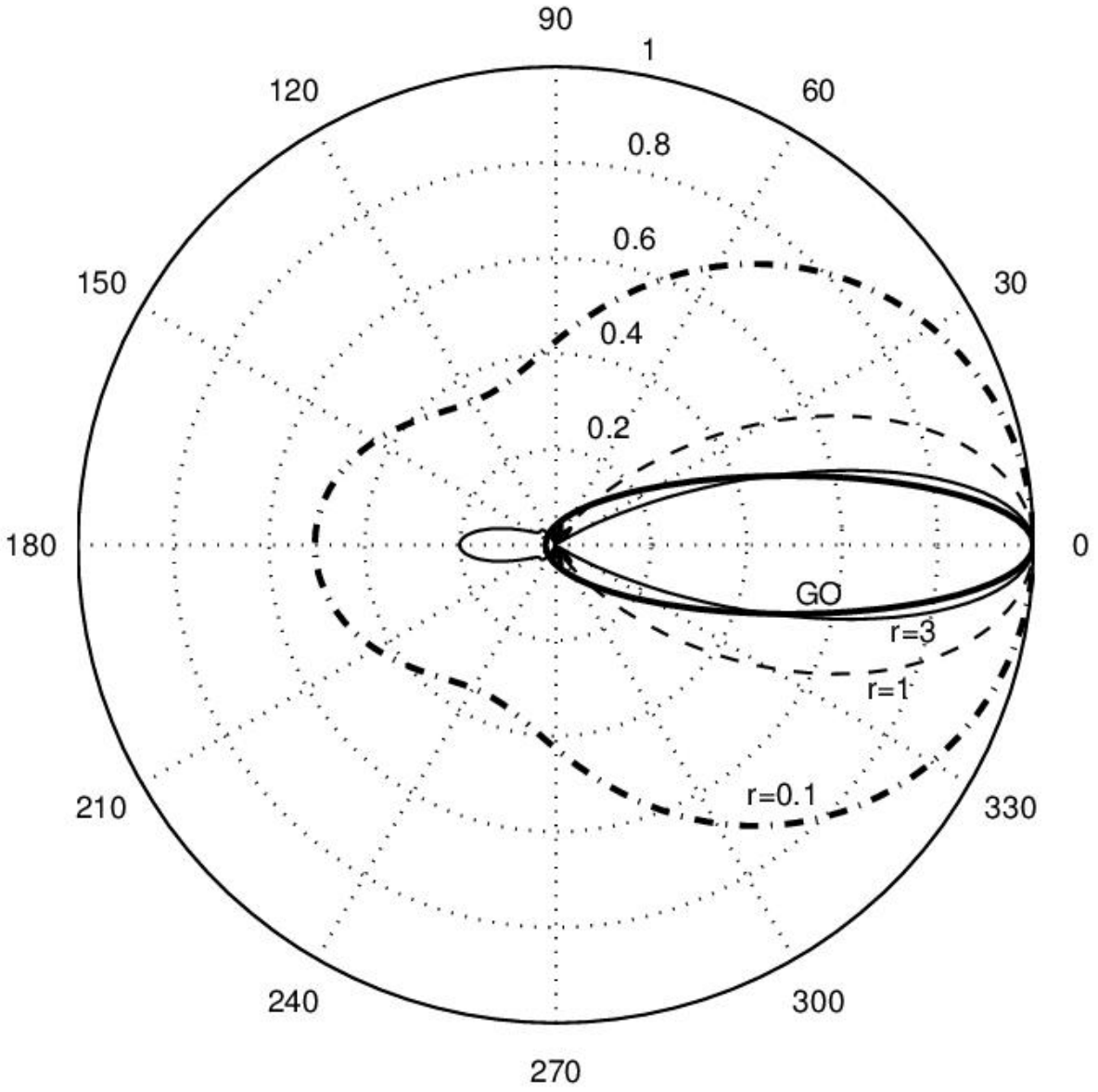

Figure 7. Comparison between the far-field pattern $\left|P^{(e)}(v)\right|^2$ given by (Equation 3.21) and the geometrical optics solution $p(v)$ of (Equation 3.20) computed for an ellipse with $u_1 = 0.8$. The values are normalized to their maxima and plotted on a linear scale. The results represent: far-field pattern for $r = 0.1$ or $c = 0.235$ (dash-dot line); far-field pattern for $r = 1$ or $c = 2.348$ (dashed line); far-field pattern for $r = 3$ or $c = 7.047$ (thin solid line); and, geometrical optics solution (thick solid line, $r = \infty$).

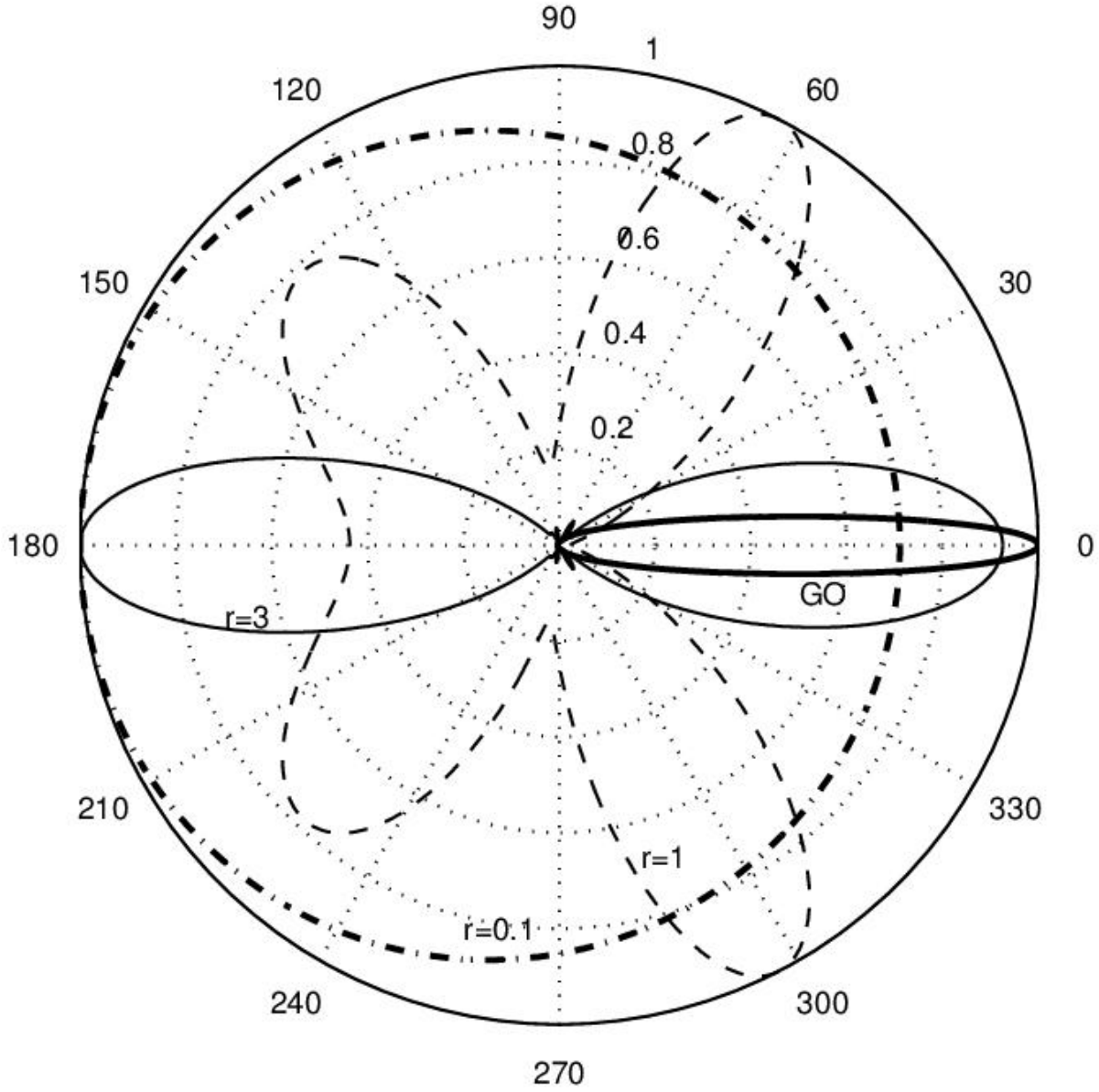

Figure 8. Comparison between the far-field pattern $\left|P^{(h)}(v)\right|^2$ and the geometrical optics solution $p(v)$ of (Equation 3.20) computed for an ellipse with $u_1 = 0.5$. The values are normalized to their maxima and plotted on a linear scale. The results represent: far-field pattern for $r = 0.1$ or $c = 0.235$ (dash-dot line); far-field pattern for $r = 1$ or $c = 2.348$ (dashed line); far-field pattern for $r = 3$ or $c = 7.047$ (thin solid line); and, geometrical optics solution (thick solid line, $r = \infty$).

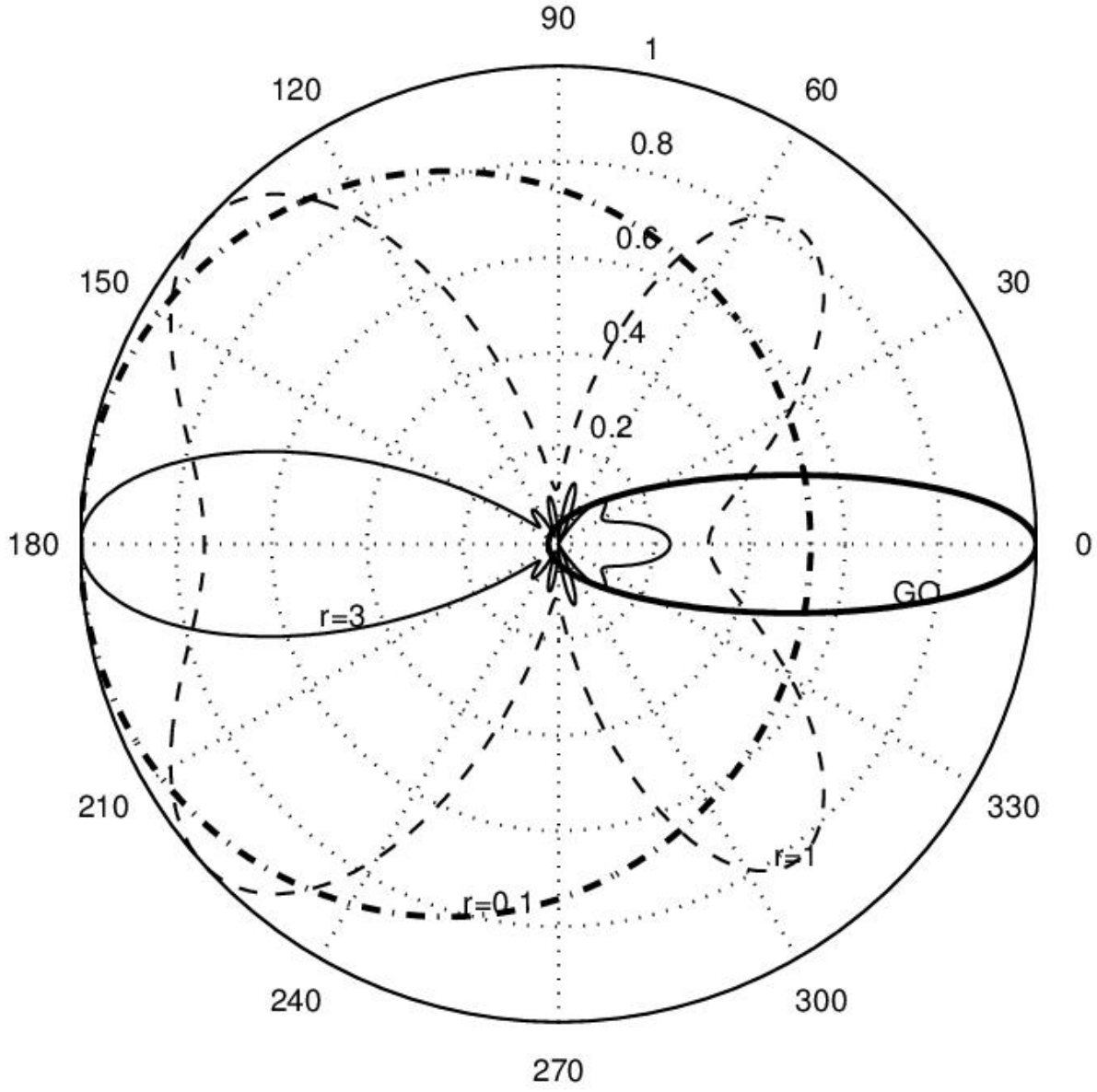

Figure 9. Comparison between the far-field pattern $\left|P^{(h)}(v)\right|^2$ and the geometrical optics solution $p(v)$ of (Equation 3.20) computed for an ellipse with $u_1 = 0.8$. The values are normalized to their maxima and plotted on a linear scale. The results represent: far-field pattern for $r = 0.1$ or $c = 0.235$ (dash-dot line); far-field pattern for $r = 1$ or $c = 2.348$ (dashed line); far-field pattern for $r = 3$ or $c = 7.047$ (thin solid line); and, geometrical optics solution (thick solid line, $r = \infty$).

3.5 Conclusions

The exact electromagnetic solution for the two-dimensional problem of a DNG lens fed by a line source located at one focal point was compared with the geometrical optics solution of the same problem. The numerical comparison show that the agreement with the geometrical optics solution improves for electrically large ellipses and, for the same value of the ratio r, the agreement is better when the ellipse has a smaller eccentricity.

This solution extends also the list of exact canonical solutions of boundary value electromagnetic scattering problems involving metamaterials.

CHAPTER 4

ELECTROMAGNETIC SCATTERING BY A SEMIELLIPTICAL TRENCH FILLED WITH DNG METAMATERIAL

4.1 INTRODUCTION

An exact solution to boundary-value problems of plane wave scattering by a semielliptical trench filled with double negative (DNG) metamaterial is presented. The DNG material has real and negative refractive index. The medium surrounding the cylinder is double-positive (DPS) having real but positive refractive index. Both media have the same intrinsic impedance value ($Z_1 = Z_2$).

4.2 GEOMETRY OF THE PROBLEM

A cross-sectional view of the structure in a plane $z =$ constant is shown in Figure 10.

Outside the semielliptical trench $u = u_1$, the electric permittivity is ε and the magnetic permeability is μ, whereas inside the trench the same quantities become $-\varepsilon$ and $-\mu$, respectively.

The wave vector is $k = \sqrt{\varepsilon\mu}$ outside the ellipse and $k = -\sqrt{\varepsilon\mu}$ inside the ellipse. We define a dimensionless parameter $c = kd/2$ in the DPS material outside the trench and $-c$ inside the trench of DNG material. The intrinsic impedance $Z = \sqrt{\mu/\varepsilon}$ is the same inside and outside the trench.

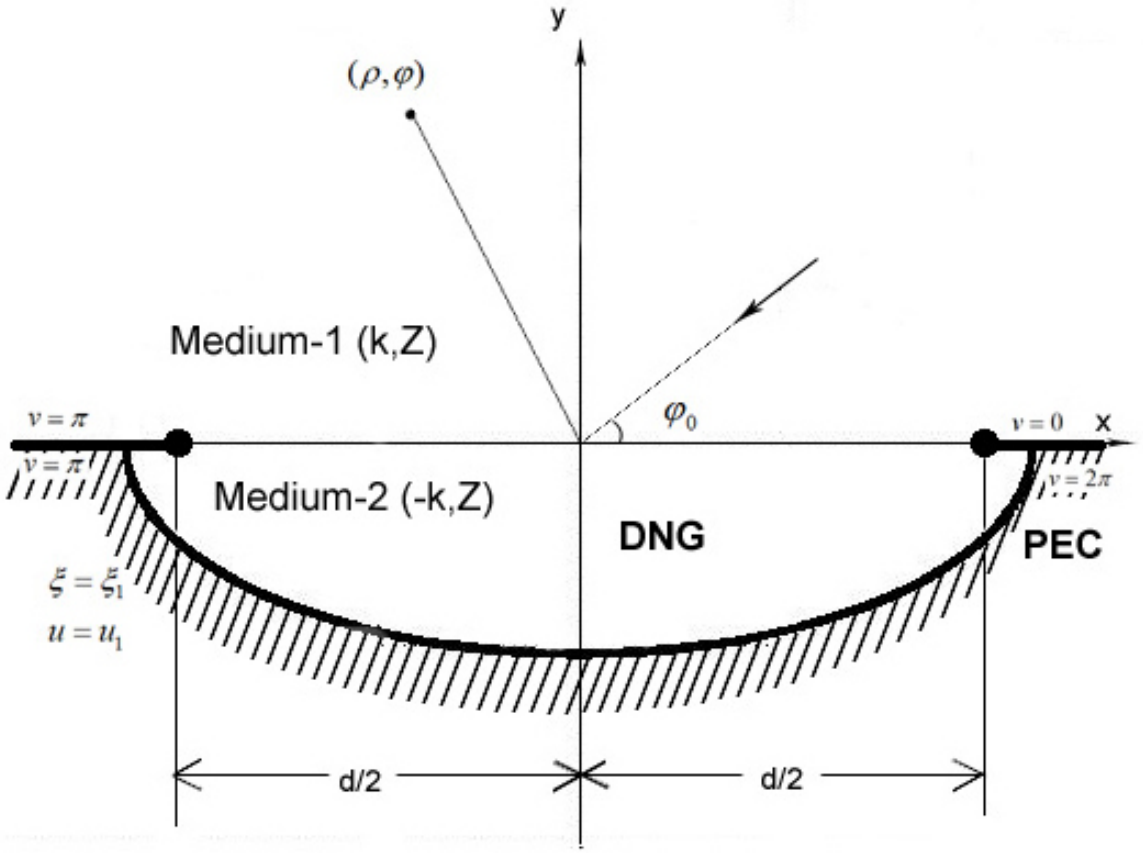

Figure 10. Geometry of the problem.

4.3 PLANE WAVE INCIDENCE

4.3.1 E-polarization

Consider a plane wave incident perpendicularly to the cylinder axis and polarized parallel to z-axis , with primary electric field

$$\boldsymbol{E}^i = \hat{z} E^i_{1z}. \tag{4.1}$$

The incident field will be same as in Equation 2.2

$$E_{1z}^{i} = \sqrt{8\pi} \sum_{m=0}^{\infty} j^{m} \left[\frac{1}{N_m^{(e)}} \mathrm{Re}_m^{(1)}(c,u)\mathrm{Se}_m(c,v)\mathrm{Se}_m(c,\varphi_0) + \frac{1}{N_m^{(o)}} \mathrm{Ro}_m^{(1)}(c,u)\mathrm{So}_m(c,v)\mathrm{So}_m(c,\varphi_0) \right]. \tag{4.2}$$

The total electric field in medium 1 can be written as

$$E_{1z} = E_{1z}^{i} + E_{1z}^{r} + E_{1z}^{d} \tag{4.3}$$

where E_{1z}^{r} is the reflected field by the metallic plane at $y = 0$ and E_{1z}^{d} is the diffracted field by the trench (1). Reflected electric field can be written by using method of images as,

$$E_{1z}^{r} = -\sqrt{8\pi} \sum_{m=0}^{\infty} j^{m} \left[\frac{1}{N_m^{(e)}} \mathrm{Re}_m^{(1)}(c,u)\mathrm{Se}_m(c,v)\mathrm{Se}_m(c,\varphi_0) - \frac{1}{N_m^{(o)}} \mathrm{Ro}_m^{(1)}(c,u)\mathrm{So}_m(c,v)\mathrm{So}_m(c,\varphi_0) \right] \tag{4.4}$$

hence,

$$E_{1z}^{i} + E_{1z}^{r} = 2\sqrt{8\pi} \sum_{m=0}^{\infty} \frac{j^{m}}{N_m^{(o)}} \mathrm{Ro}_m^{(1)}(c,u)\mathrm{So}_m(c,v)\mathrm{So}_m(c,\varphi_0). \tag{4.5}$$

The diffracted field can be written as,

$$E_z^d = \sqrt{8\pi} \sum_{m=0}^{\infty} c_m \frac{j^m}{N_m^{(o)}} \mathrm{Ro}_m^{(4)}(c,u)\mathrm{So}_m(c,v)\mathrm{So}_m(c,\varphi_0). \tag{4.6}$$

The total electric field inside the trench is

$$E_{2z} = \sqrt{8\pi} \sum_{m=0}^{\infty} j^m \frac{a_m}{N_m^{(o)}} \left[\mathrm{Ro}_m^{(1)}(-c,u) - \frac{\mathrm{Ro}_m^{(1)}(-c,u_1)}{\mathrm{Ro}_m^{(4)}(-c,u_1)} \mathrm{Ro}_m^{(4)}(-c,u) \right] \mathrm{So}_m(c,v)\mathrm{So}_m(c,\varphi_0). \tag{4.7}$$

We can find the modal coefficients by applying the boundary conditions. The tangential component of the total electric and magnetic fields in both media are equal for $u = 0$

$$(E_{1z})_{u=0} = (E_{2z})_{u=0}, (H_{1v})_{u=0} = -(H_{2v})_{u=0}. \tag{4.8}$$

Applying these boundary conditions yields the modal coefficients a_m and c_m as

$$a_m \frac{\mathrm{Ro}_m^{(1)}(-c,u_1)}{\mathrm{Ro}_m^{(4)}(-c,u_1)} \mathrm{Ro}_m^{(4)}(-c,0) + c_m \mathrm{Ro}_m^{(4)}(c,0) = 0, \tag{4.9}$$

$$a_m \left[\mathrm{Ro}_m^{(1)\prime}(-c,0) - \frac{\mathrm{Ro}_m^{(1)}(-c,u_1)}{\mathrm{Ro}_m^{(4)}(-c,u_1)} \mathrm{Ro}_m^{(4)\prime}(-c,0) \right] - c_m \mathrm{Ro}_m^{(4)\prime}(c,0) = 2\mathrm{Ro}_m^{(1)\prime}(-c,0) \tag{4.10}$$

where $'$ means $\frac{\partial}{\partial u}$. Hence

$$c_m = \frac{2}{\Delta_m} \frac{\mathrm{Ro}_m^{(1)}(-c,u_1)}{\mathrm{Ro}_m^{(4)}(-c,u_1)} \mathrm{Ro}_m^{(4)}(-c,0) \mathrm{Ro}_m^{(1)\prime}(c,0) \tag{4.11}$$

where

$$\begin{aligned} \Delta_m = & \frac{\mathrm{Ro}_m^{(1)}(-c,u_1)}{\mathrm{Ro}_m^{(4)}(-c,u_1)} \left[\mathrm{Ro}_m^{(4)}(c,0) \mathrm{Ro}_m^{(4)\prime}(-c,0) - \mathrm{Ro}_m^{(4)}(-c,0) \mathrm{Ro}_m^{(4)\prime}(c,0) \right] - \\ & \mathrm{Ro}_m^{(4)}(c,0) \mathrm{Ro}_m^{(1)\prime}(-c,0). \end{aligned} \tag{4.12}$$

Detailed procedure finding the modal coefficients a_m and c_m is given in Appendix-C.

We can obtain the bistatic RCS as

$$\sigma^{(e)}(\phi) = \frac{4}{k} \left| P^{(e)}(\phi) \right|^2 = \frac{2\lambda}{\pi} \left| P^{(e)}(\phi) \right|^2 \tag{4.13}$$

where the far field coefficient $P^{(e)}(\phi)$ is

$$P^{(e)}(\phi) = 2\pi \sum_{m=0}^{\infty} c_m \frac{(-1)^m}{N_m^{(o)}} \mathrm{So}_m(c,v)\mathrm{So}_m(c,\varphi_0). \tag{4.14}$$

4.3.2 H-polarization

The analysis is similar to that for E-polarization. The incident magnetic field is

$$\begin{aligned} H_{1z}^i =& \exp[jk(x\cos\varphi_0 + y\sin\varphi_0)] \\ =& \sqrt{8\pi} \sum_{m=0}^{\infty} \left[\frac{j^m}{N_m^{(e)}} \mathrm{Re}_m^{(1)}(c,u)\mathrm{Se}_m(c,v)\mathrm{Se}_m(c,\varphi_0) + \frac{j^m}{N_m^{(o)}} \mathrm{Ro}_m^{(1)}(c,u)\mathrm{So}_m(c,v)\mathrm{So}_m(c,\varphi_0) \right]. \end{aligned} \tag{4.15}$$

The total magnetic field in medium 1 is

$$H_{1z} = H_{1z}^i + H_{1z}^r + H_{1z}^d. \tag{4.16}$$

By image theory,

$$H_{1z}^r = \sqrt{8\pi} \sum_{m=0}^{\infty} \left[\frac{j^m}{N_m^{(e)}} \mathrm{Re}_m^{(1)}(c,u)\mathrm{Se}_m(c,v)\mathrm{Se}_m(c,\varphi_0) - \frac{j^m}{N_m^{(o)}} \mathrm{Ro}_m^{(1)}(c,u)\mathrm{So}_m(c,v)\mathrm{So}_m(c,\varphi_0) \right]. \tag{4.17}$$

Hence,

$$H_{1z}^i + H_{1z}^r = 2\sqrt{8\pi}\sum_{m=0}^{\infty}\frac{j^m}{N_m^{(e)}}\mathrm{Re}_m^{(1)}(c,u)\mathrm{Se}_m(c,v)\mathrm{Se}_m(c,\varphi_0). \tag{4.18}$$

The diffracted magnetic field can be written,

$$H_{1z}^d = \sqrt{8\pi}\sum_{m=0}^{\infty} d_m\frac{j^m}{N_m^{(e)}}\mathrm{Re}_m^{(4)}(c,u)\mathrm{Se}_m(c,v)\mathrm{Se}_m(c,\varphi_0). \tag{4.19}$$

The total magnetic field in medium 2 is

$$H_{2z} = \sqrt{8\pi}\sum_{m=0}^{\infty} j^m\frac{b_m}{N_m^{(e)}}\left[\mathrm{Re}_m^{(1)}(-c,u) - \frac{\mathrm{Re}_m^{(1)\prime}(-c,u_1)}{\mathrm{Re}_m^{(4)\prime}(-c,u_1)}\mathrm{Re}_m^{(4)}(-c,u)\right]\mathrm{Se}_m(c,v)\mathrm{Se}_m(c,\varphi_0). \tag{4.20}$$

The boundary conditions are

$$(H_{1z})_{u=0} = (H_{2z})_{u=0}, (E_{1v})_{u=0} = -(E_{2v})_{u=0}. \tag{4.21}$$

The modal coefficients can be found from

$$b_m \left[\mathrm{Re}_m^{(1)}(-c,0) - \frac{\mathrm{Re}_m^{(1)\prime}(-c,u_1)}{\mathrm{Re}_m^{(4)\prime}(-c,u_1)} \mathrm{Re}_m^{(4)}(-c,0) \right] - d_m \mathrm{Re}_m^{(4)}(c,0) = 2\mathrm{Re}_m^{(1)}(c,0), \tag{4.22}$$

$$b_m \frac{\mathrm{Re}_m^{(1)\prime}(-c,u_1)}{\mathrm{Re}_m^{(4)\prime}(-c,u_1)} \mathrm{Re}_m^{(4)\prime}(-c,0) + d_m \mathrm{Re}_m^{(4)\prime}(c,0) = 0. \tag{4.23}$$

These equations will give us b_m and d_m

$$d_m = \frac{2}{\Gamma_m} \frac{\mathrm{Re}_m^{(1)\prime}(-c,\xi_1)}{\mathrm{Re}_m^{(4)\prime}(-c,\xi_1)} \mathrm{Re}_m^{(4)\prime}(-c,0) \mathrm{Re}_m^{(1)}(c,0) \tag{4.24}$$

where

$$\Gamma_m = \frac{\mathrm{Re}_m^{(1)\prime}(-c,u_1)}{\mathrm{Ro}_m^{(4)\prime}(-c,u_1)} \left[\mathrm{Re}_m^{(4)}(-c,0) \mathrm{Re}_m^{(4)\prime}(c,0) - \mathrm{Re}_m^{(4)}(c,0) \mathrm{Re}_m^{(4)\prime}(-c,0) \right] - \mathrm{Re}_m^{(4)\prime}(c,0) \mathrm{Re}_m^{(1)}(-c,0). \tag{4.25}$$

The normalized bistatic RCS is

$$\frac{\sigma^{(h)}(\phi)}{\lambda} = \frac{2}{\pi} \left| P^{(h)}(\phi) \right|^2 \tag{4.26}$$

where the far field coefficient $P^{(h)}(\phi)$ is

$$P^{(h)}(\phi) = 2\pi \sum_{m=0}^{\infty} d_m \frac{(-1)^m}{N_m^{(e)}} \mathrm{Se}_m(c, v)\mathrm{Se}_m(c, \varphi_0). \tag{4.27}$$

4.4 NUMERICAL RESULTS

The scattering effect of trench can be investigated easily by looking at the normalized bistatic RCS as given by Equation 4.13 and Equation 4.26.

The value of c is controlled by the frequency and the focal distance d

$$c = \frac{kd}{2} = \frac{\pi d}{\lambda}. \tag{4.28}$$

Fig Figure 11 and Figure 12 show the polar plots for two different u_1 values. The incidence angle is $\varphi_0 = \pi/4$ and $u_1 = 0.5$ in Fig Figure 11 and $u_1 = 0.75$ in Fig Figure 12. To analyze the effect of c , we have used 4 different c values: $c = 0.5, c = 0.75, c = 1, c = 2$.

Similarly, we can plot the normalized RCS for H-polarization. Again, we use the incidence angle $\varphi_0 = \pi/4$ and $u_1 = 0.5$ in Fig Figure 13 and $u_1 = 0.75$ in Fig Figure 14. To analyze the effect of c , we have used 4 different c values: $c = 0.5, c = 0.75, c = 1, c = 2$ again.

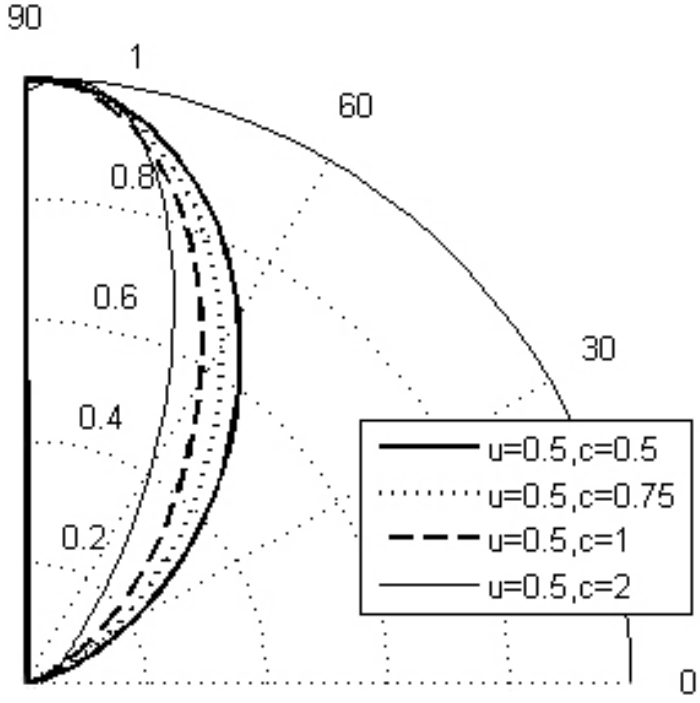

Figure 11. Normalized RCS for E-polarization with $u_1 = 0.5$ and $c = 0.5, 0.75, 1.0, 2.0$

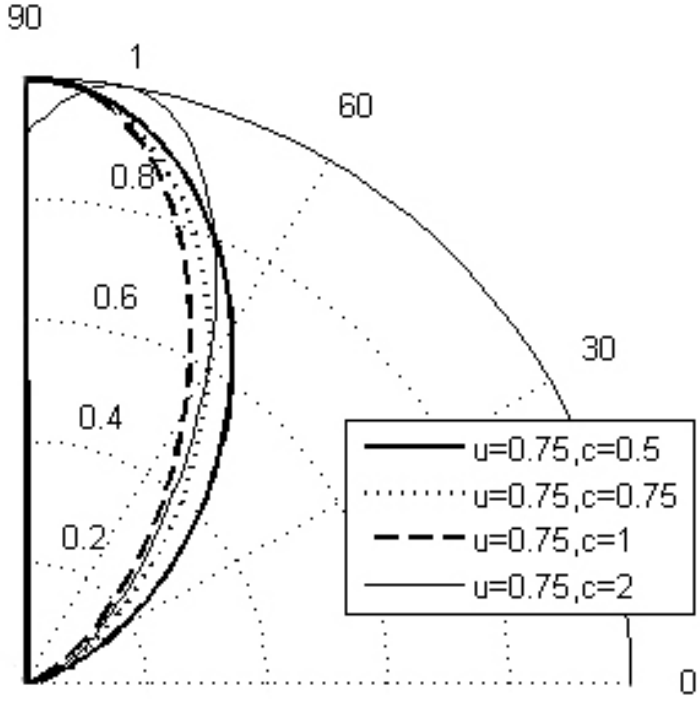

Figure 12. Normalized RCS for E-polarization with $u_1 = 0.75$ and $c = 0.5, 0.75, 1.0, 2.0$

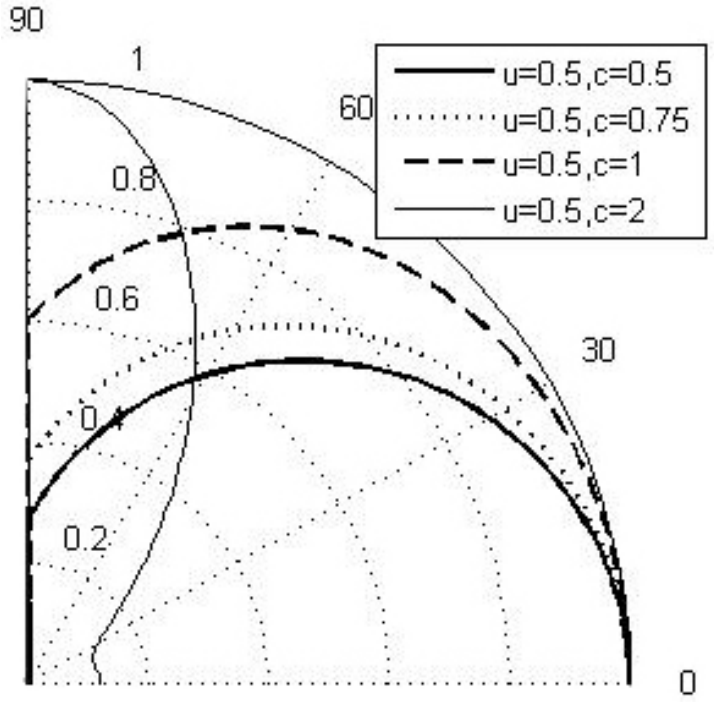

Figure 13. Normalized RCS for H-polarization with $u_1 = 0.5$ and $c = 0.5, 0.75, 1.0, 2.0$

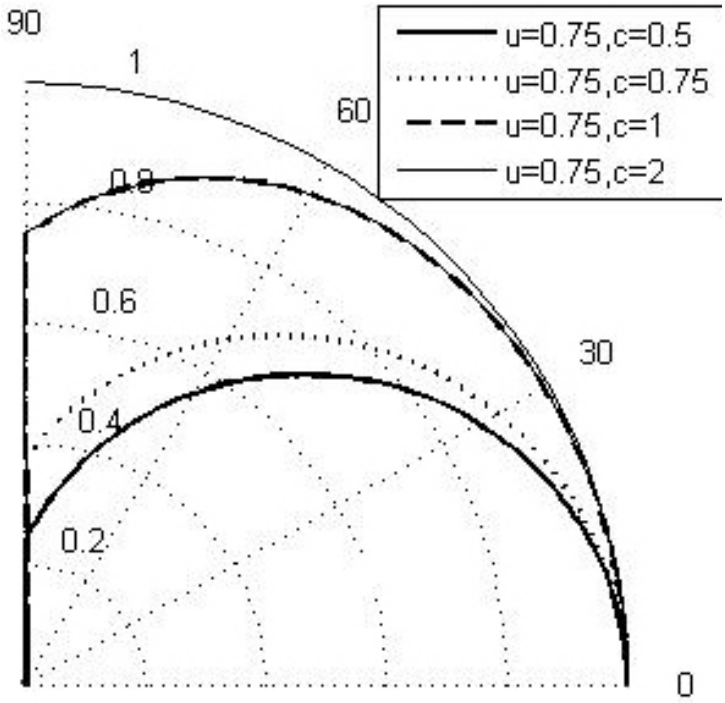

Figure 14. Normalized RCS for H-polarization with $u_1 = 0.75$ and $c = 0.5, 0.75, 1.0, 2.0$

CHAPTER 5

RADIATION OF A LINE SOURCE BY A SLOTTED SEMIELLIPTICAL TRENCH FILLED WITH DNG METAMATERIAL

5.1 INTRODUCTION

The geometry analyzed in this chapter consist of a metallic trench, or channel, of semielliptical cross section slotted along the inter focal strip and flush-mounted under a metallic infinite plane. The trench is filled with double-negative metamaterial, whose electric permittivity and permeability are real and of opposite sign of the corresponding parameters of the material (e.g. air) occupying the half-space above the trench.

5.2 GEOMETRY OF THE PROBLEM

A cross-sectional view of the structure in a plane $z =$ constant is shown in Figure 20.

Outside the semielliptical trench $u = u_1$, the electric permittivity is ε and the magnetic permeability is μ, whereas inside the trench the same quantities become $-\varepsilon$ and $-\mu$, respectively. The wave vector is $k = \sqrt{\varepsilon\mu}$ outside the ellipse and $k = -\sqrt{\varepsilon\mu}$ inside the ellipse. We define a dimensionless parameter $c = kd/2$ in the DPS material outside the trench and $-c$ inside the trench of DNG material. The intrinsic impedance $Z = \sqrt{\mu/\varepsilon}$ is the same inside and outside the trench.

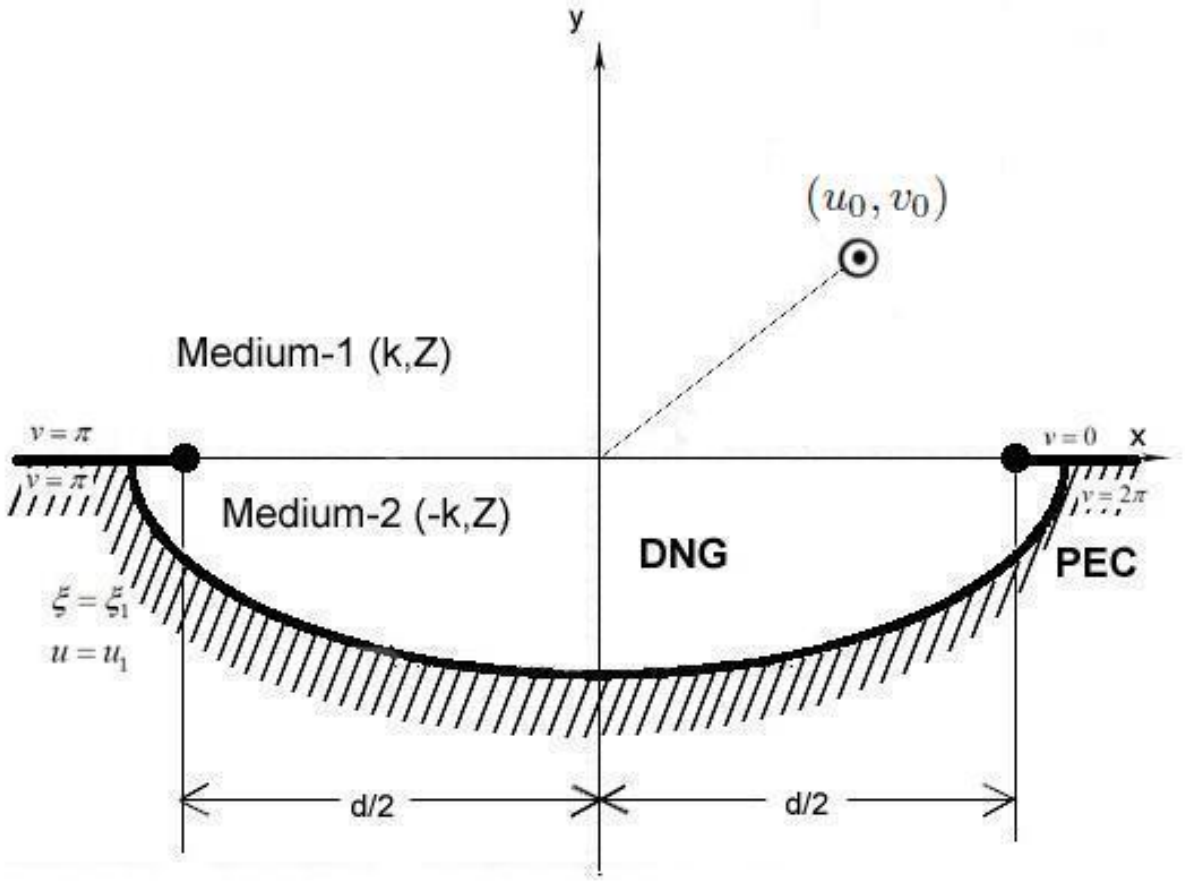

Figure 15. Geometry of the problem.

5.3 LINE SOURCE INCIDENCE

5.3.1 E-Polarization

Consider an electric line source parallel to the z-axis and located at $(x_0, y_0) \equiv (u_0, v_0) \equiv (\xi_0, \eta_0)$ whose primary electric field is

$$\boldsymbol{E}^i = \hat{z} E_z^i = \hat{z} H_0^{(2)}(kR) \tag{5.1}$$

where

$$R = \sqrt{(x - x_0)^2 + (y - y_0)^2} \tag{5.2}$$

is the distance between the line source and the observation point $(x, y) \equiv (u, v)$. The incident field may be expanded in a series of elliptic-cylinder functions (11):

$$E_{1z}^i = H_0^{(2)}(kR) = 4 \sum_{m=0}^{\infty} \left[\frac{1}{N_m^{(e)}} \mathrm{Re}_m^{(1)}(c, u_<) \mathrm{Re}_m^{(4)}(c, u_>) \mathrm{Se}_m(c, v_0) \mathrm{Se}_m(c, v) + \right.$$
$$\left. \frac{1}{N_m^{(o)}} \mathrm{Ro}_m^{(1)}(c, u_<) \mathrm{Ro}_m^{(4)}(c, u_>) \right] \mathrm{So}_m(c, v_0) \mathrm{So}_m(c, v) \tag{5.3}$$

where $u_<$ ($u_>$) is the smaller (larger) between u and u_0.

Let us first examine the case of a line source in the half-space above the channel (i.e., $0 < v_0 < \pi$).

The total field in the half-space $y \geq 0$ is

$$E_{1z} = E_{1z}^i + E_{1z}^r + E_{1z}^d \tag{5.4}$$

where E_{1z}^r is the field reflected by the infinite metal plane at $y = 0$ when no channel is present, and E_{1z}^d is the diffracted field due to the presence of the cavity-backed slot By considering the image of the line source into the ground plane, it is found that

$$E_{1z}^i + E_{1z}^r = H_0^{(2)}(kR) - H_0^{(2)}(k\tilde{R}) \tag{5.5}$$

where

$$\tilde{R} = \sqrt{(x - x_0)^2 + (y + y_0)^2} \tag{5.6}$$

is the distance between the observation point. As a result we can write,

$$E^i_{1z} + E^r_{1z} = 8 \sum_{m=0}^{\infty} \frac{1}{N^{(o)}_m} \mathrm{Ro}^{(1)}_m(c, u_<) \mathrm{Ro}^{(4)}_m(c, u_>) \mathrm{So}_m(c, v_0) \mathrm{So}_m(c, v). \tag{5.7}$$

The diffracted field E^d_{1z} in $y \geq 0$ and the total electric field inside the trench are given by,

$$E^d_{1z} = 4 \sum_{m=0}^{\infty} \frac{a_m}{N^{(o)}_m} \mathrm{Ro}^{(4)}_m(c, u_0) \mathrm{Ro}^{(4)}_m(c, u) \mathrm{So}_m(c, v_0) \mathrm{So}_m(c, v), \tag{5.8}$$

$$\begin{aligned} E_{2z} =& 4 \sum_{m=0}^{\infty} \frac{c_m}{N^{(o)}_m} \mathrm{Ro}^{(4)}_m(-c, u_0) \left[\mathrm{Ro}^{(1)}_m(-c, u) - \frac{\mathrm{Ro}^{(1)}_m(-c, u_1)}{\mathrm{Ro}^{(4)}_m(-c, u_1)} \mathrm{Ro}^{(4)}_m(-c, u) \right] \times \\ & \mathrm{So}_m(-c, v_0) \mathrm{So}_m(-c, v). \end{aligned} \tag{5.9}$$

The unknown modal coefficients a_m and c_m are determined by imposing the continuity of the total tangential electric and magnetic fields across the interface $(\xi = 1) \equiv (u = 0)$.

$$c_m = \frac{-2\mathrm{Ro}^{(4)}_m(c, u_0) \mathrm{Ro}^{(4)}_m(c, 0) \mathrm{Ro}^{(1)'}_m(c, 0)}{\Delta_m}, \tag{5.10}$$

$$a_m = \frac{-2\mathrm{Ro}^{(4)}_m(-c, u_0) \mathrm{Ro}^{(4)}_m(-c, 0) \mathrm{Ro}^{(1)'}_m(c, 0)}{\Delta_m} \frac{\mathrm{Ro}^{(1)}_m(-c, u_1)}{\mathrm{Ro}^{(4)}_m(-c, u_1)}, \tag{5.11}$$

where

$$\Delta_m = \mathrm{Ro}_m^{(4)}(-c,u_0)\left[\mathrm{Ro}_m^{(4)}(c,0)\mathrm{Ro}_m^{(1)\prime}(-c,0) - \frac{\mathrm{Ro}_m^{(1)}(-c,u_1)}{\mathrm{Ro}_m^{(4)}(-c,u_1)}\mathrm{Ro}_m^{(4)}(c,0)\mathrm{Ro}_m^{(4)\prime}(-c,0) + \frac{\mathrm{Ro}_m^{(1)}(-c,u_1)}{\mathrm{Ro}_m^{(4)}(-c,u_1)}\mathrm{Ro}_m^{(4)\prime}(c,0)\mathrm{Ro}_m^{(4)}(-c,0)\right]. \tag{5.12}$$

The behavior of the field scattered by the DNG cavity may be examined at large distance by considering

$$E_{1z}^d|_{\xi\to\infty, Im(c)<0} \approx \frac{e^{-jk\rho}}{\sqrt{k\rho}} P^{(e)}(\phi;u_0,v_0), \tag{5.13}$$

where

$$P^{(e)}(\phi;u_0,v_0) = 4\sum_{m=0}^{\infty}\frac{j^m}{N_m^{(o)}} a_m \mathrm{Ro}_m^{(4)}(c,u_0)\mathrm{So}_m(c,v_0)\mathrm{So}_m(c,\phi) \tag{5.14}$$

is a far-field coefficients that depends not only on the angle of observation ϕ but also on the source location (u_0, v_0).

Let us now consider the case of a line source located inside the channel ($u_0 < u_1, \pi < v_0 < 2\pi$). The total electric field inside the channel is

$$E_{2z} = E_{2z}^i + E_{2z}^r + E_{2z}^s \tag{5.15}$$

where E^i_{2z} is the incident field given by (Equation 5.3). E^r_{2z} is the reflected field when no slot is present. As a result $E^i_{2z} + E^r_{2z}$ is still given by (Equation 5.7). However, E^s_{2z} contains a linear combination of $\mathrm{Ro}^{(1)}_m(-c,u)$ and $\mathrm{Ro}^{(4)}_m(-c,u)$. The infinite series for the total field E_{1z} in $y > 0$ must satisfy the radiation condition, hence contains only $\mathrm{Ro}^{(4)}_m(c,u)$. The total fields for both media are

$$E_{2z} = 4\sum_{m=0}^{\infty} \frac{1}{N^{(o)}_m}\left[2\mathrm{Ro}^{(1)}_m(-c,u_<)\mathrm{Ro}^{(4)}_m(-c,u_>) + e_m\mathrm{Ro}^{(1)}_m(-c,u) + f_m\mathrm{Ro}^{(4)}_m(-c,u)\right]\times \mathrm{So}_m(c,v_0)\mathrm{So}_m(c,v), \tag{5.16}$$

$$E_{1z} = 4\sum_{m=0}^{\infty} \frac{g_m}{N^{(o)}_m}\mathrm{Ro}^{(4)}_m(c,u)\mathrm{So}_m(c,v_0)\mathrm{So}_m(c,v). \tag{5.17}$$

Imposing the boundary conditions will give us the modal coefficients e_m and f_m as,

$$e_m = \frac{\Delta e_m}{\Delta}, \tag{5.18}$$

$$f_m = \frac{\Delta f_m}{\Delta}, \tag{5.19}$$

$$g_m = -\frac{\mathrm{Ro}^{(4)}_m(-c,0)}{\mathrm{Ro}^{(4)}_m(c,0)} f_m, \tag{5.20}$$

where

$$\Delta e_m = 2\mathrm{Ro}_m^{(4)}(-c,u_1)\left[-\mathrm{Ro}_m^{(1)}(-c,u_0)\left(\mathrm{Ro}_m^{(4)\prime}(-c,0)-\frac{\mathrm{Ro}_m^{(4)}(-c,0)}{\mathrm{Ro}_m^{(4)}(c,0)}\right)+\mathrm{Ro}_m^{(1)\prime}(-c,0)\mathrm{Ro}_m^{(4)}(-c,u_0)\right], \tag{5.21}$$

$$\Delta f_m = -2\mathrm{Ro}_m^{(1)\prime}(-c,0)\left[\mathrm{Ro}_m^{(1)}(-c,u_1)\mathrm{Ro}_m^{(4)}(-c,u_0)-\mathrm{Ro}_m^{(1)}(-c,u_0)\mathrm{Ro}_m^{(4)}(-c,u_1)\right], \tag{5.22}$$

$$\Delta = \mathrm{Ro}_m^{(1)}(-c,u_1)\left[\mathrm{Ro}_m^{(4)\prime}(-c,0)-\frac{\mathrm{Ro}_m^{(4)}(-c,0)}{\mathrm{Ro}_m^{(4)}(c,0)}\mathrm{Ro}_m^{(4)\prime}(c,0)\right]-\mathrm{Ro}_m^{(1)\prime}(-c,0)\mathrm{Ro}_m^{(4)}(-c,u_1). \tag{5.23}$$

5.3.2 H-Polarization

The analysis is similar to that for E-Polarization. Consider an magnetic line source parallel to the z-axis and located at $(x_0,y_0)\equiv(u_0,v_0)\equiv(\xi_0,\eta_0)$, Magnetic field is given by;

$$H_{1z}^i = 4\sum_{m=0}^{\infty}\left[\frac{1}{N_m^{(e)}}\mathrm{Re}_m^{(1)}(c,u_<)\mathrm{Re}_m^{(4)}(c,u_>)\mathrm{Se}_m(c,v_0)\mathrm{Se}_m(c,v)+\frac{1}{N_m^{(o)}}\mathrm{Ro}_m^{(1)}(c,u_<)\mathrm{Ro}_m^{(4)}(c,u_>)\right]\mathrm{So}_m(c,v_0)\mathrm{So}_m(c,v) \tag{5.24}$$

where $u_<$ ($u_>$) is the smaller (larger) between u and u_0. The magnetic source located outside of the trench so $u_< = u$ and $u_> = u_0$. The total magnetic field in the half-space $y \geq 0$ is

$$H_{1z} = H_{1z}^i + H_{1z}^r + H_{1z}^d \tag{5.25}$$

$$H_{1z} = 4\sum_{m=0}^{\infty} \frac{1}{N_m^{(e)}} \left[2\mathrm{Re}_m^{(1)}(c, u_<)\mathrm{Re}_m^{(4)}(c, u_>) + \tilde{a}_m \mathrm{Re}_m^{(4)}(c, u_0)\mathrm{Re}_m^{(4)}(c, u)\right] \mathrm{Se}_m(c, v_0)\mathrm{Se}_m(c, v). \tag{5.26}$$

The total magnetic field inside the trench is given by,

$$H_{2z} = 4\sum_{m=0}^{\infty} \frac{\tilde{b}_m}{N_m^{(e)}} \mathrm{Re}_m^{(4)}(-c, u_0) \left[\mathrm{Re}_m^{(1)}(-c, u) - \frac{\mathrm{Re}_m^{(1)\prime}(-c, u_1)}{\mathrm{Re}_m^{(4)\prime}(-c, u_1)} \mathrm{Re}_m^{(4)}(-c, u)\right] \mathrm{Se}_m(c, v_0)\mathrm{Se}_m(c, v). \tag{5.27}$$

Modal coefficients $\tilde{a}_m$ and $\tilde{b}_m$ can be found by imposing the boundary conditions.

$$\tilde{a}_m = \frac{\Delta \tilde{a}_m}{\Delta}, \tag{5.28}$$

$$\tilde{b}_m = \frac{\Delta \tilde{b}_m}{\Delta} \tag{5.29}$$

where

$$\Delta\tilde{a}_m = 2\frac{\mathrm{Re}_m^{(4)}(-c,u_0)}{\mathrm{Re}_m^{(4)}(c,u_0)}\left[\left(\mathrm{Re}_m^{(1)}(-c,0) - \frac{\mathrm{Re}_m^{(1)\prime}(-c,u_1)}{\mathrm{Re}_m^{(4)\prime}(-c,u_1)}\mathrm{Re}_m^{(4)}(-c,0)\right)\mathrm{Re}_m^{(1)\prime}(c,0) - \left(\mathrm{Re}_m^{(1)\prime}(-c,0) - \frac{\mathrm{Re}_m^{(1)\prime}(-c,u_1)}{\mathrm{Re}_m^{(4)\prime}(-c,u_1)}\mathrm{Re}_m^{(4)\prime}(-c,0)\right)\mathrm{Re}_m^{(1)}(c,0)\right], \tag{5.30}$$

$$\Delta\tilde{b}_m = 2\left[\mathrm{Re}_m^{(1)}(c,0)\mathrm{Re}_m^{(4)\prime}(c,0) - \mathrm{Re}_m^{(1)\prime}(c,0)\mathrm{Re}_m^{(4)}(c,0)\right], \tag{5.31}$$

$$\Delta = \frac{\mathrm{Re}_m^{(4)}(-c,u_0)}{\mathrm{Re}_m^{(4)}(c,u_0)}\left[\left(\mathrm{Re}_m^{(1)\prime}(-c,0) - \frac{\mathrm{Re}_m^{(1)\prime}(-c,u_1)}{\mathrm{Re}_m^{(4)\prime}(-c,u_1)}\mathrm{Re}_m^{(4)\prime}(-c,0)\right)\mathrm{Re}_m^{(4)}(c,0) - \left(\mathrm{Re}_m^{(1)}(-c,0) - \frac{\mathrm{Re}_m^{(1)\prime}(-c,u_1)}{\mathrm{Re}_m^{(4)\prime}(-c,u_1)}\mathrm{Re}_m^{(4)}(-c,0)\right)\mathrm{Re}_m^{(4)\prime}(c,0)\right]. \tag{5.32}$$

5.4 NUMERICAL RESULTS

The scattering effect of trench can be easily investigated by looking at the square magnitude of the far-field coefficient given by (Equation 5.14)

$$\sigma^{(e)}(\phi;u_0,v_0) = \left|P^{(e)}(\phi;u_0,v_0)\right|^2. \tag{5.33}$$

The value of c is controlled by the frequency and the focal distance d:

$$c = \frac{kd}{2} = \frac{\pi d}{\lambda} \tag{5.34}$$

Figure 16 shows the far-field behavior when we move the line source in v-axis. Figure 18 and Figure 19 show the polar plots for four different u_1 and u_0 values. The location of the line source is (u_0, v_0) where we have used $v_0 = \pi/4$ and $c = 1$. To analyze the effect of c, we have used four different c values: $c = 1, 1.5, 2$ and 4 in Figure 17.

Details of the computation of Mathieu functions are given in (17; 18).

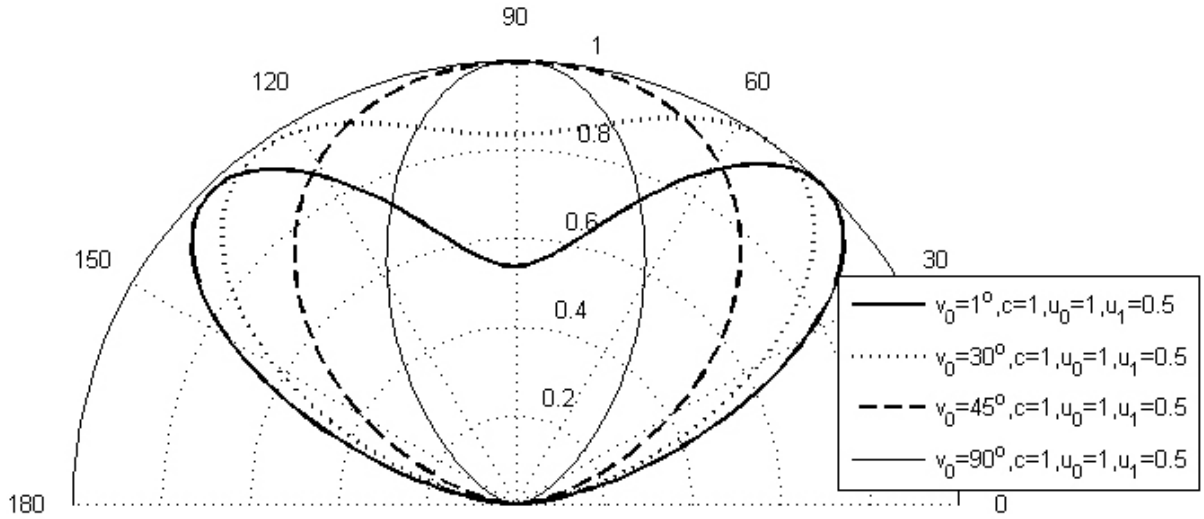

Figure 16. Far-field behavior, given by (Equation 5.14) for E-polarization with $v_0 = 1^o, 30^o, 45^o, 90^o, u_0 = 1,\ u_1 = 0.5$ and $c = 1$.

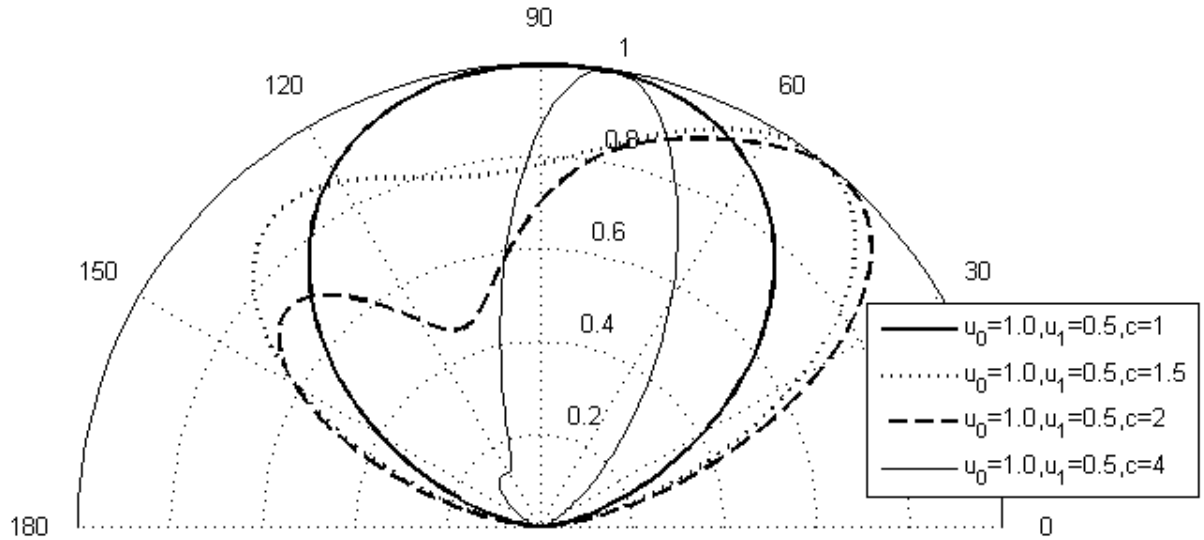

Figure 17. Far-field behavior, given by (Equation 5.14) for E-polarization with $v_0 = 45^o, u_0 = 1, u_1 = 0.5$ and $c = 1, 1.5, 2, 4$.

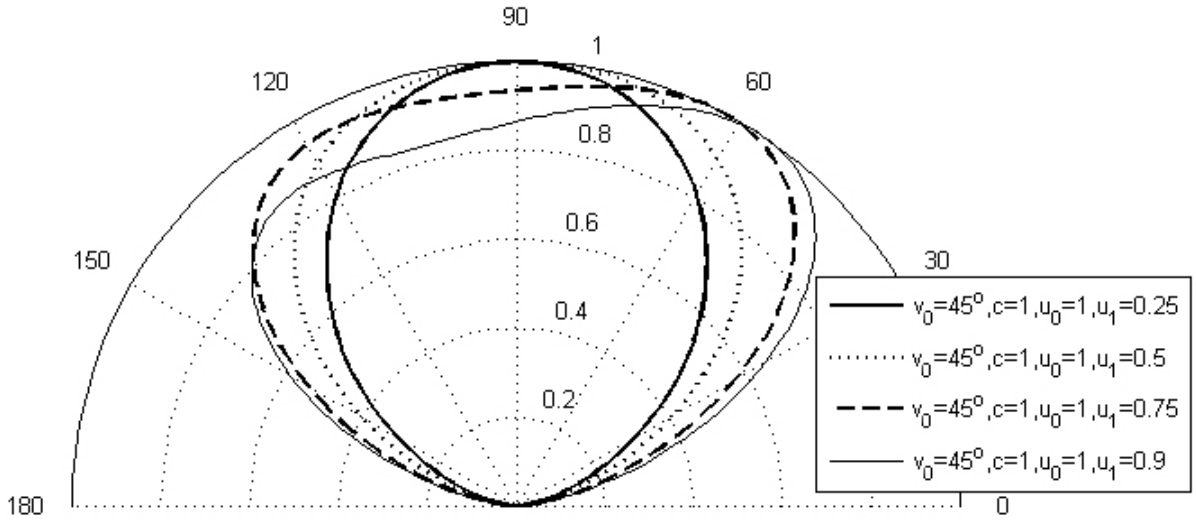

Figure 18. Far-field behavior, given by (Equation 5.14)for E-polarization with $v_0 = 45^o, u_0 = 1, u_1 = 0.25, 0.5, 1.0, 1.5$ and $c = 1$.

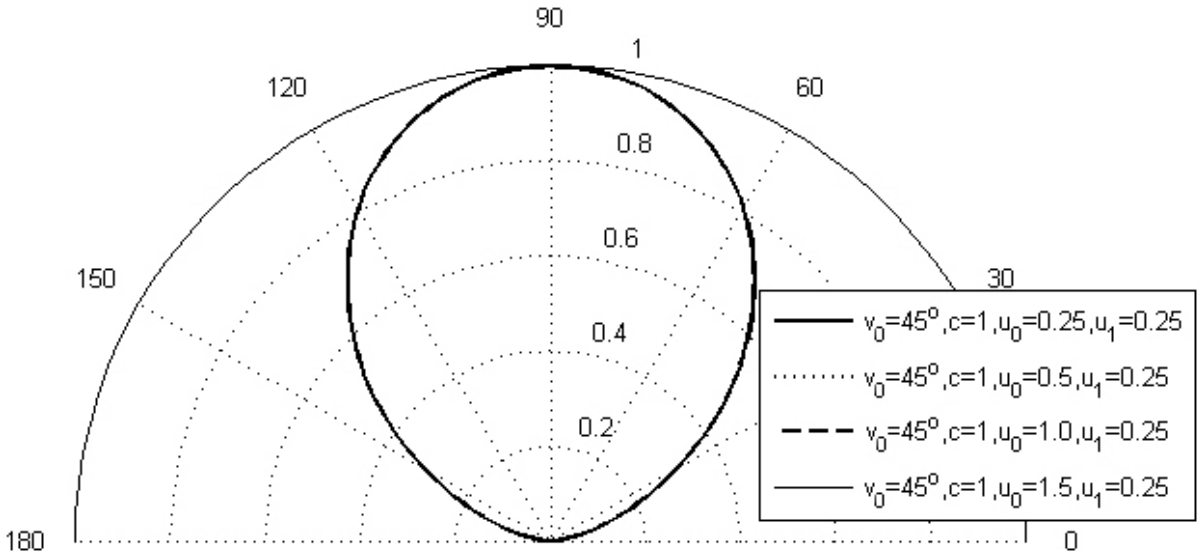

Figure 19. Far-field behavior, given by (Equation 5.14) for E-polarization with $v_0 = 45^o, u_0 = 0.25, 0.5, 1.0, 1.5, u_1 = 0.25$ and $c = 1$.

CHAPTER 6

ELECTROMAGNETIC RADIATION AND SCATTERING FOR A GAP IN A CORNER BACKED BY A CAVITY FILLED WITH DNG METAMATERIAL

6.1 INTRODUCTION

We consider the two-dimensional geometry of Figure 20 where a partially covered cavity is located at the corner of two metallic walls perpendicular to each other. The cavity has a cross section that is a quarter ellipse, and is slotted from the focus to the center of the ellipse. The cavity is partially covered by a thin metallic strip that extends from the focal line away from the central line of the ellipse, as part of the metallic wall under which the cavity is flush-mounted. The cavity is filled with a double-negative lossless metamaterial whose electric permittivity and magnetic permeability are real and opposite to the corresponding parameters of the quarter-space above the cavity. Causality requires that the index of refraction of the DNG material be negative and its intrinsic impedance positive.

Two types of sources are considered. One is a plane wave with arbitrary direction of incidence in the quarter space ($x > 0, y > 0$) and polarized with the electric or the magnetic field parallel to the z axis. The other one is an electric or magnetic line source parallel to the z axis. This two-dimensional boundary-value problem is solved exactly, in the frequency domain. In elliptic cylindrical coordinates, the primary and secondary field components are

expanded in infinite series of eigenfunctions that are products of radial and angular Mathieu functions, where the Stratton-Chu normalization is adopted (see e.g. (10; 19; 11)). Since the angular Mathieu functions are the same for positive and negative refractive index, it is possible to determine analytically the modal expansion coefficients of the secondary fields, by imposing the boundary conditions.

The only two-dimensional problem involving radiation and scattering by a cavity flush-mounted under a metallic plane for which an exact analytical solution exists is that of a slotted semielliptical channel (20; 21). A related geometry is the cavity-backed gap in a corner (22; 6). These geometries involve materials inside and outside the channel that are isorefractive to each other. Recently, the analysis performed in (20; 21) was extended to the case of a trench filled with DNG metamaterial (23; 24). The present work is an extension of the geometry analyzed in (22; 6) to the case of a corner cavity filled with DNG metamaterial and presented in (25).

Numerical results are shown for fields both inside and outside the cavity, for several cavity configurations and different primary sources.

6.2 GEOMETRY OF THE PROBLEM

A cross-sectional view of the structure in a plane $z =$ constant is shown in Figure 20. It is identical to that considered in (6), except for the material filling the trench.

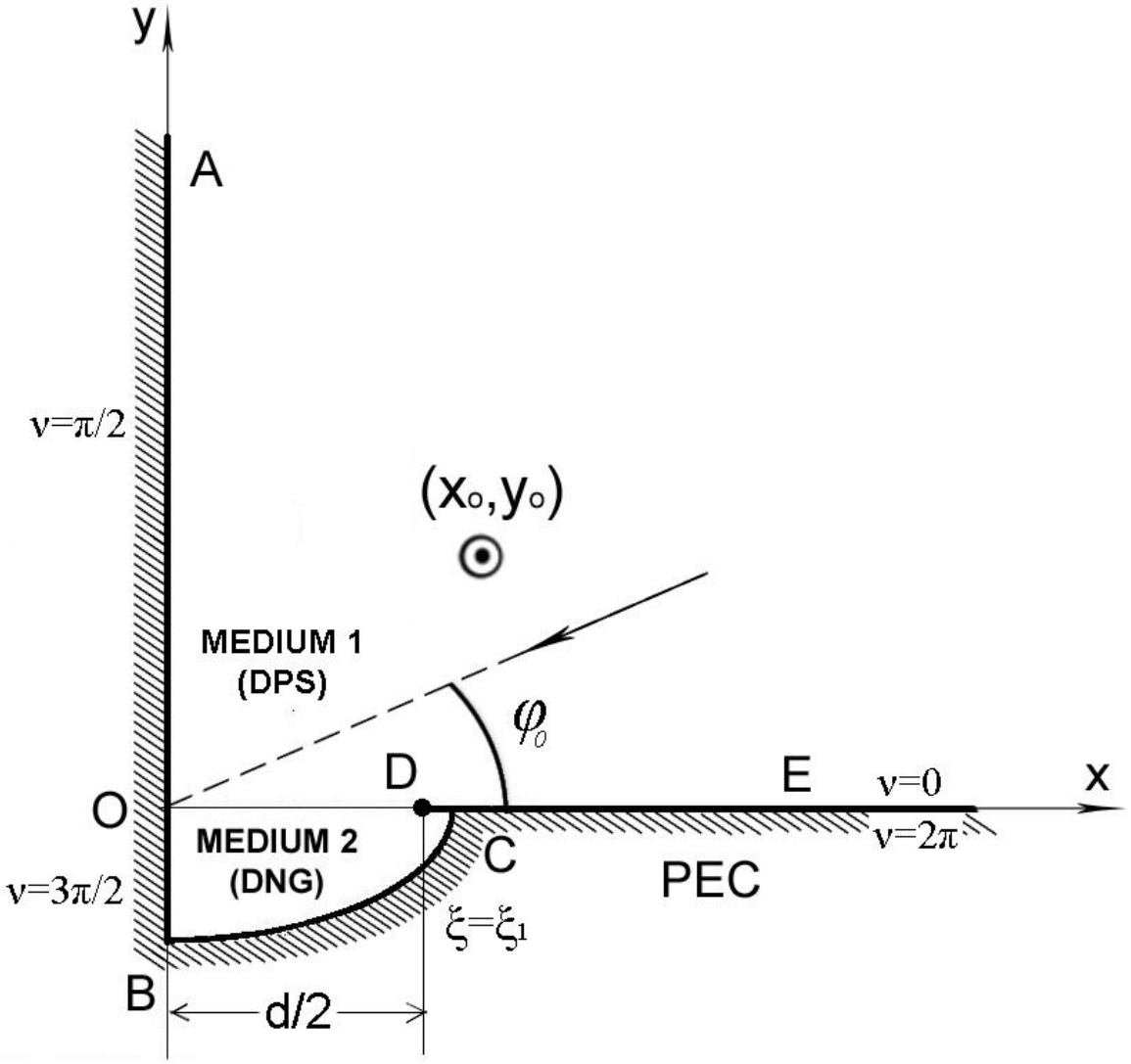

Figure 20. Geometry of the problem.

The metallic walls $OA(x = 0)$ and $OE(y = 0)$ are perpendicular to each other. The trench OBC is flush-mounted under the horizontal wall OE, and its cross-section is a quarter ellipse with semi-major axis OC and semi-minor axis OB. The wall OE is slotted along the slit of width OD equal to half the inter focal distance d of the elliptical trench. The trench is partially covered by the thin metal baffle DC.

Outside the cavity, the electric permittivity is ε and the magnetic permeability is μ, whereas inside the cavity the same quantities become $-\varepsilon$ and $-\mu$, respectively.

The wave vector is $k = \sqrt{\varepsilon\mu}$ outside the cavity and $-\sqrt{\varepsilon\mu}$ inside the cavity. We define a dimensionless parameter $c = kd/2$ in the material outside the cavity and $-c$ inside the cavity filled with DNG material. The intrinsic impedance $Z = \sqrt{\mu/\varepsilon}$ is the same inside and outside the cavity. The fact that in a DNG metamaterial the signs of the square roots must be chosen so that the refractive index is negative but the intrinsic impedance is positive is dictated by causality, not just by the radiation condition. The opposite choice, i.e. a positive refractive index and a negative intrinsic impedance, would therefore be physically incorrect (see (15)).

6.3 PLANE WAVE INCIDENCE

6.3.1 E-polarization

Consider a plane wave incident perpendicularly to the trench axis and polarized parallel to z-axis, with primary electric field

$$\boldsymbol{E}^i = \hat{z}E^i_{1z} = \hat{z}\exp[jk(x\cos\varphi_0 + y\sin\varphi_0)] \tag{6.1}$$

Incident field will be the same as in Equation 2.2

$$E_{1z}^{i} = \sqrt{8\pi} \sum_{m=0}^{\infty} j^m \left[\frac{1}{N_m^{(e)}} \mathrm{Re}_m^{(1)}(c,u)\mathrm{Se}_m(c,v)\mathrm{Se}_m(c,\varphi_0) + \frac{1}{N_m^{(o)}} \mathrm{Ro}_m^{(1)}(c,u)\mathrm{So}_m(c,v)\mathrm{So}_m(c,\varphi_0) \right]. \tag{6.2}$$

The total electric field in medium 1 can be written as the sum of a geometric-optics field E_{1z}^{go} due to the corner reflector without the trench and a diffracted field E_{1z}^{d} due to the presence of the trench

$$E_{1z} = E_{1z}^{go} + E_{1z}^{d}. \tag{6.3}$$

The geometric-optics field is the sum of four terms

$$E_{1z}^{go} = E_{1z}^{i} + E_{1z}^{OE} + E_{1z}^{OA} + E_{1z}^{OA,OE} \tag{6.4}$$

where, referring to Figure 21, the field E_{1z}^{OE} corresponds to a wave with incidence angle $2\pi - \varphi_0$ multiplied by a reflection coefficient -1, the field E_{1z}^{OA} corresponds to a wave with incidence angle $\pi - \varphi_0$ multiplied by a reflection coefficient -1, and the field $E_{1z}^{OA,OE}$ corresponds to a doubly reflected wave, i.e., a wave with incidence angle $\pi + \varphi_0$ and reflection coefficient 1.

When the even and odd functions of φ_0 are separated out in the various field components, it is found that the overall geometric-optics field is

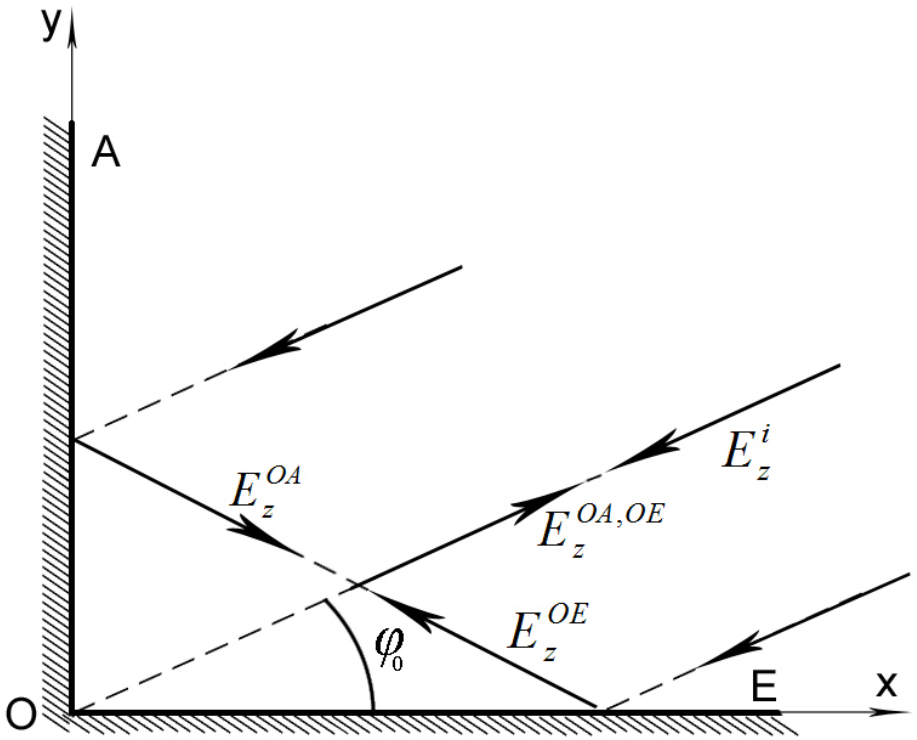

Figure 21. Geometric-optics contribution for plane-wave incidence.

$$E_{1z}^{go} = 8\sqrt{2\pi}\sum_{l=1}^{\infty}\frac{(-1)^l}{N_{2l}^{(o)}}\mathrm{Ro}_{2l}^{(1)}(c,u)\mathrm{So}_{2l}(c,v)\mathrm{So}_{2l}(c,\varphi_0). \tag{6.5}$$

The diffracted field can be written as

$$E_{1z}^{d} = 8\sqrt{2\pi}\sum_{l=1}^{\infty}\frac{(-1)^l}{N_{2l}^{(o)}}a_l\mathrm{Ro}_{2l}^{(4)}(c,u)\mathrm{So}_{2l}(c,v)\mathrm{So}_{2l}(c,\varphi_0). \tag{6.6}$$

The total electric field inside the trench is

$$E_{2z} = 8\sqrt{2\pi}\sum_{l=1}^{\infty}\frac{(-1)^l}{N_{2l}^{(o)}}b_l\left[\frac{\mathrm{Ro}_{2l}^{(4)}(-c,u_1)}{\mathrm{Ro}_{2l}^{(1)}(-c,u_1)}\mathrm{Ro}_{2l}^{(1)}(-c,u)-\mathrm{Ro}_{2l}^{(4)}(-c,u)\right]\mathrm{So}_{2l}(c,v)\mathrm{So}_{2l}(c,\varphi_0). \tag{6.7}$$

The modal coefficients can be found by applying the boundary conditions. The tangential component of the total electric and magnetic fields in both media are equal across $u = 0$

$$E_{1z}|_{u=0} = E_{2z}|_{u=0}\,,\; H_{1v}|_{u=0} = -\,H_{2v}|_{u=0}\,. \tag{6.8}$$

Therefore, applying the boundary conditions yields the modal coefficients a_l and b_l as

$$a_l = -\frac{\mathrm{Ro}_{2l}^{(4)}(-c,0)\mathrm{Ro}_{2l}^{(1)'}(c,0)}{\Delta_1}, \tag{6.9}$$

$$b_l = -\frac{\mathrm{Ro}_{2l}^{(1)'}(c,0)\mathrm{Ro}_{2l}^{(4)}(c,0)}{\Delta_1}, \tag{6.10}$$

where

$$\Delta_1 = \mathrm{Ro}_{2l}^{(4)}(-c,0)\mathrm{Ro}_{2l}^{(1)'}(-c,0)\frac{\mathrm{Ro}_{2l}^{(4)}(-c,u_1)}{\mathrm{Ro}_{2l}^{(1)}(-c,u_1)}+\mathrm{Ro}_{2l}^{(4)'}(c,0)\mathrm{Ro}_{2l}^{(4)}(-c,0)-\mathrm{Ro}_{2l}^{(4)}(c,0)\mathrm{Ro}_{2l}^{(4)'}(-c,0). \tag{6.11}$$

Detailed calculations of a_l and b_l are given in Appendix-D. Within the quarter space ($x > 0, y > 0$), the bistatic RCS $\sigma^{(e)}(\phi)$ is, in general, given by (see e.g. (11))

$$\sigma^{(e)}(\phi) = \lim_{\rho \to \infty} 2\pi\rho \frac{|\mathbf{E^s}|}{|\mathbf{E^i}|} \tag{6.12}$$

and in the case of this partially covered trench it becomes

$$\frac{\sigma^{(e)}(\phi)}{\lambda} = 128\pi \left| \sum_{l=1}^{\infty} \frac{a_l}{N_{2l}^{(o)}} \mathrm{So}_{2l}(c, v)\mathrm{So}_{2l}(c, \varphi_0) \right|^2 . \tag{6.13}$$

6.3.2 H-polarization

The analysis is similar to that for E-polarization, hence only the results are given. The incident magnetic field is

$$\boldsymbol{H}^i = \hat{z} H_{1z}^i, \tag{6.14}$$

$$H_{1z}^i = \exp[jk(x\cos\varphi_0 + y\sin\varphi_0)] =$$
$$\sqrt{8\pi} \sum_{m=0}^{\infty} \left[\frac{j^m}{N_m^{(e)}} \mathrm{Re}_m^{(1)}(c, u)\mathrm{Se}_m(c, v)\mathrm{Se}_m(c, \varphi_0) + \frac{j^m}{N_m^{(o)}} \mathrm{Ro}_m^{(1)}(c, u)\mathrm{So}_m(c, v)\mathrm{So}_m(c, \varphi_0) \right]. \tag{6.15}$$

The total magnetic field in medium-1 is

$$H_{1z} = H_{1z}^{go} + H_{1z}^{d}, \tag{6.16}$$

where the geometric-optics field H_{1z}^{go} is

$$H_{1z}^{go} = 8\sqrt{2\pi}\sum_{l=0}^{\infty}\frac{(-1)^l}{N_{2l}^{(e)}}\mathrm{Re}_{2l}^{(1)}(c,u)\mathrm{Se}_{2l}(c,v)\mathrm{Se}_{2l}(c,\varphi_0) \tag{6.17}$$

corresponding to the sum of four plane waves that are equivalent to those of Figure 21, provided that the electric field is replaced with a z directed magnetic field and all reflection coefficients are 1. Only the even Mathieu functions of even order appear because of the boundary conditions of the two metallic walls. The diffracted field due to the slotted trench is

$$H_{1z}^{d} = 8\sqrt{2\pi}\sum_{l=0}^{\infty}\frac{(-1)^l}{N_{2l}^{(e)}}c_l\mathrm{Re}_{2l}^{(4)}(c,u)\mathrm{Se}_{2l}(c,v)\mathrm{Se}_{2l}(c,\varphi_0). \tag{6.18}$$

the field inside the trench is

$$H_{2z} = 8\sqrt{2\pi}\sum_{l=0}^{\infty}\frac{(-1)^l}{N_{2l}^{(e)}}d_l\left[\frac{\mathrm{Re}_{2l}^{(4)'}(-c,u_1)}{\mathrm{Re}_{2l}^{(1)'}(-c,u_1)}\mathrm{Re}_{2l}^{(1)}(-c,u) - \mathrm{Re}_{2l}^{(4)}(-c,u)\right]\mathrm{Se}_{2l}(c,v)\mathrm{Se}_{2l}(c,\varphi_0) \tag{6.19}$$

where the prime means the derivative with respect to u. The boundary conditions are

$$H_{1z}|_{u=0} = H_{2z}|_{u=0}\,, \tag{6.20}$$

$$E_{1v}|_{u=0} = -\,E_{2v}|_{u=0}\,, \tag{6.21}$$

which yield the expansion coefficients

$$c_l = -\frac{\mathrm{Re}_{2l}^{(4)'}(-c,0)\mathrm{Re}_{2l}^{(1)}(c,0)}{\Delta_2}, \tag{6.22}$$

$$d_l = \frac{\mathrm{Re}_{2l}^{(4)'}(c,0)\mathrm{Re}_{2l}^{(1)}(c,0)}{\Delta_2}, \tag{6.23}$$

where

$$\Delta_2 = \mathrm{Re}_{2l}^{(4)}(c,0)\mathrm{Re}_{2l}^{(4)'}(-c,0) + \mathrm{Re}_{2l}^{(4)'}(c,0)\left[\frac{\mathrm{Re}_{2l}^{(4)'}(-c,u_1)}{\mathrm{Re}_{2l}^{(1)'}(-c,u_1)}\mathrm{Re}_{2l}^{(1)}(-c,0) - \mathrm{Re}_{2l}^{(4)}(-c,0)\right]. \tag{6.24}$$

The bistatic RCS $\sigma^{(h)}(\phi)$ of the partially covered trench is

$$\frac{\sigma^{(h)}(\phi)}{\lambda} = 128\pi\left|\sum_{l=1}^{\infty}\frac{c_l}{N_{2l}^{(e)}}\mathrm{Se}_{2l}(c,v)\mathrm{Se}_{2l}(c,\varphi_0)\right|^2. \tag{6.25}$$

6.4 LINE SOURCE INCIDENCE

6.4.1 E-polarization

Consider an electric line source parallel to the z-axis and located at $(x_0, y_0) \equiv (u_0, v_0)$ whose primary electric field is

$$\boldsymbol{E}^i = \hat{z}E_z^i = \hat{z}H_0^{(2)}(kR) \tag{6.26}$$

where

$$R = \sqrt{(x - x_0)^2 + (y - y_0)^2} \tag{6.27}$$

is the distance between the line source and the observation point $(x, y) \equiv (u, v)$. The incident field may be expanded in a series of elliptic-cylinder functions (11)

$$E_{1z}^i = H_0^{(2)}(kR) = 4 \sum_{m=0}^{\infty} \left[\frac{1}{N_m^{(e)}} \mathrm{Re}_m^{(1)}(c, u_<) \mathrm{Re}_m^{(4)}(c, u_>) \mathrm{Se}_m(c, v) \mathrm{Se}_m(c, v_0) \right.$$
$$\left. + \frac{1}{N_m^{(o)}} \mathrm{Ro}_m^{(1)}(c, u_<) \mathrm{Ro}_m^{(4)}(c, u_>) \mathrm{So}_m(c, v) \mathrm{So}_m(c, v_0) \right], \tag{6.28}$$

where $u_<$ ($u_>$) is the smaller (larger) between u and u_0.

In the quarter space ($x \geq 0, y \geq 0$) outside the trench, the total electric field E_{1z} may be written as the sum of the diffracted field and the geometrical-optics field. The geometrical-optics field E_{1z}^{go} is the total field that would be present in the absence of the trench and is the sum of the fields due to four line sources, i.e., the primary line source and its three images.

$$E_{1z}^{go} = H_0^{(2)}(kR) - H_0^{(2)}(kR_1) - H_0^{(2)}(kR_2) + H_0^{(2)}(kR_3) \tag{6.29}$$

where

$$R_1 = \sqrt{(x-x_0)^2+(y+y_0)^2}, \tag{6.30}$$

$$R_2 = \sqrt{(x+x_0)^2+(y-y_0)^2}, \tag{6.31}$$

$$R_3 = \sqrt{(x+x_0)^2+(y+y_0)^2}. \tag{6.32}$$

Referring to Figure 22, the image line S_1 is located at $(x_0, -y_0) \equiv (u_0, 2\pi - \varphi_0)$, the image line S_2 at $(-x_0, y_0) \equiv (u_0, \pi - \varphi_0)$, and the image line S_3 at $(-x_0, -y_0) \equiv (u_0, \pi + \varphi_0)$.

By expanding the Hankel functions in series of elliptic-cylinder functions and utilizing properties of the angular Mathieu functions, it can be found that

$$E_{1z}^{go} = 16 \sum_{l=0}^{\infty} \frac{1}{N_{2l}^{(o)}} \mathrm{Ro}_{2l}^{(1)}(c, u_<) \mathrm{Ro}_{2l}^{(4)}(c, u_>) \mathrm{So}_{2l}(c, v) \mathrm{So}_{2l}(c, v_0), \tag{6.33}$$

which involves only odd Mathieu functions of even order. The diffracted field E_{1z}^d due to the presence of the trench in $(x \geq 0, y \geq 0)$ and the total field inside the trench are given by, on consideration of the boundary conditions

$$E_{1z}^d = 16 \sum_{l=1}^{\infty} \frac{e_l}{N_{2l}^{(o)}} \mathrm{Ro}_{2l}^{(4)}(c, u_0) \mathrm{Ro}_{2l}^{(4)}(c, u) \mathrm{So}_{2l}(c, v) \mathrm{So}_{2l}(c, v_0) \tag{6.34}$$

$$E_{2z} = 16 \sum_{l=1}^{\infty} \frac{f_l}{N_{2l}^{(o)}} \mathrm{Ro}_{2l}^{(4)}(-c, u_0) \left[\frac{\mathrm{Ro}_{2l}^{(4)}(-c, u_1)}{\mathrm{Ro}_{2l}^{(1)}(-c, u_1)} \mathrm{Ro}_{2l}^{(1)}(-c, u) - \mathrm{Ro}_{2l}^{(4)}(-c, u) \right]. \tag{6.35}$$

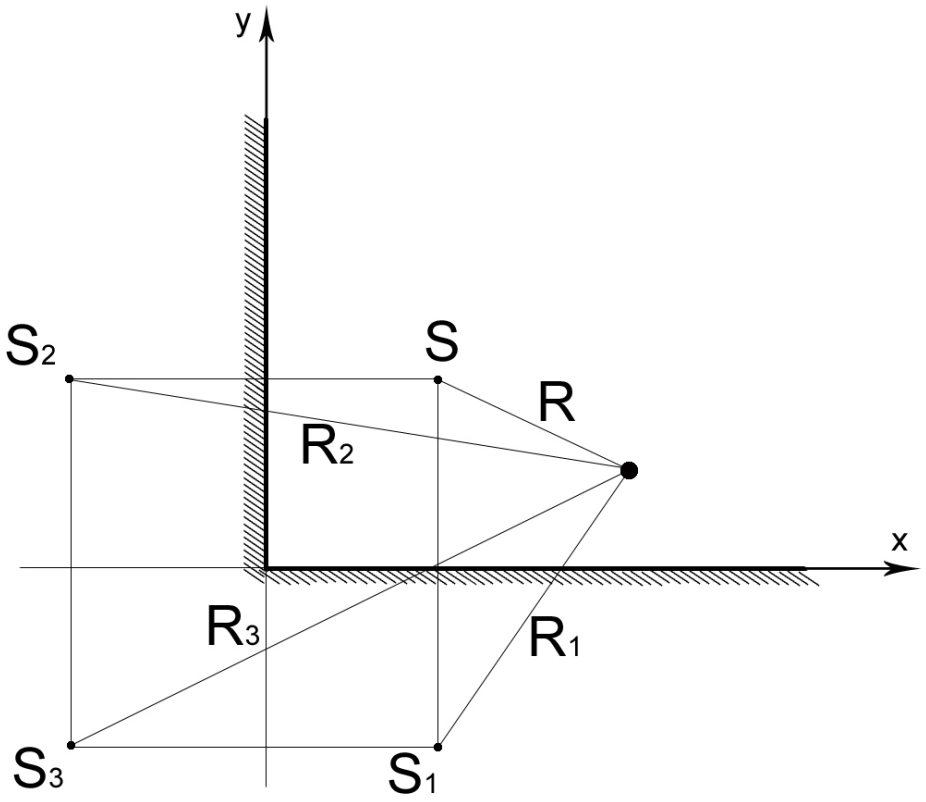

Figure 22. Geometric-optics contribution for line-source excitation.

The magnetic field is still related to the electric field by (Equation 1.4). The unknown modal coefficients e_l and f_l are determined by imposing the continuity of the total tangential electric and magnetic fields across the interface $\xi = 1$ or $u = 0$, yielding

$$e_l = -\mathrm{Ro}_{2l}^{(4)}(-c, u_0)\mathrm{Ro}_{2l}^{(4)}(-c, o)\mathrm{Ro}_{2l}^{(1)'}(c, 0)\frac{\mathrm{Ro}_{2l}^{(4)}(c, u_0)}{\Delta_3}, \tag{6.36}$$

$$f_l = -\frac{\mathrm{Ro}_{2l}^{(1)'}(c, 0)\mathrm{Ro}_{2l}^{(4)}(c, u_0)\mathrm{Ro}_{2l}^{(4)}(c, 0)\mathrm{Ro}_{2l}^{(4)}(c, u_0)}{\Delta_3}, \tag{6.37}$$

where

$$\Delta_3 = \mathrm{Ro}_{2l}^{(4)}(c,u_0)\mathrm{Ro}_{2l}^{(4)}(-c,u_0)\left[\mathrm{Ro}_{2l}^{(4)}(c,0)\left(\frac{\mathrm{Ro}_{2l}^{(4)}(-c,u_1)}{\mathrm{Ro}_{2l}^{(1)}(-c,u_1)}\mathrm{Ro}_{2l}^{(1)'}(-c,0)-\mathrm{Ro}_{2l}^{(4)'}(-c,0)\right)+\right.$$
$$\left.\mathrm{Ro}_{2l}^{(4)}(-c,0)\mathrm{Ro}_{2l}^{(4)'}(c,0)\right]. \tag{6.38}$$

The behavior of the field scattered by the DNG cavity may be examined at large distance by considering

$$E_{1z}^{d}|_{u\to\infty,Im(c)<0} \approx \frac{e^{-jk\rho+j\pi/4}}{\sqrt{k\rho}}P^{(e)}(\phi;u_0,v_0), \tag{6.39}$$

where

$$P^{(e)}(\phi;u_0,v_0) = 16\sum_{l=1}^{\infty}\frac{(-1)^l}{N_{2l}^{(o)}}e_l\mathrm{Ro}_{2l}^{(4)}(c,u_0)\mathrm{So}_{2l}(c,v)\mathrm{So}_{2l}(c,v_0) \tag{6.40}$$

is a far-field coefficient that depends not only on the angle of observation ϕ but also on the source location (u_0,v_0). In the derivation of (Equation 6.40), $\mathrm{Ro}_{2l}^{(4)}(c,u)$ in (Equation 6.34) was evaluated with an asymptotic expansion for the Mathieu radial function.

6.4.2 H-polarization

The derivations are similar to those for E-polarization, hence only the results are given. For a magnetic line source parallel to the z-axis and located outside the trench at $(x_0, y_0) \equiv (u_0, v_0) \equiv (\xi_0, \eta_0)$ the primary magnetic field is

$$\boldsymbol{H}^i = \hat{z} H_z^i = \hat{z} H_0^{(2)}(kR). \tag{6.41}$$

Once again, the total magnetic field in medium-1, H_{1z}, may be written as the sum of diffracted field and the geometrical-optics field. The geometrical-optics field H_{1z}^{go} is the total field that would be present in the absence of the trench and is the sum of the fields due to four line sources, i.e., the primary line source and its three images.

$$H_{1z}^{go} = H_0^{(2)}(kR) - H_0^{(2)}(kR_1) - H_0^{(2)}(kR_2) + H_0^{(2)}(kR_3) \tag{6.42}$$

$$H_{1z}^{go} = 16 \sum_{l=0}^{\infty} \frac{l}{N_{2l}^{(e)}} \mathrm{Re}_{2l}^{(1)}(c, u_<) \mathrm{Re}_{2l}^{(4)}(c, u_>) \mathrm{Se}_{2l}(c, v) \mathrm{Se}_{2l}(c, v_0). \tag{6.43}$$

The diffracted field H_{1z}^d due to the presence of the trench in $(x \geq 0, y \geq 0)$ and the total field inside the trench are given by

$$H_{1z}^d = 16 \sum_{l=0}^{\infty} \frac{g_l}{N_{2l}^{(e)}} \mathrm{Re}_{2l}^{(4)}(c, u_0) \mathrm{Re}_{2l}^{(4)}(c, u) \mathrm{Se}_{2l}(c, v) \mathrm{Se}_{2l}(c, v_0), \tag{6.44}$$

$$H_{2z} = 16 \sum_{l=0}^{\infty} \frac{h_l}{N_{2l}^{(e)}} \mathrm{Re}_{2l}^{(4)}(-c, u_0) \left[\frac{\mathrm{Re}_{2l}^{(4)'}(-c, u_1)}{\mathrm{Re}_{2l}^{(1)'}(-c, u_1)} \mathrm{Re}_{2l}^{(1)}(-c, u) - \mathrm{Re}_{2l}^{(4)}(-c, u) \right] \times \mathrm{Se}_{2l}(-c, v) \mathrm{Se}_{2l}(-c, v_0). \tag{6.45}$$

The electric field is related to the magnetic field by (Equation 1.5). The unknown modal coefficients g_l and h_l are determined by applying the boundary condition across $u = 0$, yielding

$$g_l = - \mathrm{Re}_{2l}^{(1)}(c, 0) \mathrm{Re}_{2l}^{(4)}(c, u_0) \mathrm{Re}_{2l}^{(4)}(-c, u_0) \frac{\mathrm{Re}_{2l}^{(4)'}(-c, 0)}{\Delta_4}, \tag{6.46}$$

$$h_l = \frac{\mathrm{Re}_{2l}^{(4)'}(c, 0) \mathrm{Re}_{2l}^{(4)}(c, u_0) \mathrm{Re}_{2l}^{(1)}(c, 0) \mathrm{Re}_{2l}^{(4)}(c, u_0)}{\Delta_4}, \tag{6.47}$$

where

$$\Delta_4 = \mathrm{Re}_{2l}^{(4)}(c, u_0) \mathrm{Re}_{2l}^{(4)}(-c, u_0) \left[\mathrm{Re}_{2l}^{(4)'}(c, 0) \left(\frac{\mathrm{Re}_{2l}^{(4)'}(-c, u_1)}{\mathrm{Re}_{2l}^{(1)'}(-c, u_1)} \mathrm{Re}_{2l}^{(1)}(-c, 0) - \mathrm{Re}_{2l}^{(4)}(-c, 0) \right) + \mathrm{Re}_{2l}^{(4)}(c, 0) \mathrm{Re}_{2l}^{(4)'}(-c, 0) \right]. \tag{6.48}$$

Similarly, the behavior of the field scattered magnetic field by the DNG cavity may be examined at large distance by considering

$$H_{1z}^{d}|_{u\to\infty,Im(c)<0} \approx \frac{e^{-jk\rho+j\pi/4}}{\sqrt{k\rho}} P^{(h)}(\phi; u_0, v_0), \tag{6.49}$$

where

$$P^{(h)}(\phi; u_0, v_0) = 16 \sum_{l=1}^{\infty} \frac{(-1)^l}{N_{2l}^{(e)}} g_l \mathrm{Re}_{2l}^{(4)}(c, u_0) \mathrm{Se}_{2l}(c, v) \mathrm{Se}_{2l}(c, v_0) \tag{6.50}$$

is a far-field coefficients that depends not only on the angle of observation ϕ but also on the source location (u_0, v_0).

6.5 NUMERICAL RESULTS

The evaluation of Mathieu functions was accomplished using the Fortran code described in (17). The numerical results described in this section were obtained after summing the first 20 terms of the pertinent series and using the acceleration method described in (18).

6.5.1 Plane Wave Incidence

The scattering effect of trench can be investigated easily by looking at the normalized bistatic RCS as given by (Equation 6.13) and (Equation 6.25). The value of c is controlled by the frequency and the focal distance d through

$$c = \frac{kd}{2} = \frac{\pi d}{\lambda}. \tag{6.51}$$

What is important is the relative value of parameters inside and outside the trench, not their absolute value. Since the medium outside the trench is of infinite extent, it may be safely assumed to be free space; however, this restriction is not necessary for the validity of our calculations. The effect of the variation of c is examined in Figure 23, where an E-polarized plane wave is incident at an angle $\varphi_0 = \pi/4$. Three cases were examined: $c = 1$, $c = 2$, and $c = 3$. When $c = 1$ the RCS is so much smaller than for the other two cases that it simply appears as a point at the origin of the polar diagram. The observed behavior of higher RCS values when c is increased agrees with what is expected from scattering theory. Figure 24 shows the effect of the variable c values with an H-polarized plane wave with same incident angle.

6.5.2 Line Source Incidence

The scattering effect of trench can be easily investigated by looking at the square magnitude of the far-field coefficient (Equation 6.40)

$$\psi^{(e)}(\phi; u_0, v_0) = \left| P^{(e)}(\phi; u_0, v_0) \right|^2 . \tag{6.52}$$

Figure 25 shows the far-field behavior for different locations of the electric line source along the ellipse $u = 1$, for a corner gap with $c = 2$ and $u_1 = 0.5$. One observes that as the source moves from close to the wall at $y = 0$ ($v_0 = 5\pi/180$) to the bisectrix of the xy plane the intensity of the pattern increases, while the shape of the beam is the same.

Similarly, the scattering effect of a magnetic line source may be investigated by looking at the square magnitude of the far-field coefficient

$$\psi^{(h)}(\phi; u_0, v_0) = \left| P^{(h)}(\phi; u_0, v_0) \right|^2 . \tag{6.53}$$

The scattering effect of a magnetic line source can be examined by looking at Figure 26

6.6 CONCLUSION

An exact solution to the boundary-value problem of a trench of quarter-elliptical cross section filled with DNG metamaterial, slotted along its inter focal strip and flush-mounted in the corner of two metallic walls perpendicular to each other has been obtained by separation of variables in the frequency domain, for both plane wave and line source excitations. Numerical results have been shown for the far-field coefficient.

Our result enriches the catalog of canonical solutions for two-dimensional boundary-value problems, and may be useful in validating computer codes that have been developed for complex geometries and penetrable media.

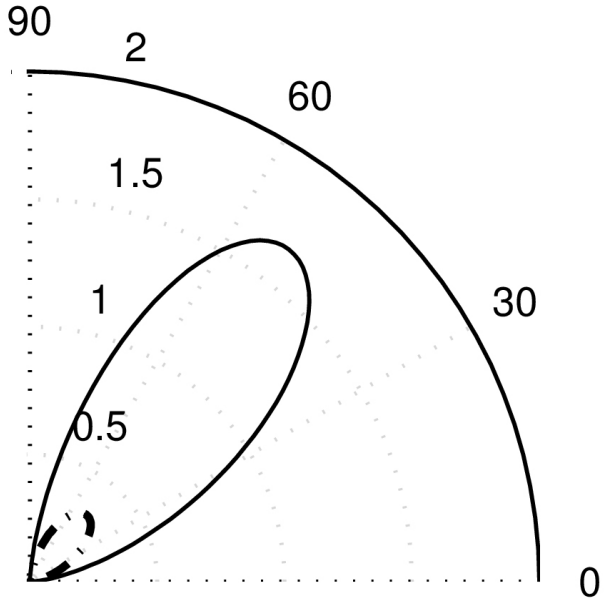

Figure 23. Polar plot of the normalized bistatic RCS $\sigma^{(e)}(\phi)$ given by (Equation 6.13) on a linear scale for an E-polarized plane wave is incident at an angle $\phi_0 = \pi/4$. Dash-dot line: $c = 2$, and solid line: $c = 3$. The values for $c = 1$ are so much smaller that corresponds to the origin in the scale used for this figure.

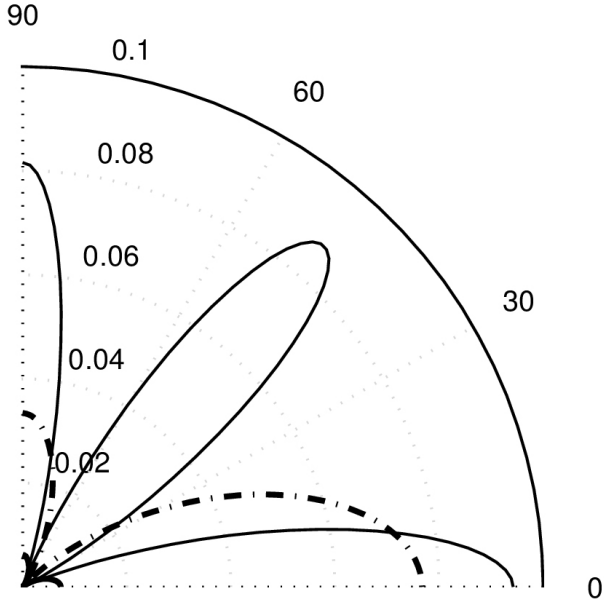

Figure 24. Polar plot of the normalized bistatic RCS $\sigma^{(h)}(\phi)$ given by (Equation 6.25) on a linear scale for an H-polarized plane wave is incident at an angle $\phi_0 = \pi/4$. Thick solid line: $c = 1$, dash-dot line: $c = 2$, and thin solid line: $c = 3$.

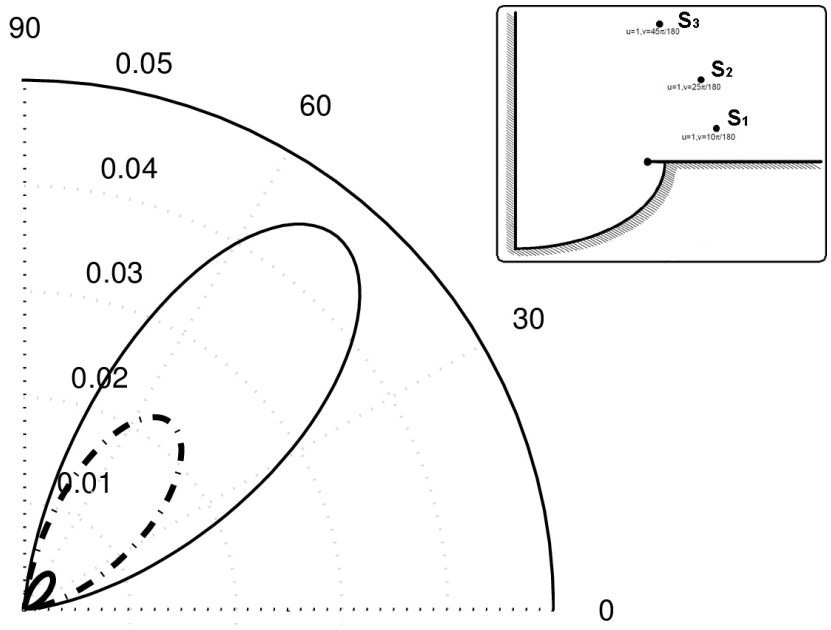

Figure 25. Polar plot of the far-field coefficient $\psi^{(e)}(\phi; u_0, v_0)$ given by (Equation 6.52) using a linear scale. The results represent a line source at S_1 (thick solid line); S_2 (dash-dot line); and S_3 (thin solid line). In all three cases $c = 2$. Units are $(\mathrm{V/m})^2$.

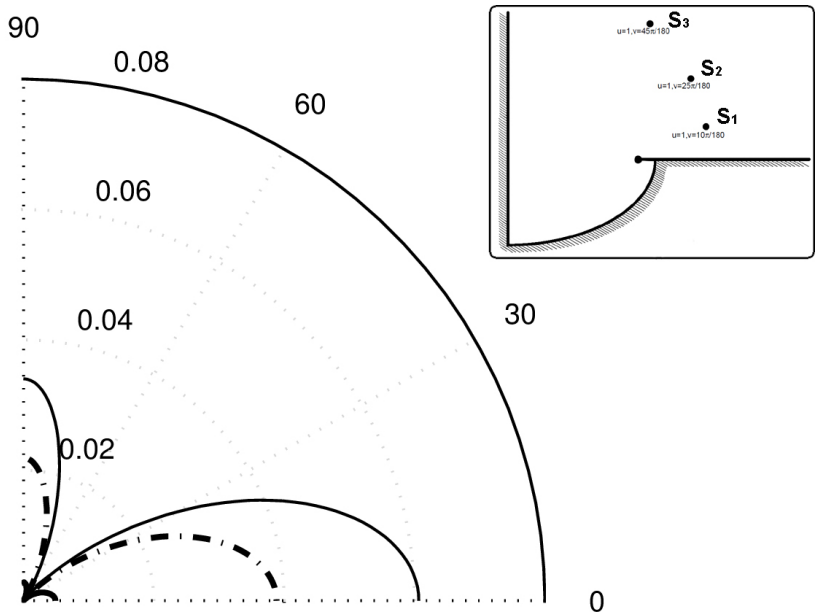

Figure 26. Polar plot of the far-field coefficient $\psi^{(h)}(\phi; u_0, v_0)$ given by (Equation 6.53) using a linear scale. The results represent a line source at S_1 (thin solid line); S_2 (dash-dot line); S_3 (thick dash line). In all three cases $c = 2$. Units are $(\mathrm{V/m})^2$.

CHAPTER 7

RADIATION BY A LINE SOURCE SHIELDED BY A CONFOCAL ELLIPTIC LAYER OF DNG METAMATERIAL

7.1 Introduction

A confocal elliptic cylindrical layer made of double-negative (DNG) metamaterial is considered. The space inside and outside the layer is filled with a lossless homogeneous double-positive (DPS) medium characterized by a real positive electric permittivity ϵ_1 and a real positive magnetic permeability μ_1, whereas the DNG sheath is characterized by a real negative permittivity $-\epsilon_2$ and a real negative permeability $-\mu_2$. The isorefractive condition $\epsilon_1\mu_1 = \epsilon_2\mu_2$ is assumed. Consequently, the wavenumber is

$$k_\ell = -(-1)^\ell \omega\sqrt{\epsilon_\ell \mu_\ell}, \tag{7.1}$$

where ω is the angular frequency, and $\ell = 1$ in the DPS regions of space and $\ell = 2$ inside the DNG sheath, meaning that the real positive wavenumber in the DPS regions has the same magnitude but opposite sign to the real negative wavenumber in the DNG layer. The real positive intrinsic impedances are

$$Z_\ell = \sqrt{\frac{\mu_\ell}{\epsilon_\ell}}. \tag{7.2}$$

The primary field is an electric or magnetic line source parallel to the generators of the cylindrical sheath and located anywhere inside the DPS medium encased by the sheath. The analysis is conducted in phaser domain with the time-dependence factor $\exp(+j\omega t)$ omitted throughout. In all regions, the field components are expressed as infinite series of Mathieu functions whose modal expansion coefficients are found analytically by imposing the boundary conditions.

This novel analytical solution is evaluated numerically for different values of the parameters involved: dimensions and thickness of the sheath in terms of wavelength, eccentricity of the elliptical cross-section of the sheath, ratio of the intrinsic impedances of the DPS and DNG media, location of the line source. Particular attention is devoted to the radiated far field and to the field inside the DNG layer.

A simplified solution is obtained when the intrinsic impedances of the DPS and DNG media are equal and the source is located in the plane containing the focal lines of the elliptical sheath. In particular, a comparison with a geometrical-optics solution is performed when the source coincides with a focal line; this simplified solution was presented at a conference (26) and it has been published in AWPL (27). Previous works have examined the case of an elliptic cylinder completely filled with DNG metamaterial and excited by a line source located at a focal line, both from an optical (12) and an electromagnetic (28) viewpoint.

7.2 Geometry of the problem

A cross-section of the structure is shown in Figure 27. The generators of the elliptic-cylindrical sheath are parallel to the z-axis, and the elliptic cylinder coordinates (u, v, z) are related to the rectangular coordinates (x, y, z) by $x = d/2 \cosh u \cos v$, $y = d/2 \sinh u \sin v$,

$z = z$, where $0 \leq u < \infty$, $0 \leq v \leq 2\pi$, $-\infty < z < \infty$ and d is the inter focal distance between the focal lines F_1 and F_2. The dimensionless parameters

$$c = k_1 d/2 = \pi d/\lambda, \qquad \zeta = Z_1/Z_2, \tag{7.3}$$

where λ is the wavelength, are introduced. The inner and outer surfaces of the DNG sheath correspond to $u = u_1$ and $u = u_2$, respectively. The position of the line source is indicated by S in Figure 27. Because of symmetries, we may restrict the location of the first quadrant, corresponding to coordinates u_0 and v_0 such that $0 \leq u_0 \leq u_1, 0 \leq v_0 \leq \pi/2$.

7.3 Analytical Solution

Consider an isotropic electric line source with electric field

$$\boldsymbol{E}^i = \hat{z} E^i_{1z} = \hat{z} H^{(2)}_0(kR) \tag{7.4}$$

where $H^{(2)}_0$ is the Hankel function of the second kind and R is the distance of the observation point from the line source. This field may be expanded in an infinite series of products of radial and angular Mathieu functions (11):

$$\begin{aligned} E^i_{1z} =& 4 \sum_{m=0}^{\infty} \left[\frac{1}{N^{(e)}_m} \mathrm{Re}^{(1)}_m(c, u_<) \mathrm{Re}^{(4)}_m(c, u_>) \mathrm{Se}_m(c, v_0) \mathrm{Se}_m(c, v) + \right. \\ & \left. \frac{1}{N^{(o)}_m} \mathrm{Ro}^{(1)}_m(c, u_<) \mathrm{Ro}^{(4)}_m(c, u_>) \mathrm{So}_m(c, v_0) \mathrm{So}_m(c, v) \right], (u_<, u_>) \leq u_1) \end{aligned} \tag{7.5}$$

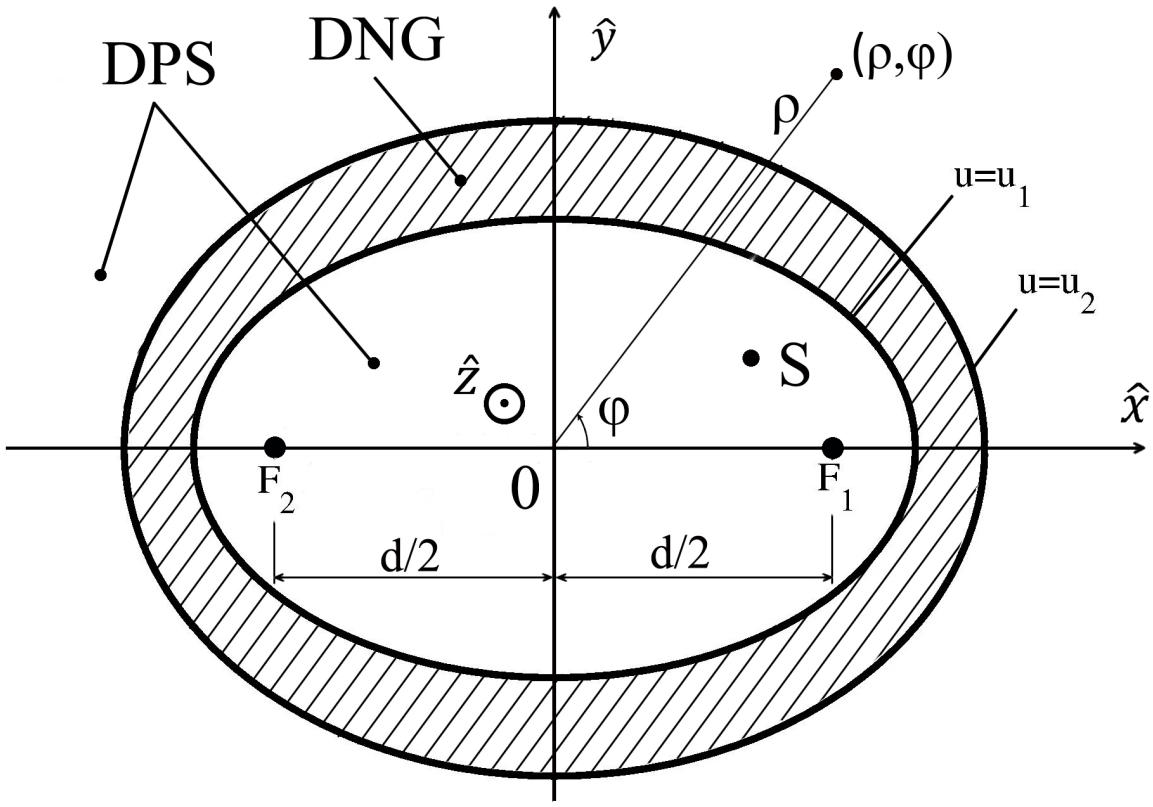

Figure 27. Cross-section of the structure

where $ui_<(u_>)$ is the smaller (larger) between u and u_0. The total electric field in the DPS region enclosed by the DNG sheath is

$$E_{1z} = E^i_{1z} + E^d_{1z}, \tag{7.6}$$

where

$$E_{1z}^{d} = 4\sum_{m=0}^{\infty}\left[\frac{a_m^{(e)}}{N_m^{(e)}}\mathrm{Re}_m^{(1)}(c,u_0)\mathrm{Re}_m^{(1)}(c,u)\mathrm{Se}_m(c,v_0)\mathrm{Se}_m(c,v)+ \frac{a_m^{(o)}}{N_m^{(o)}}\mathrm{Ro}_m^{(1)}(c,u_0)\mathrm{Ro}_m^{(1)}(c,u)\mathrm{So}_m(c,v_0)\mathrm{So}_m(c,v)\right], (u \le u_1). \tag{7.7}$$

The electric field radiated into the infinite DPS space surrounding the structure is

$$E_{1z}^{s} = 4\sum_{m=0}^{\infty}\left[\frac{c_m^{(e)}}{N_m^{(e)}}\mathrm{Re}_m^{(1)}(c,u_0)\mathrm{Re}_m^{(4)}(c,u)\mathrm{Se}_m(c,v_0)\mathrm{Se}_m(c,v)+ \frac{c_m^{(o)}}{N_m^{(o)}}\mathrm{Ro}_m^{(1)}(c,u_0)\mathrm{Ro}_m^{(4)}(c,u)\mathrm{So}_m(c,v_0)\mathrm{So}_m(c,v)\right], (u \ge u_2). \tag{7.8}$$

The electric field inside the DNG layer is

$$E_{2z} = 4\sum_{m=0}^{\infty}\left[\frac{\mathrm{Re}_m^{(1)}(c,u_0)}{N_m^{(e)}}\left[b_m^{(e)}\mathrm{Re}_m^{(1)}(-c,u)+d_m^{(e)}\mathrm{Re}_m^{(4)}(-c,u)\right]\mathrm{Se}_m(c,v_0)\mathrm{Se}_m(c,v) + \frac{\mathrm{Ro}_m^{(1)}(c,u_0)}{N_m^{(o)}}\left[b_m^{(o)}\mathrm{Ro}_m^{(1)}(-c,u)+d_m^{(o)}\mathrm{Ro}_m^{(4)}(-c,u)\right]\mathrm{Se}_m(c,v_0)\mathrm{Se}_m(c,v)\right], (u_1 \le u \le u_2) \tag{7.9}$$

where the fact that the angular functions Se_m and So_m are even functions of the parameter c has been taken into account.

The modal expansion coefficients $a_m^{(e,o)}$, $b_m^{(e,o)}$, $d_m^{(e,o)}$ and $c_m^{(e,o)}$ are determined by imposing the boundary conditions, i.e. the continuity of the tangential field components E_z and H_v across the interfaces $u = u_1$ and $u = u_2$. The magnetic field component H_v is related to E_z by

$$H_{lv} = \frac{(-1)^l j}{cZ_l} \frac{1}{\sqrt{\cosh^2 u - \cos^2 v}} E'_{lz}, \tag{7.10}$$

where $l = 1(2)$ for DPS (DNG) media, and here and in the following the prime means derivative with respect to u. It is found that

$$a_m^{(e)} = \frac{1}{\Delta^{(e)}} \left[A_m^{(e)}(u_1) B_m^{(e)}(u_2) - A_m^{(e)}(u_2) B_m^{(e)}(u_1) \right], \tag{7.11}$$

$$b_m^{(e)} = \frac{-j B_m^{(e)}(u_2)}{\Delta^{(e)}}, \tag{7.12}$$

$$c_m^{(e)} = \frac{-\zeta}{\Delta^{(e)}}, \tag{7.13}$$

$$d_m^{(e)} = \frac{j A_m^{(e)}(u_2)}{\Delta^{(e)}}, \tag{7.14}$$

where

$$A_m^{(e)}(u) = \mathrm{Re}_m^{(1)}(-c, u)\mathrm{Re}_m^{(4)\prime}(c, u) + \zeta \mathrm{Re}_m^{(1)\prime}(-c, u)\mathrm{Re}_m^{(4)}(c, u), \tag{7.15}$$

$$B_m^{(e)}(u) = \mathrm{Re}_m^{(1)}(-c, u)\mathrm{Re}_m^{(4)\prime}(c, u) + \zeta \mathrm{Re}_m^{(4)\prime}(-c, u)\mathrm{Re}_m^{(4)}(c, u), \tag{7.16}$$

$$\Delta^{(e)} = A_m^{(e)}(\xi_2)\left[\mathrm{Re}_m^{(1)'}(c,u_1)\mathrm{Re}_m^{(4)}(-c,u_1) + \xi\mathrm{Re}_m^{(1)}(c,u_1)\mathrm{Re}_m^{(4)'}(-c,u_1)\right] - B_m^{(e)}(\xi_2)\left[\mathrm{Re}_m^{(1)'}(c,u_1)\mathrm{Re}_m^{(1)}(-c,u_1) + \xi\mathrm{Re}_m^{(1)}(c,u_1)\mathrm{Re}_m^{(1)'}(-c,u_1)\right]. \quad (7.17)$$

The coefficients $a_m^{(o)}$, $b_m^{(o)}$, $d_m^{(o)}$ and $c_m^{(o)}$ are obtained by replacing $\mathrm{Re}_m^{(1,4)}$ and their derivatives with $\mathrm{Ro}_m^{(1,4)}$ and their derivatives everywhere in the expressions for $a_m^{(o)}$, $b_m^{(o)}$, $d_m^{(o)}$ and $c_m^{(o)}$ respectively.

In the absence of a DNG sheath, it is easily verified that

$$a_m^{(e,o)}|_{\xi_1=\xi_2} = 0, \quad (7.18)$$

$$c_m^{(e,o)}|_{\xi_1=\xi_2} = 1 \quad (7.19)$$

as should be expected. With reference to circular cylindrical coordinates (ρ,ϕ,z) (see Fig.1), the radiated far field is

$$E_{1z}^s|_{k\rho\to\infty} \approx P^{(e)}(\varphi)\frac{e^{-jk\rho+j\frac{\pi}{4}}}{\sqrt{k\rho}}, \quad (7.20)$$

where the far-field coefficient is

$$P^{(e)}(\varphi) = 4\sum_{m=0}^{\infty} j^m \left[\frac{c_m^{(e)}}{N_m^{(e)}}\mathrm{Re}_m^{(1)}(c,u_0)\mathrm{Se}_m(c,v_0)\mathrm{Se}_m(c,\varphi) + \frac{c_m^{(o)}}{N_m^{(o)}}\mathrm{Ro}_m^{(1)}(c,u_0)\mathrm{So}_m(c,v_0)\mathrm{So}_m(c,\varphi)\right]. \quad (7.21)$$

In the absence of the DNG sheath, the far-field coefficient is that of the line source (6), and is equal to one. Hence, the far-field power pattern normalized to the power pattern without the DNG sheath is

$$P(\varphi) = \left| P^{(e)}(\varphi) \right|^2 . \tag{7.22}$$

Simplifications in the formulas of this section occur when the line source is located either in the $x = 0$ plane or in the $y = 0$ plane of Fig.1. In particular, if the source coincides with the focal line F_1 of Fig.1, so that $u_0 = v_0 = 0$, the far-field coefficient (Equation 7.21) simplifies to

$$P^{(e)}(\varphi)|_{u_0=v_0=0} = 4 \sum_{m=0}^{\infty} \frac{j^m}{N_m^{(e)}} c_m^{(e)} \mathrm{Re}_m^{(1)}(c, 1) \mathrm{Se}_m(c, \varphi). \tag{7.23}$$

The solution for an isotropic magnetic line source is obtained by duality from the solution for an electric line source.

7.4 A Geometrical Optics Solution

Consider the particular case of an isotropic line source located at the focal line F_1. With reference to the cross-section of Figure 28, the optical ray F_1A is totally transmitted across the interface $u = u_1$ in the direction AB, as though it were produced by an anisotropic virtual line source located at the other focal line F_2. Along AB, the normalized power emitted per unit angle is (12)

$$p(\beta) = \frac{1 - \chi_1^2}{1 + \chi_1^2 - 2\chi_1 \cos\beta}, \tag{7.24}$$

where β is the angle that the direction F_2AB of propagation forms with the positive x-axis. The eccentricity of the cross-sectional ellipse $u = u_\ell$ is

$$\chi_\ell = \frac{d}{2a_\ell}, (\ell = 1, 2) \tag{7.25}$$

where a_ℓ is the semi-major axis of the ellipse.

The optical ray AB is totally transmitted across the interface $u = u_2$ in the direction F_1BC. If the virtual line source at F_2 were isotropic, the normalized power emitted per unit angle in the direction BC would be

$$p_{\text{iso}} = \frac{1 - \chi_2^2}{1 + \chi_2^2 + 2\chi_2 \cos\alpha}, \tag{7.26}$$

where α is the angle that the direction F_1BC forms with the positive x-axis. Therefore, the optical power emitted per unit angle along BC, normalized to the power emitted isotropically per unit angle by the line source at F_1, is

$$p(\alpha) = p_{\text{iso}}(\alpha)p(\beta) = \frac{(1 - \chi_1^2)(1 - \chi_2^2)}{(1 + \chi_1^2 - 2\chi_1 \cos\beta)(1 + \chi_2^2 + 2\chi_2 \cos\alpha)}. \tag{7.27}$$

To complete the optical solution, it remains to express β as a function of α. After some geometrical manipulations, it is found that

$$\cos\beta = \frac{(1 + \chi_2^2)\cos\alpha + 2\chi_2}{1 + \chi_2^2 + 2\chi_2 \cos\alpha)}. \tag{7.28}$$

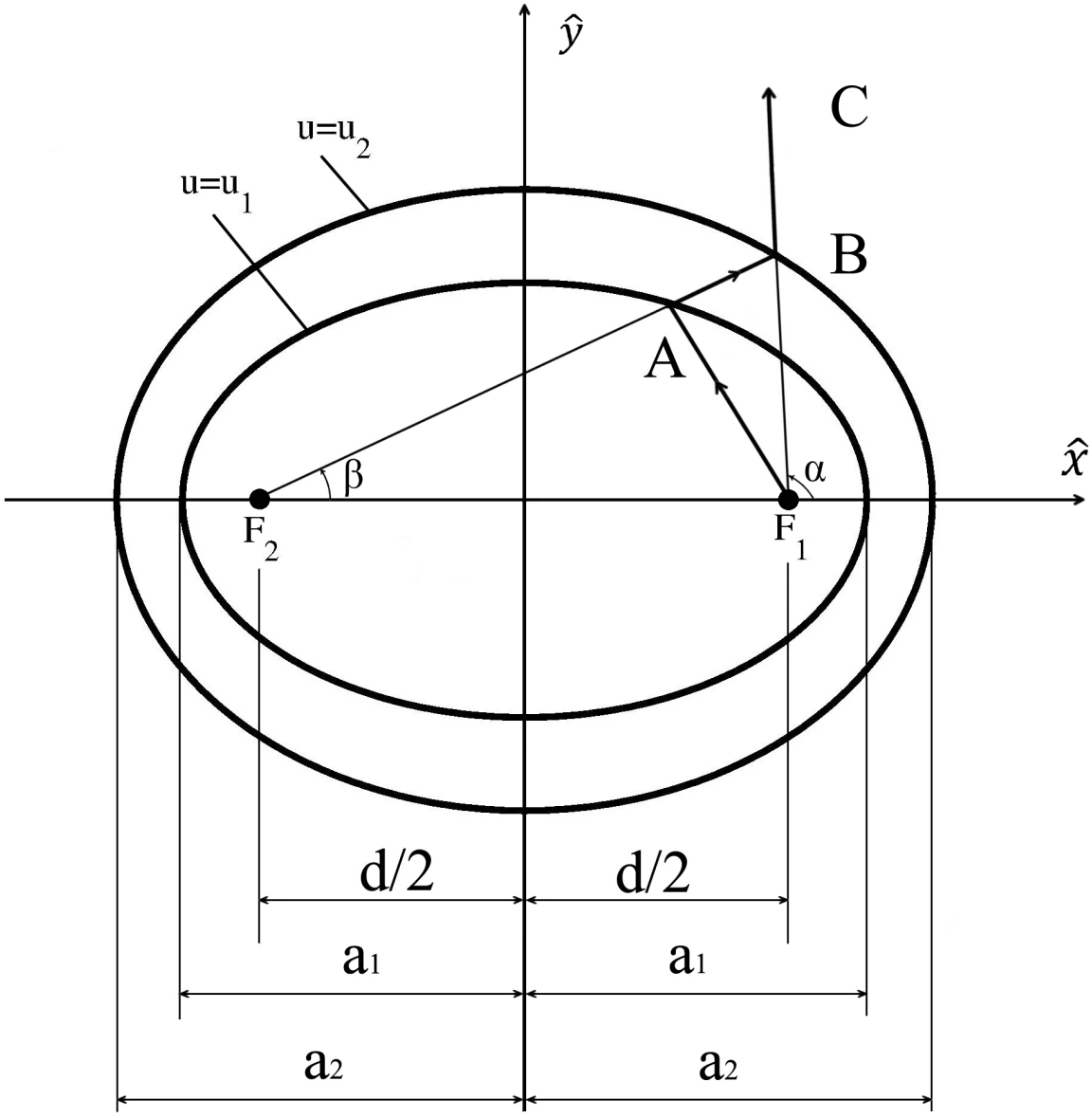

Figure 28. Geometry of the problem for the geometrical optics solution.

7.5 Numerical Results

We first examine comparisons between the radiated power pattern given by (Equation 7.22) and the geometrical optical solution of (Equation 7.27). The results are parameterized according to the ratio

$$r = \frac{2a_1}{\lambda}. \tag{7.29}$$

A smaller value of the ratio correspond to an electrically small cross-section, while a large value of the ratio is associated with an electrically large cross-section, up to infinity that corresponds to the geometrical optics case. Referring to Figure 29, when $r = 0.05$ the radiated power pattern is a slightly flattened circle; when $r = 0.1$, the flattening becomes more prominent; and, when $r = 4.3$ the power radiated pattern approaches the geometrical optics solution.

Next, we examine the effect of changing ζ, while keeping constant all other parameters. Figure 30 indicates quite significant changes of the normalized radiated power pattern of (Equation 7.22) when $\zeta = 0.1, 1, 10$.

The last numerical example is the behavior of the magnitude of the the electric field within the DNG, which is represented in Figure 31 for various values of the ratio r. For smaller values of r there are fewer oscillations within the DNG layer, while the behavior becomes more complex for larger values of r.

The computations of the Mathieu functions were carried out with an extension of the software described in (17) and the acceleration technique described in (18).

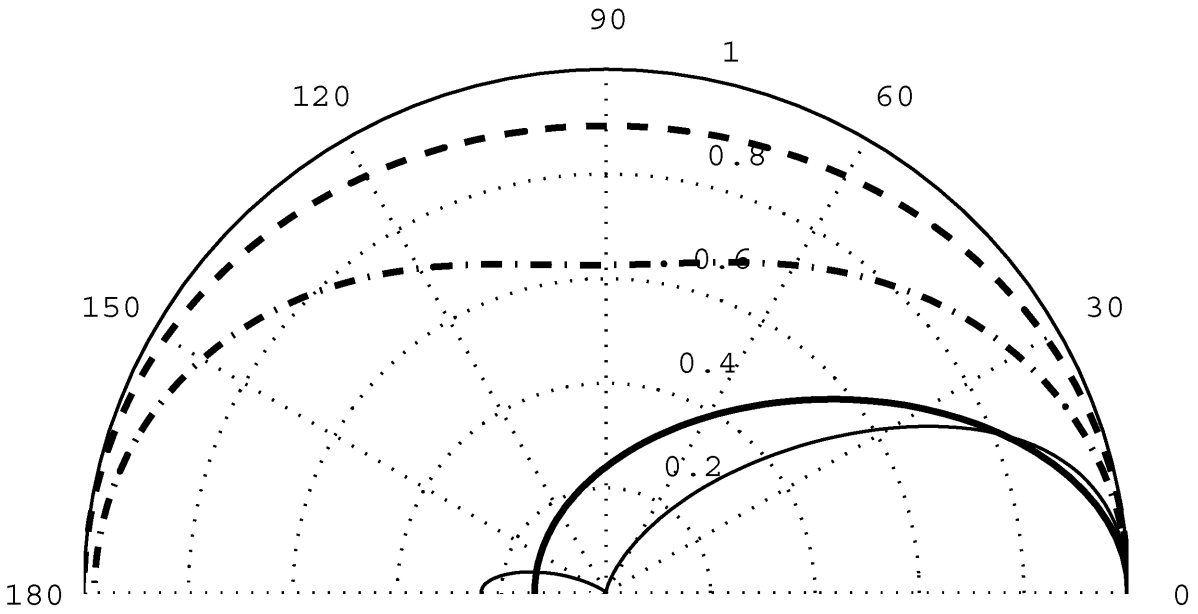

Figure 29. Normalized radiated power patterns for a structure with $u_1 = 0.3$, $u_2 = 0.5$, $\zeta = 10$. The dashed line represents $r = 0.05$ (or $c = 0.15$); the dash-dot line represents $r = 0.1$ (or $c = 0.3$); the thin solid line represents $r = 4.3$ (or $c = 12.92$); and the thick solid line represents the GO solution.

7.6 Conclusion

The novel two-dimensional boundary value problem of radiation from a line source shielded by a confocal elliptic layer of DNG metamaterial has been solved exactly. Numerical data for the radiated far-field and the field inside the sheath have been exhibited.

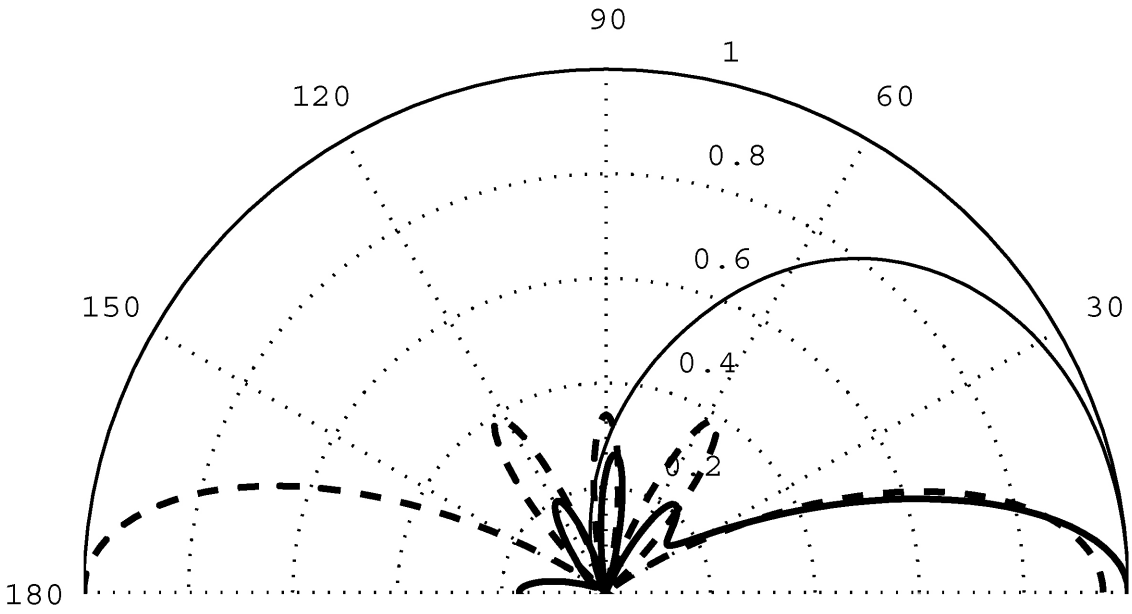

Figure 30. Effect of the variation of the parameter ζ of (Equation 7.3) for a structure with $u_1 = 0.5$, $u_2 = 0.8$ and a line source located at $u_0 = 0.25$, $v_0 = 0$, with $r = 2$. Normalized radiated power patterns for $\zeta = 0.1$, dashed line; $\zeta = 1$, thin solid line; and $\zeta = 10$ thick solid line

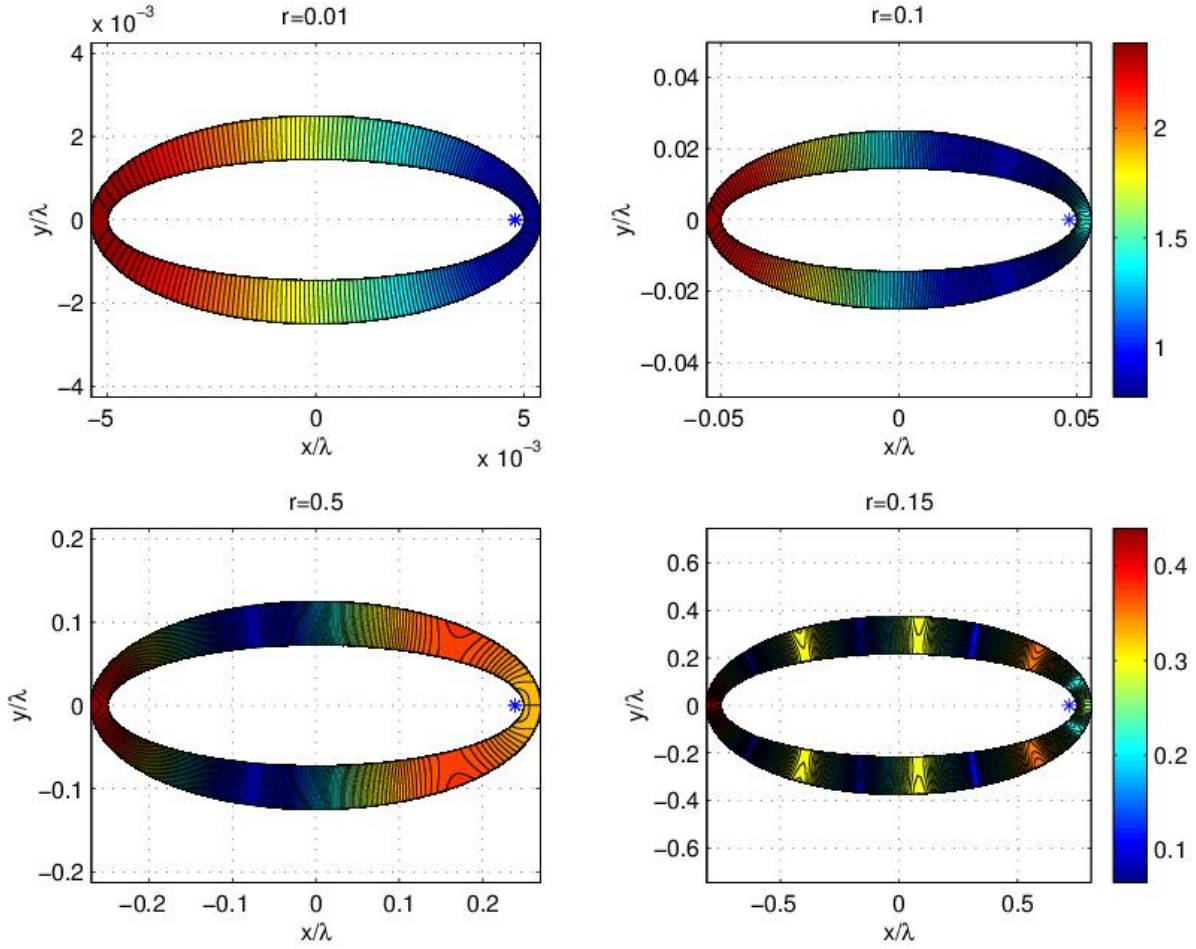

Figure 31. Behavior of $|E_z|$ within the DNG layer with $u_1 = 0.3$, $u_2 = 0.5$, $\zeta = 10$ for various values of the ratio r and for a source located at $u_0 = 0, v_0 = 0$.

APPENDICES

Appendix A

DERIVATION OF ELECTROMAGNETIC SCATTERING BY AN ELLIPTIC DNG METAMATERIAL CYLINDER

$$E_z^i = \sqrt{8\pi} \sum_{m=0}^{\infty} j^m \left[\frac{1}{N_m^{(e)}} \mathrm{Re}_m^{(1)}(c,u)\mathrm{Se}_m(c,v)\mathrm{Se}_m(c,\varphi_0) + \frac{1}{N_m^{(o)}} \mathrm{Ro}_m^{(1)}(c,u)\mathrm{So}_m(c,v)\mathrm{So}_m(c,\varphi_0) \right],$$
$$(u \geq u_1). \tag{A.1}$$

The scattered electric field outside the cylinder can be written as

$$E_z^s = \sqrt{8\pi} \sum_{m=0}^{\infty} j^m \left[\frac{c_m}{N_m^{(e)}} \mathrm{Re}_m^{(4)}(c,u)\mathrm{Se}_m(c,v)\mathrm{Se}_m(c,\varphi_0) + \frac{d_m}{N_m^{(o)}} \mathrm{Ro}_m^{(4)}(c,u)\mathrm{So}_m(c,v)\mathrm{So}_m(c,\varphi_0) \right],$$
$$(u \geq u_1). \tag{A.2}$$

Since

$$\mathrm{Se}_m(-c,v) = \mathrm{Se}_m(c,v),$$
$$\mathrm{So}_m(-c,v) = \mathrm{So}_m(c,v), \tag{A.3}$$

then

Appendix A (Continued)

$$E_{1z} = \sqrt{8\pi} \sum_{m=0}^{\infty} j^m \left[\frac{a_m}{N_m^{(e)}} \mathrm{Re}_m^{(1)}(-c,u)\mathrm{Se}_m(-c,v)\mathrm{Se}_m(-c,\varphi_0) + \frac{b_m}{N_m^{(o)}} \mathrm{Ro}_m^{(1)}(-c,u)\mathrm{So}_m(-c,v)\mathrm{So}_m(-c,\varphi_0) \right], (0 \le u \le u_1). \tag{A.4}$$

The magnetic fields are

$$H_v^i + H_v^s = \frac{-j}{cZ\sqrt{\xi^2-\eta^2}} \frac{\partial}{\partial u}(E_z^i + E_z^s); \;\; (u \ge u_1) \tag{A.5}$$

and

$$H_{1v} = \frac{j}{cZ\sqrt{\xi^2-\eta^2}} \frac{\partial}{\partial u} E_{1z}, \;\; (0 \le u \le u_1). \tag{A.6}$$

Boundary Conditions;

$$\left(E_z^i + E_z^s\right)_{u=u_1} = \left(E_{1z}\right)_{u=u_1}, \tag{A.7}$$

$$\left(H_v^i + H_v^s\right)_{u=u_1} = \left(H_{1v}\right)_{u=u_1}, \tag{A.8}$$

Appendix A (Continued)

$$a_m \mathrm{Re}_m^{(1)}(-c, u1) - c_m \mathrm{Re}_m^{(4)}(c, u1) = \mathrm{Re}_m^{(1)}(c, u1), \tag{A.9}$$

$$a_m \mathrm{Re}_m^{(1)'}(-c, u1) + c_m \mathrm{Re}_m^{(4)'}(c, u1) = -\mathrm{Re}_m^{(1)'}(c, u1) \tag{A.10}$$

and

$$b_m \mathrm{Ro}_m^{(1)}(-c, u1) - d_m \mathrm{Ro}_m^{(4)}(c, u1) = \mathrm{Ro}_m^{(1)}(c, u1), \tag{A.11}$$

$$b_m \mathrm{Ro}_m^{(1)'}(-c, u1) + d_m \mathrm{Ro}_m^{(4)'}(c, u1) = -\mathrm{Ro}_m^{(1)'}(c, u1) \tag{A.12}$$

where $'$ is $\frac{\partial}{\partial u}$ evaluated at $u = u_1$.

$$\Delta^{(e)} = \begin{vmatrix} \mathrm{Re}_m^{(1)}(-c, u_1) & -\mathrm{Re}_m^{(4)}(c, u_1) \\ \mathrm{Re}_m^{(1)\prime}(-c, u_1) & \mathrm{Re}_m^{(4)'}(c, u_1) \end{vmatrix},$$

$$a_m = \frac{1}{\sqrt{\xi_1^2 - 1}\Delta^{(e)}} \begin{vmatrix} \mathrm{Re}_m^{(1)}(c, u_1) & -\mathrm{Re}_m^{(4)}(c, u_1) \\ -\mathrm{Re}_m^{(1)\prime}(c, u_1) & \mathrm{Re}_m^{(4)'}(c, u_1) \end{vmatrix}.$$

From Wronskian relation we can note that

$$\mathrm{Ro}, e_m^{(1)}(c, u)\mathrm{Ro}, e_m^{(4)'}(c, u) - \mathrm{Ro}, e_m^{(4)}(c, u)\mathrm{Ro}, e_m^{(1)'}(c, u) = -j \tag{A.13}$$

Appendix A (Continued)

Therefore, a_m can be found as

$$a_m = \frac{-j}{\sqrt{\xi_1^2 - 1}\Delta^{(e)}}. \tag{A.14}$$

Similarly

$$\Delta^{(o)} = \begin{vmatrix} \mathrm{Ro}_m^{(1)}(-c, u_1) & -\mathrm{Ro}_m^{(4)}(c, u_1) \\ \mathrm{Ro}_m^{(1)\prime}(-c, u_1) & \mathrm{Ro}_m^{(4)'}(c, u_1) \end{vmatrix},$$

$$b_m = \frac{1}{\sqrt{\xi_1^2 - 1}\Delta^{(o)}} \begin{vmatrix} \mathrm{Ro}_m^{(1)}(c, u_1) & -\mathrm{Ro}_m^{(4)}(c, u_1) \\ -\mathrm{Ro}_m^{(1)'}(c, u_1) & \mathrm{Ro}_m^{(4)'}(c, u_1) \end{vmatrix},$$

$$a_m = \frac{-j}{\sqrt{\xi_1^2 - 1}\Delta^{(e)}}, \tag{A.15}$$

$$b_m = \frac{-j}{\sqrt{\xi_1^2 - 1}\Delta^{(o)}}, \tag{A.16}$$

$$c_m = \frac{\Delta_{(c)}}{\Delta^{(e)}}, \tag{A.17}$$

$$d_m = \frac{\Delta_{(d)}}{\Delta^{(o)}}, \tag{A.18}$$

Appendix A (Continued)

where

$$\Delta^{(e)} = \mathrm{Re}_m^{(1)}(-c,u_1)\mathrm{Re}_m^{(4)'}(c,u_1) + \mathrm{Re}_m^{(4)}(c,u_1)\mathrm{Re}_m^{(1)'}(-c,u_1), \tag{A.19}$$

$$\Delta^{(o)} = \mathrm{Ro}_m^{(1)}(-c,u_1)\mathrm{Ro}_m^{(4)'}(c,u_1) + \mathrm{Ro}_m^{(4)}(c,u_1)\mathrm{Ro}_m^{(1)'}(-c,u_1), \tag{A.20}$$

$$\Delta_{(c)} = -\left[\mathrm{Re}_m^{(1)}(-c,u_1)\mathrm{Re}_m^{(1)'}(c,u_1) + \mathrm{Re}_m^{(1)'}(-c,u_1)\mathrm{Re}_m^{(1)}(c,u_1)\right], \tag{A.21}$$

$$\Delta_{(d)} = -\left[\mathrm{Ro}_m^{(1)}(-c,u_1)\mathrm{Ro}_m^{(1)'}(c,u_1) + \mathrm{Ro}_m^{(1)'}(-c,u_1)\mathrm{Ro}_m^{(1)}(c,u_1)\right]. \tag{A.22}$$

Far-field coefficient $P^{(e)}(\phi)$ can be found by using Asymptotic expansions of Radial Mathieu functions

$$\mathrm{Re}, o_m^{(4)}(c,\xi)|_{\xi\to\infty, Imc<0} \approx \frac{j^m}{\sqrt{k\rho}}\exp(-jk\rho + j\frac{\pi}{4}), \tag{A.23}$$

$$E_z^s|_{\xi\to\infty} \approx P^{(e)}(\phi)\sqrt{\frac{2}{\pi k\rho}}\exp(-jk\rho + j\frac{\pi}{4}) \tag{A.24}$$

where the far field coefficient $P^{(e)}(\phi)$ is

$$P^{(e)}(\phi) = 2\pi\sum_{m=0}^{\infty}(-1^m)\left[\frac{c_m}{N_m^{(e)}}\mathrm{Se}_m(c,v)\mathrm{Se}_m(c,\varphi_0) + \frac{d_m}{N_m^{(o)}}\mathrm{So}_m(c,v)\mathrm{So}_m(c,\varphi_0)\right]. \tag{A.25}$$

The bistatic radar cross section (RCS) per unit length is

Appendix A (Continued)

$$\sigma^{(e)}(\phi) = \frac{4}{k}\left|P^{(e)}(\phi)\right|^2. \tag{A.26}$$

Following the same procedure calculation for H-polarization can be found easily.

Appendix B

DERIVATIONS OF MODAL COEFFICIENTS OF EXACT IMAGING BY AN ELLIPTIC LENS

B.1 E-Polarization

The incident field may be expanded in a series of elliptic-cylinder wave functions (1)-(11):

$$E_{1z}^{i} = H_0^{(2)}(-kR) = 4\sum_{m=0}^{\infty} \left[\frac{1}{N_m^{(e)}}\mathrm{Re}_m^{(1)}(-c,u_<)\mathrm{Re}_m^{(4)}(-c,u_>)\mathrm{Se}_m(-c,v_0)\mathrm{Se}_m(-c,v)+ \frac{1}{N_m^{(o)}}\mathrm{Ro}_m^{(1)}(-c,u_<)\mathrm{Ro}_m^{(4)}(-c,u_>)\mathrm{So}_m(-c,v_0)\mathrm{So}_m(-c,v)\right] \tag{B.1}$$

where $u_<$ ($u_>$) is the smaller (larger) between u and u_0. When the electric line source is located inside the lens at the focal line ($x_0 = d/2, y_0 = 0$) the incident electric field only contains even functions and it becomes

$$E_{1z}^{i} = 4\sum_{m=0}^{\infty} \frac{1}{N_m^{(e)}}\mathrm{Re}_m^{(1)}(-c,0)\mathrm{Re}_m^{(4)}(-c,u)\mathrm{Se}_m(c,v) \tag{B.2}$$

Appendix B (Continued)

where we have also used

$$\begin{aligned} \mathrm{Se}_m(-c,v) &= \mathrm{Se}_m(c,v), \\ \mathrm{So}_m(-c,v) &= \mathrm{So}_m(c,v). \end{aligned} \tag{B.3}$$

The scattered field inside the lens is also only contain even functions

$$E_{1z}^s = 4\sum_{m=0}^{\infty} \frac{a_m}{N_m^{(e)}} \mathrm{Re}_m^{(1)}(-c,u)\mathrm{Se}_m(c,v). \tag{B.4}$$

Outside the lens, the scattered field is

$$E_{2z}^s = 4\sum_{m=0}^{\infty} \frac{b_m}{N_m^{(e)}} \mathrm{Re}_m^{(4)}(c,u)\mathrm{Se}_m(c,v), (u \geq u_1). \tag{B.5}$$

The magnetic fields are

$$H_{1v}|_{u=u_1} = H_{1v}^i + H_{1v}^s = \frac{-j}{cZ\sqrt{\xi_1^2-\eta^2}} \frac{\partial}{\partial u}(E_{1z}^i + E_{1z}^s), \ \ (u \geq u_1), \tag{B.6}$$

$$H_{1v}|_{u=u_1} = \frac{-j}{cZ\sqrt{\xi_1^2-\eta^2}} 4\sum_{m=0}^{\infty} \frac{1}{N_m^{(e)}} \left[\mathrm{Re}_m^{(1)}(-c,0)\mathrm{Re}_m^{(4)'}(-c,u) + a_m \mathrm{Re}_m^{(1)'}(-c,u)\right] \mathrm{Se}_m(c,v), (u \geq u_1) \tag{B.7}$$

Appendix B (Continued)

and

$$H_{2v}|_{u=u_1} = \frac{-j}{cZ\sqrt{\xi_1^2-\eta^2}}\frac{\partial}{\partial u}(E_{2z}^s),\ \ (u \geq u_1), \tag{B.8}$$

$$H_{2v}|_{u=u_1} = \frac{-j}{cZ\sqrt{\xi_1^2-\eta^2}} 4\sum_{m=0}^{\infty}\frac{b_m}{N_m^{(e)}}\mathrm{Re}_m^{(4)'}(c,u)\mathrm{Se}_m(c,v),\ \ (u \geq u_1). \tag{B.9}$$

Boundary Conditions;

$$\left(E_{1z}^i + E_{1z}^s\right)_{u=u_1} = \left(E_{2z}^s\right)_{u=u_1}, \tag{B.10}$$

$$\left(H_{1v}^i + H_{1v}^s\right)_{u=u_1} = -\left(H_{2v}^s\right)_{u=u_1}, \tag{B.11}$$

$$a_m\mathrm{Re}_m^{(1)}(-c,u_1) - b_m\mathrm{Re}_m^{(4)}(c,u_1) = -\mathrm{Re}_m^{(1)}(-c,0)\mathrm{Re}_m^{(4)}(-c,u_1), \tag{B.12}$$

$$a_m\mathrm{Re}_m^{(1)'}(-c,u1) + b_m\mathrm{Re}_m^{(4)'}(c,u1) = -\mathrm{Re}_m^{(1)}(-c,0)\mathrm{Re}_m^{(4)'}(-c,u1) \tag{B.13}$$

where $'$ is $\frac{\partial}{\partial u}$ evaluated at $u = u_1$.

Appendix B (Continued)

$$\Delta = \begin{vmatrix} \mathrm{Re}_m^{(1)}(-c, u_1) & -\mathrm{Re}_m^{(4)}(c, u_1) \\ \mathrm{Re}_m^{(1)'}(-c, u1) & \mathrm{Re}_m^{(4)'}(c, u_1) \end{vmatrix},$$

$$\Delta = \mathrm{Re}_m^{(1)}(-c, u_1)\mathrm{Re}_m^{(4)'}(c, u_1) + \mathrm{Re}_m^{(1)'}(-c, u_1)\mathrm{Re}_m^{(4)}(c, u_1), \tag{B.14}$$

$$a_m = \frac{1}{\Delta} \begin{vmatrix} -\mathrm{Re}_m^{(1)}(-c, 0)\mathrm{Re}_m^{(4)}(-c, u_1) & -\mathrm{Re}_m^{(4)}(c, u_1) \\ -\mathrm{Re}_m^{(1)}(-c, 0)\mathrm{Re}_m^{(4)'}(-c, u1) & \mathrm{Re}_m^{(4)'}(c, u1) \end{vmatrix},$$

$$b_m = \frac{1}{\Delta} \begin{vmatrix} \mathrm{Re}_m^{(1)}(-c, u_1) & -\mathrm{Re}_m^{(1)}(-c, 0)\mathrm{Re}_m^{(4)}(-c, u_1) \\ \mathrm{Re}_m^{(1)'}(-c, u1) & -\mathrm{Re}_m^{(1)}(-c, 0)\mathrm{Re}_m^{(4)'}(-c, u1) \end{vmatrix},$$

$$a_m = \frac{-\mathrm{Re}_m^{(1)}(-c, 0)}{\Delta} \left[\mathrm{Re}_m^{(4)'}(c, u_1)\mathrm{Re}_m^{(4)}(-c, u_1) + \mathrm{Re}_m^{(4)}(c, u_1)\mathrm{Re}_m^{(4)'}(-c, u_1)\right], \tag{B.15}$$

$$b_m = \frac{-\mathrm{Re}_m^{(1)}(-c, 0)}{\Delta} \left[\mathrm{Re}_m^{(4)'}(-c, u_1)\mathrm{Re}_m^{(1)}(-c, u_1) - \mathrm{Re}_m^{(4)}(-c, u_1)\mathrm{Re}_m^{(1)'}(-c, u_1)\right], \tag{B.16}$$

(B.17)

Appendix B (Continued)

The modal coefficients for H-polarization can be found easily by following the same procedure.

Appendix C

DERIVATIONS OF RADIATION OF A LINE SOURCE BY A SLOTTED SEMIELLIPTICAL TRENCH FILLED WITH DNG METAMATERIAL

C.1 E-Polarization

C.1.1 Finding the Modal Coefficients When the Line Source is Outside the Trench

The total field in the half-space $y \geq 0$ is

$$E_{1z} = E_{1z}^{i} + E_{1z}^{r} + E_{1z}^{d}, \tag{C.1}$$

$$E_{1z} = 4\sum_{m=0}^{\infty} \frac{1}{N_m^{(o)}} \left[2\mathrm{Ro}_m^{(1)}(c,u_<)\mathrm{Ro}_m^{(4)}(c,u_>) + a_m \mathrm{Ro}_m^{(4)}(c,u_0)\mathrm{Ro}_m^{(4)}(c,u)\right] \mathrm{So}_m(c,v_0)\mathrm{So}_m(c,v) \tag{C.2}$$

where $u_< = u$ and $u_> = u_0$. The electric field inside the trench

$$E_{2z} = 4\sum_{m=0}^{\infty} \frac{c_m}{N_m^{(o)}} \mathrm{Ro}_m^{(4)}(-c,u_0) \left[\mathrm{Ro}_m^{(1)}(-c,u) - \frac{\mathrm{Ro}_m^{(1)}(-c,u_1)}{\mathrm{Ro}_m^{(4)}(-c,u_1)} \mathrm{Ro}_m^{(4)}(-c,u)\right] \mathrm{So}_m(-c,v_0)\mathrm{So}_m(-c,v). \tag{C.3}$$

Appendix C (Continued)

Boundary condition; $(E_{1z})_{u=0} = (E_{2z})_{u=0}$ where one needs to observe that $[S_{om}(c,v)]_{v=v_0} = -[S_{om}(c,v)]_{v=2\pi-v_0}$. As a result, we can find

$$a_m \mathrm{Ro}_m^{(4)}(c,u_0)\mathrm{Ro}_m^{(4)}(c,0) - c_m \mathrm{Ro}_m^{(4)}(-c,u_0)\frac{\mathrm{Ro}_m^{(1)}(-c,u_1)}{\mathrm{Ro}_m^{(4)}(-c,u_1)}\mathrm{Ro}_m^{(4)}(-c,0) = 0. \tag{C.4}$$

Continuity of H field across $u = 0$ yields us $\left(\frac{\partial E_{2z}}{\partial u} = -\frac{\partial E_{1z}}{\partial u}\right)$ where we have taken into account;

- Angular function are odd so there is a sign reversal going across $u = 0$,
- Unit vector $\hat{v}$ reverses going across $u = 0$,
- (c) changes sign across $u = 0$.

$$\begin{aligned} &2\mathrm{Ro}_m^{(1)\prime}(c,0)\mathrm{Ro}_m^{(4)}(c,u_0) + a_m \mathrm{Ro}_m^{(4)}(c,u_0)\mathrm{Ro}_m^{(4)\prime}(c,0) = \\ &- c_m \mathrm{Ro}_m^{(4)}(-c,u_0)\left[\mathrm{Ro}_m^{(1)\prime}(-c,0) - \frac{\mathrm{Ro}_m^{(1)}(-c,u_1)}{\mathrm{Ro}_m^{(4)}(-c,u_1)}\mathrm{Ro}_m^{(4)\prime}(-c,0)\right], \end{aligned} \tag{C.5}$$

$$\begin{aligned} &a_m \mathrm{Ro}_m^{(4)}(c,u_0)\mathrm{Ro}_m^{(4)\prime}(c,0) + c_m \mathrm{Ro}_m^{(4)}(-c,u_0)\left[\mathrm{Ro}_m^{(1)\prime}(-c,0) - \frac{\mathrm{Ro}_m^{(1)}(-c,u_1)}{\mathrm{Ro}_m^{(4)}(-c,u_1)}\mathrm{Ro}_m^{(4)\prime}(-c,0)\right] = \\ &- 2\mathrm{Ro}_m^{(1)\prime}(c,0)\mathrm{Ro}_m^{(4)}(c,u_0), \end{aligned} \tag{C.6}$$

From Equation C.2 and from Equation C.6 we can find the modal coefficients.

Appendix C (Continued)

$$\Delta = \begin{vmatrix} \mathrm{Ro}_m^{(4)}(c,u_0)\mathrm{Ro}_m^{(4)}(c,0) & -\mathrm{Ro}_m^{(4)}(-c,u_0)\frac{\mathrm{Ro}_m^{(1)}(-c,u_1)}{\mathrm{Ro}_m^{(4)}(-c,u_1)}\mathrm{Ro}_m^{(4)}(-c,0) \\ \mathrm{Ro}_m^{(4)}(c,u_0)\mathrm{Ro}_m^{(4)\prime}(c,0) & \mathrm{Ro}_m^{(4)}(-c,u_0)\left[\mathrm{Ro}_m^{(1)\prime}(-c,0) - \frac{\mathrm{Ro}_m^{(1)}(-c,u_1)}{\mathrm{Ro}_m^{(4)}(-c,u_1)}\mathrm{Ro}_m^{(4)\prime}(-c,0)\right] \end{vmatrix},$$

$$\begin{aligned}\Delta =& \mathrm{Ro}_m^{(4)}(c,u_0)\mathrm{Ro}_m^{(4)}(c,0)\mathrm{Ro}_m^{(4)}(-c,u_0)\left[\mathrm{Ro}_m^{(1)\prime}(-c,0) - \frac{\mathrm{Ro}_m^{(1)}(-c,u_1)}{\mathrm{Ro}_m^{(4)}(-c,u_1)}\mathrm{Ro}_m^{(4)\prime}(-c,0)\right] + \\ & \mathrm{Ro}_m^{(4)}(c,u_0)\mathrm{Ro}_m^{(4)\prime}(c,0)\mathrm{Ro}_m^{(4)}(-c,u_0)\frac{\mathrm{Ro}_m^{(1)}(-c,u_1)}{\mathrm{Ro}_m^{(4)}(-c,u_1)}\mathrm{Ro}_m^{(4)}(-c,0), \end{aligned} \tag{C.7}$$

$$\begin{aligned}\Delta =& \mathrm{Ro}_m^{(4)}(c,u_0)\mathrm{Ro}_m^{(4)}(-c,u_0)\left[\mathrm{Ro}_m^{(1)\prime}(-c,0)\mathrm{Ro}_m^{(4)}(c,0) - \frac{\mathrm{Ro}_m^{(4)}(c,0)\mathrm{Ro}_m^{(1)}(-c,u_1)}{\mathrm{Ro}_m^{(4)}(-c,u_1)}\mathrm{Ro}_m^{(4)\prime}(-c,0) + \right. \\ & \left. \mathrm{Ro}_m^{(4)\prime}(c,0)\mathrm{Ro}_m^{(4)}(-c,0)\frac{\mathrm{Ro}_m^{(1)}(-c,u_1)}{\mathrm{Ro}_m^{(4)}(-c,u_1)}\right], \end{aligned} \tag{C.8}$$

$$\Delta a_m = \begin{vmatrix} 0 & -\mathrm{Ro}_m^{(4)}(-c,u_0)\frac{\mathrm{Ro}_m^{(1)}(-c,u_1)}{\mathrm{Ro}_m^{(4)}(-c,u_1)}\mathrm{Ro}_m^{(4)}(-c,0) \\ -2\mathrm{Ro}_m^{(1)\prime}(c,0)\mathrm{Ro}_m^{(4)}(c,u_0) & \mathrm{Ro}_m^{(4)}(-c,u_0)\left[\mathrm{Ro}_m^{(1)\prime}(-c,0) - \frac{\mathrm{Ro}_m^{(1)}(-c,u_1)}{\mathrm{Ro}_m^{(4)}(-c,u_1)}\mathrm{Ro}_m^{(4)\prime}(-c,0)\right] \end{vmatrix},$$

$$\Delta a_m = -2\mathrm{Ro}_m^{(1)\prime}(c,0)\mathrm{Ro}_m^{(4)}(c,u_0)\mathrm{Ro}_m^{(4)}(-c,u_0)\frac{\mathrm{Ro}_m^{(1)}(-c,u_1)}{\mathrm{Ro}_m^{(4)}(-c,u_1)}\mathrm{Ro}_m^{(4)}(-c,0), \tag{C.9}$$

Appendix C (Continued)

$$\Delta c_m = \begin{vmatrix} \mathrm{Ro}_m^{(4)}(c,u_0)\mathrm{Ro}_m^{(4)}(c,0) & 0 \\ \mathrm{Ro}_m^{(4)}(c,u_0)\mathrm{Ro}_m^{(4)\prime}(c,0) & -2\mathrm{Ro}_m^{(1)\prime}(c,0)\mathrm{Ro}_m^{(4)}(c,u_0) \end{vmatrix},$$

$$\Delta c_m = -2\mathrm{Ro}_m^{(4)}(c,0)\mathrm{Ro}_m^{(4)}(c,u_0)\mathrm{Ro}_m^{(1)\prime}(c,0)\mathrm{Ro}_m^{(4)}(c,u_0). \tag{C.10}$$

Finally, the modal coefficients a_m and c_m can be found by using the fractions below.

$$a_m = \frac{\Delta a_m}{\Delta}, \qquad c_m = \frac{\Delta c_m}{\Delta} \tag{C.11}$$

$$c_m = \frac{-2\mathrm{Ro}_m^{(4)}(c,u_0)\mathrm{Ro}_m^{(4)}(c,0)\mathrm{Ro}_m^{(1)'}(c,0)}{\Delta_m}, \tag{C.12}$$

$$a_m = \frac{-2\mathrm{Ro}_m^{(4)}(-c,u_0)\mathrm{Ro}_m^{(4)}(-c,0)\mathrm{Ro}_m^{(1)'}(c,0)}{\Delta_m}\frac{\mathrm{Ro}_m^{(1)}(-c,u_1)}{\mathrm{Ro}_m^{(4)}(-c,u_1)}, \tag{C.13}$$

where

$$\begin{aligned}\Delta_m = &\mathrm{Ro}_m^{(4)}(-c,u_0)\left[\mathrm{Ro}_m^{(4)}(c,0)\mathrm{Ro}_m^{(1)'}(-c,0) - \frac{\mathrm{Ro}_m^{(1)}(-c,u_1)}{\mathrm{Ro}_m^{(4)}(-c,u_1)}\mathrm{Ro}_m^{(4)}(c,0)\mathrm{Ro}_m^{(4)'}(-c,0) + \right. \\ &\left.\frac{\mathrm{Ro}_m^{(1)}(-c,u_1)}{\mathrm{Ro}_m^{(4)}(-c,u_1)}\mathrm{Ro}_m^{(4)'}(c,0)\mathrm{Ro}_m^{(4)}(-c,0)\right].\end{aligned} \tag{C.14}$$

Appendix C (Continued)

C.1.2 Finding the Modal Coefficients When the Line Source is Inside the Trench

Tangential component of H field inside the channel along $\xi = 1$

$$H_{2v} = \frac{j}{cZ\sqrt{1-\eta^2}} \left\{ 4 \sum_{m=0}^{\infty} \left[\frac{2}{N_m^{(o)}} \mathrm{Ro}_m^{(1)\prime}(-c,0)\mathrm{Ro}_m^{(4)}(-c,u_0) + e_m \mathrm{Ro}_m^{(1)\prime}(-c,0) + f_m \mathrm{Ro}_m^{(4)\prime}(-c,0) \right] \right\}$$
$$\mathrm{So}_m(c,v_0)\mathrm{So}_m(c,v). \tag{C.15}$$

Tangential component of H field outside the channel along $u = 0$

$$H_{1v} = \frac{-j}{cZ\sqrt{1-\eta^2}} \left\{ 4 \sum_{m=0}^{\infty} \frac{g_m}{N_m^{(o)}} \mathrm{Ro}_m^{(4)\prime}(c,0)\mathrm{So}_m(c,v_0)\mathrm{So}_m(c,v) \right\}. \tag{C.16}$$

Continuity of H_v across $u = 0$ yields $H_{1v} = H_{2v}$.Once again, along $u = 0$, the $\hat{v}$ unit vector reverses direction and the angular function $\mathrm{So}_m(\pm c, v)$ is odd so that this introduces another change of sign. Therefore,

$$2\mathrm{Ro}_m^{(1)\prime}(-c,0)\mathrm{Ro}_m^{(4)}(-c,u_0) + e_m \mathrm{Ro}_m^{(1)\prime}(-c,0) + f_m \mathrm{Ro}_m^{(4)\prime}(-c,0) = -g_m \mathrm{Ro}_m^{(4)\prime}(c,0) \tag{C.17}$$

Total field inside the trench is,

$$E_{2z} = 4 \sum_{m=0}^{\infty} \frac{1}{N_m^{(o)}} \left[2\mathrm{Ro}_m^{(1)}(-c,u_<)\mathrm{Ro}_m^{(4)}(-c,u_>) + e_m \mathrm{Ro}_m^{(1)}(-c,u) + f_m \mathrm{Ro}_m^{(4)}(-c,u) \right]$$
$$\mathrm{So}_m(c,v_0)\mathrm{So}_m(c,v). \tag{C.18}$$

Appendix C (Continued)

Total field outside the channel will be

$$E_{1z} = 4\sum_{m=0}^{\infty} \frac{g_m}{N_m^{(o)}} \mathrm{Ro}_m^{(4)}(c,u)\mathrm{So}_m(c,v_0)\mathrm{So}_m(c,v). \tag{C.19}$$

Continuity of E_z across $u = 0$ yields

$$f_m \mathrm{Ro}_m^{(4)}(-c,0) = -g_m \mathrm{Ro}_m^{(4)}(c,0) \Longrightarrow g_m = -\frac{\mathrm{Ro}_m^{(4)}(-c,0)}{\mathrm{Ro}_m^{(4)}(c,0)} f_m. \tag{C.20}$$

Another condition is $E_z = 0$ on $u = u_1$. Hence,

$$2\mathrm{Ro}_m^{(1)}(-c,u_0)\mathrm{Ro}_m^{(4)}(-c,u_1) + e_m \mathrm{Ro}_m^{(1)}(-c,u_1) + f_m \mathrm{Ro}_m^{(4)}(-c,u_1) = 0 \tag{C.21}$$

If we substitute Equation C.20 into Equation C.17, we will get

$$e_m \mathrm{Ro}_m^{(1)\prime}(-c,0) + f_m \left[\mathrm{Ro}_m^{(4)\prime}(-c,0) - \mathrm{Ro}_m^{(4)\prime}(c,0) \frac{\mathrm{Ro}_m^{(4)}(-c,0)}{\mathrm{Ro}_m^{(4)}(c,0)} \right] = -2\mathrm{Ro}_m^{(1)\prime}(-c,0)\mathrm{Ro}_m^{(4)}(-c,u_0). \tag{C.22}$$

If we rewrite Equation C.21, we obtain

$$e_m \mathrm{Ro}_m^{(1)}(-c,u_1) + f_m \mathrm{Ro}_m^{(4)}(-c,u_1) = -2\mathrm{Ro}_m^{(1)}(-c,u_0)\mathrm{Ro}_m^{(4)}(-c,u_1). \tag{C.23}$$

Now let us solve Equation C.23 and Equation C.22 for e_m and f_m,

Appendix C (Continued)

$$\Delta = \begin{vmatrix} \mathrm{Ro}_m^{(1)}(-c,u_1) & \mathrm{Ro}_m^{(4)}(-c,u_1) \\ \mathrm{Ro}_m^{(1)\prime}(-c,0) & \left[\mathrm{Ro}_m^{(4)\prime}(-c,0) - \frac{\mathrm{Ro}_m^{(4)}(-c,0)}{\mathrm{Ro}_m^{(4)}(c,0)}\mathrm{Ro}_m^{(4)\prime}(c,0)\right] \end{vmatrix},$$

$$\Delta = \mathrm{Ro}_m^{(1)}(-c,u_1)\left[\mathrm{Ro}_m^{(4)\prime}(-c,0) - \frac{\mathrm{Ro}_m^{(4)}(-c,0)}{\mathrm{Ro}_m^{(4)}(c,0)}\mathrm{Ro}_m^{(4)\prime}(c,0)\right] - \mathrm{Ro}_m^{(4)}(-c,u_1)\mathrm{Ro}_m^{(1)\prime}(-c,0). \tag{C.24}$$

$$\Delta e_m = \begin{vmatrix} -2\mathrm{Ro}_m^{(1)}(-c,u_0)\mathrm{Ro}_m^{(4)}(-c,u_1) & \mathrm{Ro}_m^{(4)}(-c,u_1) \\ -2\mathrm{Ro}_m^{(1)\prime}(-c,0)\mathrm{Ro}_m^{(4)}(-c,u_0) & \left[\mathrm{Ro}_m^{(4)\prime}(-c,0) - \frac{\mathrm{Ro}_m^{(4)}(-c,0)}{\mathrm{Ro}_m^{(4)}(c,0)}\mathrm{Ro}_m^{(4)\prime}(c,0)\right] \end{vmatrix},$$

$$\begin{aligned}\Delta e_m =& 2\mathrm{Ro}_m^{(4)}(-c,u_1)\left\{-\mathrm{Ro}_m^{(1)}(-c,u_0)\left[\mathrm{Ro}_m^{(4)\prime}(-c,0) - \frac{\mathrm{Ro}_m^{(4)}(-c,0)}{\mathrm{Ro}_m^{(4)}(c,0)}\mathrm{Ro}_m^{(4)\prime}(c,0)\right] + \right. \\ & \left. \mathrm{Ro}_m^{(1)\prime}(-c,0)\mathrm{Ro}_m^{(4)}(-c,u_0)\right\}, \end{aligned} \tag{C.25}$$

$$\Delta f_m = \begin{vmatrix} \mathrm{Ro}_m^{(1)}(-c,u_1) & -2\mathrm{Ro}_m^{(1)}(-c,u_0)\mathrm{Ro}_m^{(4)}(-c,u_1) \\ \mathrm{Ro}_m^{(1)\prime}(-c,0) & -2\mathrm{Ro}_m^{(1)\prime}(-c,0)\mathrm{Ro}_m^{(4)}(-c,u_0) \end{vmatrix},$$

Appendix C (Continued)

$$\Delta f_m = -2\mathrm{Ro}_m^{(1)\prime}(-c,0)\left\{\mathrm{Ro}_m^{(1)}(-c,u_1)\mathrm{Ro}_m^{(4)}(-c,u_0) - \mathrm{Ro}_m^{(1)}(-c,u_0)\mathrm{Ro}_m^{(4)}(-c,u_1)\right\}. \quad \text{(C.26)}$$

We can find the modal coefficients by,

$$e_m = \frac{\Delta e_m}{\Delta}, \qquad f_m = \frac{\Delta f_m}{\Delta}. \quad \text{(C.27)}$$

C.2 H-Polarization

$$H_{1z}^i = 4\sum_{m=0}^{\infty}\left[\frac{1}{N_m^{(e)}}\mathrm{Re}_m^{(1)}(c,u_<)\mathrm{Re}_m^{(4)}(c,u_>)\mathrm{Se}_m(c,v_0)\mathrm{Se}_m(c,v) + \frac{1}{N_m^{(o)}}\mathrm{Ro}_m^{(1)}(c,u_<)\mathrm{Ro}_m^{(4)}(c,u_>)\right]$$
$$\mathrm{So}_m(c,v_0)\mathrm{So}_m(c,v) \quad \text{(C.28)}$$

where $u_<$ ($u_>$) is the smaller (larger) between u and u_0. The magnetic source located outside of the trench so $u_< = u$ and $u_> = u_0$. The total magnetic field in the half-space $y \geq 0$ is

$$H_{1z} = H_{1z}^i + H_{1z}^r + H_{1z}^d \quad \text{(C.29)}$$

$$H_{1z} = 4\sum_{m=0}^{\infty}\frac{1}{N_m^{(e)}}\left[2\mathrm{Re}_m^{(1)}(c,u)\mathrm{Re}_m^{(4)}(c,u_0) + \tilde{a}_m\mathrm{Re}_m^{(4)}(c,u_0)\mathrm{Re}_m^{(4)}(c,u)\right]\mathrm{Se}_m(c,v_0)\mathrm{Se}_m(c,v). \quad \text{(C.30)}$$

Appendix C (Continued)

The total magnetic field inside the trench is given by

$$H_{2z} = 4\sum_{m=0}^{\infty} \frac{\tilde{b}_m}{N_m^{(e)}} \mathrm{Re}_m^{(4)}(-c,u_0)\left[\mathrm{Re}_m^{(1)}(-c,u) - \frac{\mathrm{Re}_m^{(1)\prime}(-c,u_1)}{\mathrm{Re}_m^{(4)\prime}(-c,u_1)}\mathrm{Re}_m^{(4)}(-c,u)\right]\mathrm{Se}_m(c,v_0)\mathrm{Se}_m(c,v) \tag{C.31}$$

$$\frac{\partial H_{1z}}{\partial u} = 4\sum_{m=0}^{\infty} \frac{1}{N_m^{(e)}}\left[2\mathrm{Re}_m^{(1)\prime}(c,u)\mathrm{Re}_m^{(4)}(c,u_0) + \tilde{a}_m \mathrm{Re}_m^{(4)}(c,u_0)\mathrm{Re}_m^{(4)\prime}(c,u)\right]\mathrm{Se}_m(c,v_0)\mathrm{Se}_m(c,v) \tag{C.32}$$

$$\frac{\partial H_{2z}}{\partial u} = 4\sum_{m=0}^{\infty} \frac{\tilde{b}_m}{N_m^{(e)}} \mathrm{Re}_m^{(4)}(-c,u_0)\left[\mathrm{Re}_m^{(1)\prime}(-c,u) - \frac{\mathrm{Re}_m^{(1)\prime}(-c,u_1)}{\mathrm{Re}_m^{(4)\prime}(-c,u_1)}\mathrm{Re}_m^{(4)\prime}(-c,u)\right]\mathrm{Se}_m(c,v_0)\mathrm{Se}_m(c,v) \tag{C.33}$$

- Angular Mathieu functions do not change sign
- Unit vector $\hat{v}$ add $(-)$
- c introduces another minus sign so the boundary conditions will be,

$$\left.\frac{\partial(H_{1z})}{\partial\xi}\right|_{\xi=1} = \left.\frac{\partial H_{2z}}{\partial\xi}\right|_{\xi=1}, \; H_{1z}|_{\xi=1} = H_{2z}|_{\xi=1}\,. \tag{C.34}$$

Appendix C (Continued)

If we apply the boundary conditions we will get

$$A = \frac{\mathrm{Re}_m^{(4)}(-c,u_0)}{\mathrm{Re}_m^{(4)}(c,u_0)}, \tag{C.35}$$

$$B = \mathrm{Re}_m^{(1)}(-c,0) - \frac{\mathrm{Re}_m^{(1)\prime}(-c,u_1)}{\mathrm{Re}_m^{(4)\prime}(-c,u_1)}\mathrm{Re}_m^{(4)}(-c,0), \tag{C.36}$$

$$C = \mathrm{Re}_m^{(1)\prime}(-c,0) - \frac{\mathrm{Re}_m^{(1)\prime}(-c,u_1)}{\mathrm{Re}_m^{(4)\prime}(-c,u_1)}\mathrm{Re}_m^{(4)\prime}(-c,0) \tag{C.37}$$

and

$$\begin{aligned}
&\tilde{a}_m\mathrm{Re}_m^{(4)}(c,0) - \tilde{b}_m\frac{\mathrm{Re}_m^{(4)}(-c,u_0)}{\mathrm{Re}_m^{(4)}(c,u_0)}\left[\mathrm{Re}_m^{(1)}(-c,0) - \frac{\mathrm{Re}_m^{(1)\prime}(-c,u_1)}{\mathrm{Re}_m^{(4)\prime}(-c,u_1)}\mathrm{Re}_m^{(4)}(-c,0)\right] = -2\mathrm{Re}_m^{(1)}(c,0),\\
&\tilde{a}_m\mathrm{Re}_m^{(4)\prime}(c,0) - \tilde{b}_m\frac{\mathrm{Re}_m^{(4)}(-c,u_0)}{\mathrm{Re}_m^{(4)}(c,u_0)}\left[\mathrm{Re}_m^{(1)\prime}(-c,0) - \frac{\mathrm{Re}_m^{(1)\prime}(-c,u_1)}{\mathrm{Re}_m^{(4)\prime}(-c,u_1)}\mathrm{Re}_m^{(4)\prime}(-c,0)\right] = -2\mathrm{Re}_m^{(1)\prime}(c,0).
\end{aligned} \tag{C.38}$$

Solving last equations yields the following result,

$$\Delta = \begin{vmatrix} \mathrm{Re}_m^{(4)}(c,0) & \frac{\mathrm{Re}_m^{(4)}(-c,u_0)}{\mathrm{Re}_m^{(4)}(c,u_0)}\left[\mathrm{Re}_m^{(1)}(-c,0) - \frac{\mathrm{Re}_m^{(1)\prime}(-c,u_1)}{\mathrm{Re}_m^{(4)\prime}(-c,u_1)}\mathrm{Re}_m^{(4)}(-c,0)\right] \\ \mathrm{Re}_m^{(4)\prime}(c,0) & \frac{\mathrm{Re}_m^{(4)}(-c,u_0)}{\mathrm{Re}_m^{(4)}(c,u_0)}\left[\mathrm{Re}_m^{(1)\prime}(-c,0) - \frac{\mathrm{Re}_m^{(1)\prime}(-c,u_1)}{\mathrm{Re}_m^{(4)\prime}(-c,u_1)}\mathrm{Re}_m^{(4)\prime}(-c,0)\right] \end{vmatrix},$$

Appendix C (Continued)

$$\Delta = \frac{\mathrm{Re}_m^{(4)}(-c,u_0)}{\mathrm{Re}_m^{(4)}(c,u_0)}\left[\left(\mathrm{Re}_m^{(1)\prime}(-c,0) - \frac{\mathrm{Re}_m^{(1)\prime}(-c,u_1)}{\mathrm{Re}_m^{(4)\prime}(-c,u_1)}\mathrm{Re}_m^{(4)\prime}(-c,0)\right)\mathrm{Re}_m^{(4)}(c,0) - \left(\mathrm{Re}_m^{(1)}(-c,0) - \frac{\mathrm{Re}_m^{(1)\prime}(-c,u_1)}{\mathrm{Re}_m^{(4)\prime}(-c,u_1)}\mathrm{Re}_m^{(4)}(-c,0)\right)\mathrm{Re}_m^{(4)\prime}(c,0)\right], \tag{C.39}$$

$$\Delta\tilde{a}_m = \begin{vmatrix} -2\mathrm{Re}_m^{(1)}(c,0) & \frac{\mathrm{Re}_m^{(4)}(-c,u_0)}{\mathrm{Re}_m^{(4)}(c,u_0)}\left[\mathrm{Re}_m^{(1)}(-c,0) - \frac{\mathrm{Re}_m^{(1)\prime}(-c,u_1)}{\mathrm{Re}_m^{(4)\prime}(-c,u_1)}\mathrm{Re}_m^{(4)}(-c,0)\right] \\ -2\mathrm{Re}_m^{(1)\prime}(c,0) & \frac{\mathrm{Re}_m^{(4)}(-c,u_0)}{\mathrm{Re}_m^{(4)}(c,u_0)}\left[\mathrm{Re}_m^{(1)\prime}(-c,0) - \frac{\mathrm{Re}_m^{(1)\prime}(-c,u_1)}{\mathrm{Re}_m^{(4)\prime}(-c,u_1)}\mathrm{Re}_m^{(4)\prime}(-c,0)\right] \end{vmatrix},$$

$$\Delta\tilde{a}_m = 2\frac{\mathrm{Re}_m^{(4)}(-c,u_0)}{\mathrm{Re}_m^{(4)}(c,u_0)}\left[\left(\mathrm{Re}_m^{(1)}(-c,0) - \frac{\mathrm{Re}_m^{(1)\prime}(-c,u_1)}{\mathrm{Re}_m^{(4)\prime}(-c,u_1)}\mathrm{Re}_m^{(4)}(-c,0)\right)\mathrm{Re}_m^{(1)\prime}(c,0) - \left(\mathrm{Re}_m^{(1)\prime}(-c,0) - \frac{\mathrm{Re}_m^{(1)\prime}(-c,u_1)}{\mathrm{Re}_m^{(4)\prime}(-c,u_1)}\mathrm{Re}_m^{(4)\prime}(-c,0)\right)\mathrm{Re}_m^{(1)}(c,0)\right], \tag{C.40}$$

$$\Delta\tilde{b}_m = \begin{vmatrix} \mathrm{Re}_m^{(4)}(c,0) & -2\mathrm{Re}_m^{(1)}(c,0) \\ \mathrm{Re}_m^{(4)\prime}(c,0) & -2\mathrm{Re}_m^{(1)\prime}(c,0) \end{vmatrix},$$

$$\Delta\tilde{b}_m = 2\left[\mathrm{Re}_m^{(1)}(c,0)\mathrm{Re}_m^{(4)\prime}(c,0) - \mathrm{Re}_m^{(1)\prime}(c,0)\mathrm{Re}_m^{(4)}(c,0)\right]. \tag{C.41}$$

Appendix D

DERIVATIONS OF ELECTROMAGNETIC RADIATION AND SCATTERING FOR A GAP IN A CORNER BACKED BY A CAVITY FILLED WITH DNG METAMATERIAL

Derivations are quite similar with the other chapters so only derivations for magnetic line source incidence has been given. Remaining parts can be easilly found by similar approaches.

D.1 Magnetic Line Source Incidence

The primary magnetic field is

$$\boldsymbol{H}^i = \hat{z} H_z^i = \hat{z} H_0^{(2)}(kR). \tag{D.1}$$

$$H_{1z}^i = H_0^{(2)}(kR) = 4 \sum_{m=0}^{\infty} \left[\frac{1}{N_m^{(e)}} \mathrm{Re}_m^{(1)}(c, u_<) \mathrm{Re}_m^{(4)}(c, u_>) \mathrm{Se}_m(c, v) \mathrm{Se}_m(c, v_0) \right.$$
$$\left. + \frac{1}{N_m^{(o)}} \mathrm{Ro}_m^{(1)}(c, u_<) \mathrm{Ro}_m^{(4)}(c, u_>) \mathrm{So}_m(c, v) \mathrm{So}_m(c, v_0) \right], \tag{D.2}$$

$$H_{1z}^{go} = H_0^{(2)}(kR) + H_0^{(2)}(kR_1) + H_0^{(2)}(kR_2) + H_0^{(2)}(kR_3), \tag{D.3}$$

Appendix D (Continued)

where

$$R_1 = \sqrt{(x - x_0)^2 + (y + y_0)^2}, \tag{D.4}$$

$$R_2 = \sqrt{(x + x_0)^2 + (y - y_0)^2}, \tag{D.5}$$

$$R_3 = \sqrt{(x + x_0)^2 + (y + y_0)^2}. \tag{D.6}$$

Referring to Figure 22, the image line S_1 is located at $(x_0, -y_0) \equiv (u_0, 2\pi - v_0)$, the image line S_2 at $(-x_0, y_0) \equiv (u_0, \pi - v_0)$, and the image line S_3 at $(-x_0, -y_0) \equiv (u_0, \pi + v_0)$.

for $S_1 \equiv (u_0, 2\pi - v_0)$,

$$\mathrm{Se}_m(c, 2\pi - v_0) \to \mathrm{Se}_m(c, v_0), \tag{D.7}$$

$$\mathrm{So}_m(c, 2\pi - v_0) \to -\mathrm{So}_m(c, v_0). \tag{D.8}$$

The field due to the line source at S_1 can be written as

$$H_{1z}^{S_1} = H_0^{(2)}(kR_1) = 4 \sum_{m=0}^{\infty} \left[\frac{1}{N_m^{(e)}} \mathrm{Re}_m^{(1)}(c, u_<) \mathrm{Re}_m^{(4)}(c, u_>) \mathrm{Se}_m(c, v) \mathrm{Se}_m(c, v_0) \right.$$
$$\left. - \frac{1}{N_m^{(o)}} \mathrm{Ro}_m^{(1)}(c, u_<) \mathrm{Ro}_m^{(4)}(c, u_>) \mathrm{So}_m(c, v) \mathrm{So}_m(c, v_0) \right], \tag{D.9}$$

Appendix D (Continued)

for $S_2 \equiv (u_0, \pi - v_0)$,

$$\mathrm{Se}_m(c, \pi - v_0) \to (-1)^m \mathrm{Se}_m(c, v_0), \tag{D.10}$$

$$\mathrm{So}_m(c, \pi - v_0) \to -(-1)^m \mathrm{So}_m(c, v_0). \tag{D.11}$$

The field due to the line source at S_2 is

$$H_{1z}^{S_2} = H_0^{(2)}(kR_2) = 4 \sum_{m=0}^{\infty} \left[\frac{(-1)^m}{N_m^{(e)}} \mathrm{Re}_m^{(1)}(c, u_<) \mathrm{Re}_m^{(4)}(c, u_>) \mathrm{Se}_m(c, v) \mathrm{Se}_m(c, v_0) \right.$$
$$\left. - \frac{(-1)^m}{N_m^{(o)}} \mathrm{Ro}_m^{(1)}(c, u_<) \mathrm{Ro}_m^{(4)}(c, u_>) \mathrm{So}_m(c, v) \mathrm{So}_m(c, v_0) \right], \tag{D.12}$$

for $S_3 \equiv (u_0, \pi + v_0)$,

$$\mathrm{Se}_m(c, \pi + v_0) \to (-1)^m \mathrm{Se}_m(c, v_0), \tag{D.13}$$

$$\mathrm{So}_m(c, \pi + v_0) \to (-1)^m \mathrm{So}_m(c, v_0). \tag{D.14}$$

The field due to the line source at S_3,

$$H_{1z}^{S_3} = H_0^{(2)}(kR_3) = 4 \sum_{m=0}^{\infty} \left[\frac{(-1)^m}{N_m^{(e)}} \mathrm{Re}_m^{(1)}(c, u_<) \mathrm{Re}_m^{(4)}(c, u_>) \mathrm{Se}_m(c, v) \mathrm{Se}_m(c, v_0) \right.$$
$$\left. + \frac{(-1)^m}{N_m^{(o)}} \mathrm{Ro}_m^{(1)}(c, u_<) \mathrm{Ro}_m^{(4)}(c, u_>) \mathrm{So}_m(c, v) \mathrm{So}_m(c, v_0) \right]. \tag{D.15}$$

The geometrical optic field becomes,

Appendix D (Continued)

$$H_{1z}^{go} = 16 \sum_{l=0}^{\infty} \frac{l}{N_{2l}^{(e)}} \mathrm{Re}_{2l}^{(1)}(c, u_<) \mathrm{Re}_{2l}^{(4)}(c, u_>) \mathrm{Se}_{2l}(c, v) \mathrm{Se}_{2l}(c, v_0). \tag{D.16}$$

CITED LITERATURE

1. P.L.E. Uslenghi, "Exact penetration, radiation and scattering for a slotted semielliptical channel filled with isorefractive material," *IEEE Trans. Antennas Propag.*, vol. 52, no. 6, pp. 1473–1480, June 2004.

2. D. Erricolo, M. D. Lockard, C. M. Butler, and P. L. E. Uslenghi, "Numerical analysis of penetration, radiation, and scattering for a 2D slotted semielliptical channel filled with isorefractive material," *PIER*, vol. 53, pp. 69–89, 2005.

3. D. Erricolo, M.D. Lockard, C.M. Butler, and P.L.E. Uslenghi, "Comparison among currents on surfaces inside and near a semielliptical channel filled with isorefractive material that backs a slotted plane: currents computed by analytical formulas and by integral equation methods," in *Proc. Intl. Conf. on Electromagnetics in Advanced Applications (ICEAA'03)*, Torino, Italy, Sept 2003, pp. 469–474.

4. D. Erricolo, M.D. Lockard, C.M. Butler, and P.L.E. Uslenghi, "Currents on conducting surfaces of a semielliptical-channel-backed slotted screen in an isorefractive environment," *IEEE Trans. Antennas Propag.*, vol. 53, no. 7, pp. 2350–2356, July 2005.

5. C. Berardi, D. Erricolo, and P.L.E. Uslenghi, "Exact dipole radiation for an oblate spheroidal cavity filled with isorefractive material and aperture-coupled to a half space," *IEEE Trans. Antennas Propag.*, vol. 52, no. 9, pp. 2205–2213, Sept. 2004.

6. D. Erricolo and P. L. E. Uslenghi, "Penetration, radiation, and scattering for a cavity-backed gap in a corner," *IEEE Trans. Antennas Propag.*, vol. 53, no. 8, pp. 2738–2748, Aug. 2005.

7. T. M. Larsen, P.L.E. Uslenghi, and D. Erricolo, "Low-frequency behavior of a slotted semielliptical channel," in *Digest of National Radio Science Meeting*, Boulder, CO, USA, Jan 2004, p. 66.

8. C. M. Butler, D. Erricolo, III C. L. Bopp, and A. W. Schreiber, "Penetration through a slotted screen into a semi-elliptic channel: Simple integral equation with an eigenseries kernel," in *IEEE AP-S International Symposium on Antennas and Propagation and USNC/URSI National Radio Science Meeting and AMEREM*, Albuquerque, NM, July 9-15, 2006.

CITED LITERATURE (Continued)

9. N. W. McLachlan, *Theory and Application of Mathieu Functions*, Dover Publications, New York, 1964.

10. J. A. Stratton, *Electromagnetic Theory*, McGraw-Hill, New York, 1941.

11. J. J. Bowman, T. B. A. Senior, and P. L. E. Uslenghi, *Electromagnetic and Acoustic Scattering by Simple Shapes*, Hemisphere Publishing Corporation, New York, 1987.

12. P.L.E. Uslenghi, "Optical behavior of elliptical lenses made of dng metamaterial," in *IEEE Antennas Wirel. Propag. Lett.*, 2010, vol. 9, pp. 566–567.

13. O. Akgol, D. Erricolo, and P.L.E. Uslenghi, "Electromagnetic behavior of an elliptical lens made of DNG metamaterial," in *XXIX General Assembly of the International Union of Radio Science (URSI)*, Chicago, Illinois, 11-15 Aug. 2008.

14. O. Akgol, D. Erricolo, and P.L.E. Uslenghi, "Imaging Effect of an Elliptic Perfect Lens ," in *National Radio Science Meeting*, Boulder, Colorado, 5-8 Jan. 2009.

15. R. W. Ziolkowski and E. Heyman, "Wave propagation in media having negative permittivity and permeability," *Phys. Rev. E*, vol. 64, no. 5, pp. 056,625, 2001.

16. O. Akgol, D. Erricolo, and P.L.E. Uslenghi, "Electromagnetic Radiation and Scattering for a Gap in a Corner Backed by a Cavity Filled with DNG Metamaterial," *Radio Science*, vol. 46, no. RS4005,, pp. doi:10.1029/2010RS004471, 4 Aug. 2011.

17. D. Erricolo, "Algorithm 861: Fortran 90 subroutines for computing the expansion coefficients of Mathieu functions using Blanch's algorithm," *ACM Transactions on Mathematical Software*, vol. 32, no. 4, pp. 622–634, Dec. 2006.

18. D. Erricolo, "Acceleration of the convergence of series containing Mathieu functions using Shanks transformation," *IEEE Antennas Wireless Propag. Lett.*, vol. 2, pp. 58–61, 2003.

19. Staff of the computation Laboratory, *Tables relating to Mathieu Functions*, Applied Mathematics Series. U.S. Government Printing Office, Washington, D.C., 1967, second edition edition, Aug. 1967.

20. P.L.E. Uslenghi, "Exact scattering from a slotted semielliptical channel," in *Proceedings of the IEEE AP-S International Symposium*, Chicago, IL, USA, July 1992, pp. 1849–1852.

CITED LITERATURE (Continued)

21. P.L.E. Uslenghi, "Exact geometrical optics scattering from a tri-sector isorefractive wedge structure," *IEEE Antennas Wireless Propag. Lett.*, vol. 3, pp. 94–95, 2004.

22. P.L.E. Uslenghi, "Exact electromagnetic penetration througha gap in a corner," in *Proc. 1999 IEEE-APS/URSI Intl. Symp*, Orlando, FL, USA, July 1999, p. 164.

23. O. Akgol, D. Erricolo, and P.L.E. Uslenghi, "Electromagnetic scattering by a semielliptical trench filled with DNG metamaterial," in *International Conference on Electromagnetics in Advanced Applications ICEAA*, Turin, Italy, 14-18 Sept. 2009.

24. O. Akgol, D. Erricolo, and P.L.E. Uslenghi, "Radiation of a line source by a slotted semielliptical trench filled with DNG metamaterial," in *Proc. MAPE'09*, Beijing, China, 27-29 Oct. 2009, pp. 114–117.

25. O. Akgol, D. Erricolo, and P.L.E. Uslenghi, "Electromagnetic Radiation and Scattering for a Gap in a Corner Backed by a Cavity Filled with DNG Metamaterial," in *The 9th Engineering Mathematics and Applications Conference*, University of Adelaide, South Australia, 6-9 Dec. 2009.

26. P.L.E. Uslenghi, O. Akgol, V. G Daniele, and D. Erricolo, "Exact radiation by a line source located inside a confocal elliptic layer of DNG metamaterial," in *XXX URSI General Assembly and Scientific Symposium*, Istanbul, Turkey, 13-20 Aug. 2011.

27. O. Akgol, V.G. Daniele, D. Erricolo, and P.L.E. Uslenghi, "Radiation from a line source shielded by a confocal elliptic layer of dng metamaterial," in *IEEE Antennas Wirel. Propag. Lett.*, 2011, vol. 10, pp. 943 – 946.

28. O. Akgol, D. Erricolo, and P.L.E. Uslenghi, "Exact imaging by an elliptic lens," in *IEEE Antennas Wirel. Propag. Lett.*, 2011, vol. 10, pp. 639–642.

VITA

Oguzhan Akgol

NAME:EDUCAT B.A., Inonu University, Malatya, Turkey, 2001M.S.

2002 Turkish Minister of National Education Scholarship for

O. Akgol, D. Erricolo, and P.L.E. Uslenghi, “Electromagnetic

VITA (Continued)

O. Akgol, D. Erricolo, and P.L.E. Uslenghi, “Electro